1-1-2011

Surface Wave Derived Shear Velocity Structure of the Gamburtsev Subglacial Mountains, Transantarctic Mountains, and West Antarctica and Shallow Seismicity of the Mariana and Tonga Subduction Zones

David Heeszel
Washington University in St. Louis

WASHINGTON UNIVERSITY IN ST. LOUIS

Department of Earth and Planetary Sciences

Dissertation Examination Committee
Douglas Wiens, Chair
Jeffrey Catalano
James Conder
Martin Israel
Philip Skemer
Michael Wysession

SURFACE WAVE DERIVED SHEAR VELOCITY STRUCTURE OF THE GAMBURTSEV SUBGLACIAL MOUNTAINS, TRANSANTARCTIC MOUNTAINS, AND WEST ANTARCTICA AND SHALLOW SEISMICITY OF THE MARIANA AND TONGA SUBDUCTION ZONES

By

David Scott Heeszel

A dissertation presented to the
Graduate School of Arts and Sciences
of Washington University in
partial fulfillment of the
requirements for the degree
of Doctor of Philosophy

August 2011

St. Louis, Missouri

Acknowledgements: When I think about the number of people who have helped me undertake the writing of this dissertation and the requisite research, it is difficult to know where to begin and perhaps more importantly end. First, I need to thank my advisor and mentor Doug Wiens for his support, guidance, and patience during my time here at Washington University. My wife, Lindsey, and daughter, Anika, have constantly provided love, support, distraction, and the oft required kick in the rear that have lead to the completion of this volume. I would also like to thank the other great people who work in the seismology group here particularly, Patrick Shore for the friendship and guidance he has offered me, Ghassan Aleqabi for forcing me to return to first principles, Garrett Euler, Moira Pyle, and Erica Emry for suffering with me through life as a graduate student. Many thanks to all of the graduate students, past and present, for their friendship and the front office staff for keeping me aware that there are indeed deadlines and rules. I also need to thank all of the people involved in the collection of the data I present here. Thanks to the TAMSEIS, GAMSEIS, POLENET, MARIANA, and TONGA06 field teams who are too numerous to list, this dissertation could not exist without your hard work. I owe a deep debt of gratitude to the National Science Foundation, which provided the financial resources to undertake these projects and the PASSCAL division of the Incorporated Research Insitutions for Seismology (IRIS) for providing instrumentation and seismic data. Finally, I want to thank my parents for always encouraging me to reach for more, do what I love, and pursue my own path through life.

Table of Contents

List of Figures

List of Tables

Chapter 1

Introduction

Recent advances in seismic instrumentation have allowed researchers to undertake focused investigations of regions previously inaccessible. From the bottom of the sea to the coldest, driest places on earth, we are now able to deploy seismometers to remote locations and be certain of collecting large amounts of useable data. By focusing regionally scaled seismic arrays in locations of tectonic and geodynamic interest we are able to better image the structure of these regions and place them in a global framework. This is particularly important in regions such as Antarctica and the ocean bottom where more traditional tools such as geologic mapping and sampling are difficult, if not currently impossible. This volume utilizes information garnered from several temporary deployments to such locations.

In chapter 2 we use data collected from ocean bottom seismometers in the Mariana Islands to investigate the implications of along-arc extension. Small earthquakes that go undetected by the large global seismic network are detected by a temporary ocean bottom seismic array. The locations and timing of this seismicity place constraints on along-arc extension, an important arc process. In chapter 3 we use data collected by a short-term seismic array designed to detect and locate aftershocks associated with the May 3, 2006 M_W8.0 Tonga earthquake. The fault mechanism of this earthquake is unusual and has important implications for tsunami hazard associated with the Tonga subduction zone. Through high precision location of aftershocks, we are able to

determine the updip and downdip limits of seismicity associated with the mainshock. We are also able to relocate the mainshock location to a high degree of precision.

In chapters 4 and 5 we utilize data from seismic arrays in Antarctica to image the crust and upper mantle structure of specific regions of interest using teleseismic surface waves. We focus our efforts on the Gamburtsev Subglacial Mountains in Chapter 4. This mountain range is located in the center of the East Antarctic Ice Sheet and their origin is enigmatic. Through high-resolution surface wave tomography possible only with a seismic array located above them, we are able to determine the lithospheric age and crustal thickness of the mountains. This study has important implications for determining the most recent age of uplift and their tectonothermal history. Finally, in chapter 5 we utilize data from three separate temporary deployments to image the crust and upper mantle of the Antarctic continent from the Gamburtsev Subglacial Mountains, across the Transantarctic Mountains that define the boundary between East and West Antarctica to Marie Byrd Land. This study encompasses nearly nine million square kilometers of the Antarctic continent.

Chapter 2

Earthquake evidence for along-arc extension in the Mariana Islands

Heeszel, D. S., D. A. Wiens, P. J. Shore, H. Shiobara, and H. Sugioka (2008), Earthquake evidence for along-arc extension in the Mariana Islands, *Geochem. Geophys. Geosyst.*, 9, Q12X03, doi:10.1029/2008GC002186.

Abstract

Analysis of data from a deployment of ocean bottom and land seismographs in 2003-2004 detected four swarms of earthquakes in the overriding plate of the Mariana subduction system between the fore arc and the back arc spreading center. Two additional shallow swarms were identified by analyzing the teleseismic earthquake catalogs from 1967-2003. Focal mechanism solutions for these swarms, determined from regional waveform inversion for the 2003-2004 events or retrieved from the Centroid Moment Tensor catalog for previous years suggest a complex system of deformation throughout the arc. We observe arc parallel extension near volcanic cross-chains, arc perpendicular extension along the frontal arc, and arc parallel compression farther into the back arc near the Mariana Spreading Center. A swarm beneath the middle and eastern summits of the Diamante cross chain may have recorded magmatic activity. Volcanic cross-chains showing evidence of adiabatic decompression melting from extensional upwelling are localized at regions of enhanced along-strike extension. The

earthquake data are consistent with recent GPS results indicating 12 mm/yr of extension between Guam and Agrihan. The along-arc extension may result from either increasing curvature of the Mariana system with time or from deformation induced by oblique subduction in the northernmost and southernmost regions of the arc.

Mariana Islands, Arc-parallel extension, Cross-chain volcanism

2.1 Introduction

It is widely understood that the geometry of island arcs must change as the configuration of the trench and the downgoing slab evolves. Tectonic reconstructions have documented large changes of arc curvature for several subduction zones in the geologic record [*Barker and Dalziel,* 1983; *Hall et al.,* 1995]. Geodynamic modeling studies have shown that slabs with limited along-strike length (< 1500 km) tend to develop strong curvature due to the retreat of the slab edges [*Schellart*, 2005; *Schellart et al.*, 2007]. Changes in slab geometry and curvature must cause significant deformation of the overriding plate, but actual documentation of ongoing deformation and its possible links to volcanic and other tectonic processes in present-day arcs has been limited.

The Mariana Arc presents a ideal opportunity to study the deformation of the overriding arc microplate and associated effects on volcanism in response to changes in slab geometry. The currently active Mariana Arc developed at approximately 7Ma [*Stern et al*., 2003] because of the formation of the Mariana Trough and the migration of arc volcanism from the previous arc (currently the West Mariana Ridge) to the currently active volcanic arc. The curvature of the Mariana arc has increased through time as can be seen in maps of the Philippine Sea basin in which the original arc, the Palau Kyushu ridge (see figure 2.1 inset), is nearly straight. Subsequent arcs, the West Mariana Ridge and the active Mariana arc, indicate increasing curvature with time (see *Stern, et al.,* [2003] for a review). The Mariana Trough has a spreading rate that changes along the length of the arc, decreasing from 45 mm/yr in the south near Guam to 15 mm/yr in the north [*Kato et al*., 2003] and eventually transitions from seafloor spreading to rifting north of 20ºN [*Martinez et al*., 2000]. Additionally, the relative subduction direction

changes over the length of the arc. It is trench-perpendicular through the central region of the arc and increases in obliquity to the north and the south [*Bird*, 2003]. Evidence for arc parallel extension in the Mariana microplate also exists in the form of numerous serpentinite seamounts in the fore arc, some of which are upthrown horsts [*Fryer*, 1996] and bathymetric mapping data that indicates a large number of roughly trench perpendicular normal faults in the Mariana fore arc [*Stern and Smoot*, 1998]. Geodetic results also indicate significant arc-parallel extensional strains in the Mariana Arc [*McCaffery*, 1996; *Bird*, 2003; *Kato et al*., 2003].

Volcanic cross chains occur throughout the Mariana arc and are apparent in bathymetric images as a line of high structures extending from the active arc into the back arc (figure 2.1). Several have had their geochemistry studied in detail, particularly the cross-chain extending west from Guguan island [*Stern, et al*., 2006], a small network of cross-chain volcanoes at 14º40'N which Chaife [*Kohut, et al.*, 2006] and Northwest-Rota-1 [*Embly, et al.*, 2006] seamounts are a part, and the Kasuga cross-chain [*Stern et al.*, 1993, *Fryer et al*., 1997]. The chain at Guguan is morphologically typical of other cross-chains in the Marianas, consisting of a large volcano at the magmatic front with one or more smaller volcanoes extending into the back arc. Geochemistry at Guguan is consistent with other arc volcanoes, but there is a decrease in the subduction component as the volcanoes extend into the back arc [*Stern et al*., 2006]. The cross-chain at 14º40'N is atypical of the other cross-chains in the Mariana arc, as it is comprised of several small (mean volume of ~27 km^3) seamounts extending from the arc to the back arc in a diffuse line. Chaife Seamount has been studied in detail and has an anomalous geochemistry. It

is more consistent with MORB than typical arc magmas, having an Mg# of ~76, much higher than typical arc volcanism [*Kohut, et al*., 2006].

The frontal arc, a region of uplifted basement rock trenchward of the volcanic front including the largest islands in the Mariana system, is also undergoing deformation [*Fryer*, 1996; *Stern et al*., 2003]. Interpreted as an upthrown block bound on both sides by normal faults [*Stern and Smoot*, 1998], *Gvirtzman and Stern* [2004] propose that this uplift is due to a narrower plate coupling zone in the southern portion of the Mariana Arc. This narrower zone of slab 'pull-down' allows the fore arc of the overriding plate to rise higher than for the more widely coupled subduction zone in the central portion of the Mariana Arc.

In this paper we present the results of a 2003-2004 Mariana passive seismic experiment as well as teleseismic catalogs that recorded significant seismicity in the overriding plate, placing constraints on the present-day deformation of the Mariana platelet in response to changing slab geometry. We discuss the relationship of this seismicity and deformation to volcanic cross-chains and propose that the locations of cross-chain volcanoes may be linked to localization of extensional strain. We also note several swarms of seismicity that likely are associated with previously undocumented submarine volcanic activity.

2.2 Data

The Mariana Subduction Factory Imaging Project deployed 20 broadband land seismographs and 58 semi-broadband ocean bottom seismographs (OBSs) during May-June of 2003 and recovered them in April-May 2004. The land stations consisted of

either Streckheisen STS-2 or Guralp 40-T seismometers and Reftek 72A-08 dataloggers with GPS timing located on 10 islands between Guam and Agrihan. Each island with a station had at least one STS-2 seismograph; the 40T seismographs were deployed in denser arrays on Saipan, Tinian, and Guam. The 58 OBSs were located around the region of deepest earthquake activity near Pagan Island extending from the forearc through the back-arc spreading center to the West Mariana Ridge (figure 2.1). Lamont-Doherty Earth Observatory operated fifty OBSs that used three-component Mark Products L4 sensors with a 1-Hz natural period and modified amplifiers to extend long-period performance [*Webb et al*., 2001]. Fifteen of these OBSs were an older 16-bit model and 35 were of a new 24-bit design. The remaining OBSs used Precision Measuring Devices (PMD-WB2023LP) sensors and were built by H. Shiobara at the University of Tokyo. The 35 new U.S. OBSs stopped recording ~50 days after deployment due to a firmware error, eight U.S. OBSs were not recovered (not plotted in figure 2.1), and several U.S. OBSs failed to deploy the sensor to the seafloor properly. All of the land stations operated properly throughout the deployment with the exception of Anatahan Island, which experienced several power failures due to ash from volcanic activity [*Pozgay et al*., 2005]. The coordinates of all stations and recovered OBSs are given in *Pozgay et al*., [2007].

2.3 Analysis

2.3.1 Earthquake Locations

Earthquakes were initially detected and located using Boulder Real Time Technology's Antelope data management package [*Quinlan et al*., 1996]. The short-term

average/long-term average (STA/LTA) automatic picking routine was used to identify earthquakes and their initial locations were calculated using a gridsearch routine with the IASPEI91 velocity model [*Kennett and Engdahl*, 1991] used to calculate travel-times. Subsequently, over 3400 earthquakes with a significant number of arrivals were reviewed and relocated using the GENLOC least squares location module [*Pavlis et al*., 2004], and the best located earthquakes are plotted in figure 2.1. Since IASPEI91 is a global velocity model, we relocated the closely clustered local events for this study using a one-dimensional P-wave model of the Mariana arc [*Takahashi et al*., 2007] for the crust. The S-wave model was derived from the P-wave model using Vp/Vs ratios consistent with the crust [*Shaw,* 1994] and upper mantle [*Christensen,* 1996] of a volcanic arc. The upper mantle was modeled as PREM [*Dziewonski and Anderson*, 1981] with both the P and S wave velocities reduced by 2-5% based on modeling events of known focal mechanisms in both Tonga-Fiji and the Marianas. Most of the relocated events used in this study and the stations that detected them are either on or very near the volcanic arc, so a single velocity model was appropriate to improve the travel-time misfit.

In order to further improve earthquake locations for the four observed swarms we applied a multiple-event relative relocation program based on the hypocentroidal decomposition algorithm [*Jordan and Sverdrup*, 1981] that was modified to use the local travel time calculator from the HYPOELLIPSE program [*Lahr*, 1999]. The program was applied to each swarm individually and only events with greater than ten total arrivals and more than three S-wave arrivals were included in the relocation.

In addition to the four swarms detected during the 2003-2004 deployment, two previous teleseismically-detected swarms were discovered in the International

Seismological Center (ISC) database [*ISC*, 2001]. One occurred during 1990 and was located in the same region as the swarm in the fore arc observed during the 2003-2004 experiment. The second historical swarm occurred during 1997 at approximately 14º40'N, a region of anomalous volcanism. Both swarms were relocated using teleseismic P-wave arrival times using the method of [*Jordan and Sverdrup*, 1981] and the IASPEI91velocity model [*Kennett and Engdahl*, 1991].

2.3.2 Focal Mechanisms

Although the swarm earthquakes were quite small we were able to calculate focal mechanisms for seven events (table 2.1), six in the swarm on the Diamante Seamount chain and one in the region between West Sarigan seamount and the Mariana Trough, using regional waveform inversion. There is low signal-to-noise ratio above 0.1Hz and significant uncertainty in the small-scale seismic velocity structure to which higher frequency signal is sensitive. As a result, the inversions were calculated at frequencies of 0.03-0.06 Hz, a low frequency range that has a higher signal-noise ratio and for which uncertainties in velocity structure are less important.

To calculate focal mechanisms, we first used a reflectivity code [*Kennett*, 1983] that incorporates a water layer to calculate synthetic seismograms for three fundamental focal mechanisms. Synthetics can then be calculated for an arbitrary focal mechanism using a linear combination of these fundamental synthetics [*Langston and Helmberger*, 1975]. We use a grid search over fault strike, dip, slip, and time function duration to determine the proper focal mechanism and seismic moment with the lowest least squared misfit for the vertical and, where there is a good signal-noise ratio, the transverse

components. Each gridsearch was run 100 times with random start, step size, and number of steps to ensure the solution is not biased by the discretization of the grid search. A test focal mechanism was calculated for an earthquake in the CMT catalog near Northwest Rota that occurred close to the end of the deployment to ensure that our method accurately calculated the focal mechanisms of interest. Our results are nearly identical to those in the CMT (figure 2.2).

2.4 Results

2.4.1 14º40'N, Northwest Rota

One of the largest swarms, both in earthquake magnitude and in the number of events, occurred on an E-W trending line from just northwest of Rota Island to the Mariana Trough at a latitude of approximately 14º40'N. This swarm of 64 events occurred in August and September of 1997 (see table 2.2 for details). Nearly two-thirds of the earthquakes in the swarm occurred during a two-day period (29-30) in August, though there was no large mainshock to indicate that this is an aftershock sequence. We used teleseismic arrival times from the ISC to relocate these events using the hypocentroidal decomposition method. A few of the westernmost events lie on the Mariana Trough, but the majority are located on or very near a diffuse, E-W trending line of small volcanic seamounts running perpendicular to the volcanic arc (figure 2.3) from the magmatic front to the back-arc spreading center. Geochemical analysis of two seamounts in this cross-chain indicate that in addition to arc style volcanism [Embly et al., 2006] adiabatic decompression melting also occurs [Kohut et al., 2006]. Additionally, two of these events have solutions in the CMT database that indicate N-S

extension and are plotted in their relocated positions in figure 2.3. Additional CMT solutions for the area also indicate an N-S oriented extensional axis, though the westernmost solutions with E-W normal faulting are likely associated with back-arc basin tectonics.

2.4.2 Diamante Seamount Chain

The swarm on the Diamante seamount chain (figure 2.4) occurred between June and August, 2003 and consisted of 111 earthquakes with depths of less than 40 km (table 2.2 for average locations). None of the earthquakes associated with the swarm were detected teleseismically. We obtained focal mechanisms for six events using waveform inversion, with moment magnitudes ranging from M_w 3.3 to 3.7 (table 2.1). All events share a generally E-W striking, steeply dipping fault plane and a dominantly N-S oriented tensional axis. These factors combined suggest the presence of significant N-S extension in the region of the Diamante Seamount chain associated with tectonism and magmatism. Bathymetric mapping of the seamount chain also indicate strong N-S extension (figure 2.4) particularly on the summit of East Diamante where the caldera is elongated in and E-W direction and contains E-W striking normal faults.

The occurrence of 99 of the 111 events during a four week period in August 2003 and the absence of a clear mainshock may indicate that this swarm is associated with active magmatism beneath one or multiple volcanoes in the chain. However, earthquake locations do not indicate a progression either laterally or with depth, and the focal mechanisms, representing the largest earthquakes in the swarm, show no preferred progression in location with time. 95% confidence ellipses for this swarm average 9.2

km in a nearly east-west line, making it difficult to determine which of the seamounts the earthquakes occurred beneath, though the best located events indicate that both East Diamante and Mid Diamante were seismically active. The earthquakes are spread out in a diffuse cloud that underlies both mid-Diamante and East Diamante seamounts. We conclude that the swarm could indicate an eruptive event at either Middle or East Diamante, or it could have resulted from magmatic activity at deeper levels beneath the seamounts.

2.4.3 16° 40' N, Mariana Trough

The swarm located furthest to the west, between Sarigan Island and the Mariana Trough consisted of 21 events between July and September, 2003 with activity peaking during the second week of August. The earthquakes had an average depth of ~24 km, and this swarm is the only one, other than that at Diamante, for which a focal mechanism was determined from regional waveforms. This event has a focal mechanism consistent with thrust faulting with a strike-slip component and a shallowly dipping plane with a strike that is roughly parallel to a small bathymetric ridge to the west of the swarm (circled feature in figure 2.5). Additionally the rest of the swarm lies along strike with this bathymetric feature, and there is little to no bathymetric relief in the region immediately surrounding the location of the observed swarm, presumably due to sediment cover. The 95% confidence ellipses for the earthquakes are on average ~5 km in the E-W direction and smaller in the N-S, so it is unlikely that they are actually located on the bathymetric high to the west or further to the east near the volcanic arc. We

suggest that this swarm is associated with compressional tectonics associated with the tectonically uplifted compression ridge in this region.

2.4.4 West Sarigan seamount

The earthquake swarm just northwest of West Sarigan seamount consisted of 33 events at an average depth of ~17 km during December, 2003 and January, 2004. The absence of a mainshock and the short duration of the swarm over a period of approximately 40 days (see table 2.2) indicates that the swarm is likely associated with magmatic or tectonic processes very near West Sarigan seamount. The observed earthquakes are well constrained in depth by the presence of the Sarigan Island station ~25 km away. Additionally, a CMT solution from August, 2005 indicates the presence of N-S extensional faulting in the same area as the observed swarm. We interpret this swarm as the result of either north-south extension along the Sarigan volcanic cross-chain or else magmatic activity near West Sarigan seamount.

2.4.5 Fore Arc Rise

The final two swarms are located in the fore arc rise. One was observed by the local seismograph array and consisted of 19 earthquakes beginning in October, 2003 and continuing into January, 2004. They have an average depth of 27 km, consistent with the teleseismic swarm in the same region. The teleseismic swarm occurred during March and April, 1990 and consisted of 13 events at an average depth of ~28 km. The majority of events (nine) occurred during the last three days of March. These swarms are too far east to be of volcanic origin as there is no confirmed volcanism in the uplifted fore arc

[*Fryer*, 1996; *Stern et al*., 2003]. Additionally the earthquakes are too far west of the trench to be associated with the shallow thrust zone. Both swarms are well located laterally, though the locally detected swarm is the most poorly constrained of the locally detected swarms due to its occurrence later in the deployment when many of the OBSs had already failed. This swarm is likely due to continued uplift of the fore arc basement material that composes the islands further to the south that [*Gvirtzman and Stern*, 2003] suggest is due to weak plate coupling between the subducting Pacific plate and the overriding Mariana microplate.

2.5 Discussion

2.5.1 Extensional swarms associated with Volcanic Cross Chains

Arc parallel extension has been documented in the southern Marianas by GPS data. GPS surveys from 1992 to 1999 [*Kato et al*., 2003] indicate a separation rate of approximately 5mm/yr between Saipan and Guam, the closest islands for which there are results. Data from more islands, particularly Rota and Tinian, is required to discern whether this extension is localized at 14º40'N or if it is associated with a more diffuse zone of deformation. Geochemical evidence from Chaife seamount a small seamount with an Mg#~76 [*Kohut et al*., 2006], and the seismic results presented here serve as a strong indication that the deformation is in fact concentrated at 14º40'N. Miller *et al.* [2006] proposed a slab tear in the region of 14º40'N. Based on the GPS results of Kato *et al.* [2003] and the amount of intervening mantle between the downgoing slab and the overriding plate in this region we believe it is unlikely to be a significant contributor to the observed volcano-tectonic activity observed in this location. This concentration of

seismicity at volcanic cross-chains occurs in other locations within the Mariana Arc such as at the Diamante Seamount chain indicating that the location of cross-chain volcanism is controlled by the concentration of along arc extensional stresses throughout the arc.

The Diamante cross-chain volcanoes are morphologically different from those of the Northwest Rota region. They are larger and fewer in number and are more consistent with those described as typical cross-chain volcanoes [*Kohut et al*., 2006]. However, the high level of seismicity in the region coupled with the focal mechanisms determined in this study is suggestive of a similar mechanism for their formation as those to the south. The same arc parallel extension that may control extensional volcanism to the south near 14º40'N may also play a role in the development of other, larger cross chains such as that at Diamante. Though not fully resolved, GPS results from *Kato et al*. [2003] indicate that there is approximately 3mm/yr of separation between Saipan and Anatahan which are the islands directly to the south and north of the Diamante cross-chain respectively. This suggests that the focusing of arc parallel stresses likely controls the location of the Diamante cross-chain. Additionally, the size and structure of the seamounts may be controlled by their location in the main portion of the arc rather than in the southern seamount province [*Stern et al*., 2003] where volcanoes are typically smaller and none is of significant enough size to breach the surface.

Geochemical evidence from the Guguan [*Stern et al*., 2006] cross-chain indicates that the material erupted behind the island arc becomes progressively more consistent with primitive mantle melts altered by subduction components than with typical arc magmas seen at the magmatic front (island arc) moving toward the back-arc spreading center. Data from the 14°40'N cross-chain [*Kohut et al.*, 2006] indicates adiabatic

decompression melting which is consistent with extensional stresses. The localization of seismic activity and a style of volcanism that is both more primitive and more indicative of passive upwelling due to extension rather than flux melting from a downgoing slab suggests that the location of cross-chain volcanism is controlled more by localization of arc parallel extensional stress and less by subduction processes.

2.5.2 Seismicity and Deformation in the Mariana microplate

The observed pattern of along-strike extension in the forearc and arc and compression near the backarc spreading center is likely due to tectonic forces that are increasing the curvature of the Mariana microplate. The microplate is bounded on the east and south by the Mariana trench, on the west by the Mariana Trough and associated spreading center that effectively decouples stresses in the microplate from those in the Philippine Sea Plate [*Martinez et al*., 2000] and on the north by a complex system of rifting and transform faulting [*Bird*, 2003]. Increasing curvature with the endpoints fixed will lead to along arc extension in most of the arc and particularly on the convex side, with the possibility of compression on the concave side. In addition to the increasing curvature in the arc, the Mariana microplate is associated with the oblique subduction of the Pacific plate in the northern and southern parts of the forearc. Oblique subduction causes sliver motion of the arc and fore arc similar to that suggested for arc parallel extension in the Okinawa Trough [*Kubo and Fukuyama*, 2003]. This may have an additive effect in stretching the arc in the N-S direction, producing the extensional stresses resulting in cross-chain volcanoes in the arc.

If the curvature of the arc is increasing then the western portion of the arc microplate will have to be undergoing compression, as indicated by the swarm and tectonically uplifted compression ridge between Sarigan Island and the back-arc spreading center. The fact that compression in the back arc is observed in only one place relatively near the spreading center may indicate that there are several regions of extensional stress due to the combined effects of increasing curvature and oblique subduction with small regions of along arc contraction near the spreading center. The detailed along-strike distribution of extensional and compressional strain in the arc and backarc may be rather complex but consistent with this overall pattern (figure 2.6).

2.6 Conclusions

Seismic observations of several swarms of small earthquakes present strong evidence for significant along-arc extension in the upper plate of the Mariana subduction system between the trench and back-arc spreading center. This extension facilitates the occurrence of volcanic cross chains involving passive mantle upwelling such as those at 14º40'N [*Kohut et al*., 2006] and the Diamante cross-chain. The interaction of different volcanic and tectonic processes likely gives the two cross-chains different morphologic and seismic characteristics even though the same overall process is responsible for both. Recent GPS and earthquake slip vector results [*McCaffery*, 1996; *Bird*, 2003; *Kato et al*., 2003] also support along arc extension in the southern region though the amount of extension between Saipan and islands further to the north is not yet fully resolved. Based on the strong correlation between extensional seismicity and volcanism, it is likely that cross-chain location it tectonically controlled and is centralized in regions with

heightened levels of arc parallel stress and that the style of volcanism is controlled by the presence of active upwelling. While the region around the arc and fore arc is undergoing extension, the back arc region may be undergoing shortening due to the increasing curvature of the arc and the shortening that this creates. The mechanism for the localization of compressional stresses in the back arc does not appear to be as well developed as the mechanism for localizing arc parallel extension.

2.7 Acknowledgements

. We thank Bob Stern for helpful comments on an earlier version, and numerous people for assistance with deploying and recovering the seismographs, particularly Patrick Shore, Spahr Webb, Allan Sauter, Mitchell Barklage, Brian Shiro, Sara Pozgay, Patrick Jonke, Juan Camacho, Joe Kaipat, and Ray Chong, as well as the captains and the crews of the R/V Kaiyo, the R/V Wecoma, and the Super Emerald. Land seismic instrumentation was provided by the PASSCAL program of the Incorporated Research Institutions in Seismology (IRIS) and the Lamont Ocean Bottom Seismograph Facility provided ocean bottom seismographs. This research was supported by the MARGINS program under National Science Foundation grants OCE-0001938 and EAR-0549056. We also thank Bob Stern and Cliff Frolich for helpful reviews.

2.8 References

Barker, P. F., and I . W. D. Dalziel (1983), Progress in geodynamics in the Scotia Arc region, in *Geodynamics of the Eastern Pacific Region, Caribbean, and Scotia arcs*, R. Cabre, ed, American Geophysical Union, Washington DC, 137-170.

Bird, P. (2003), An updated digital model of plate boundaries, *Geochem. Geophys. Geosyst. 4*(3), DOI:10.1029/2001GC000252.

Christensen, N. I. (1994), Poisson's ratio and crustal seismology, *J. Geophys. Res. 101*, 3139-3156.

Dziewonski, A. M. and D. L. Anderson (1981), Preliminary Earth reference model, *Phys. Earth Planet. Inter. 25*(4), 297-356.

Embley, R.W., W. W. Chadwick Jr., D. A. Butterfield, J. A. Resing, C. E.J. de Ronde, V. Tunnicliffe, J. E. Lupton, S. K. Juniper, K. H. Rubin, R. J. Stern, G. T. Lebon, K. Nakamura, S. G. Merle, J. R. Hein, D. A. Wiens, and Y. Tamura (2006), Long term eruptive activity at a submarine arc volcano, *Nature, 441*, 494-497, DOI:10.1038/nature04762.

Fryer, P. (1996), Evolution of the Mariana convergent plate margin system, *Reviews of Geophysics, 34*(1), 89-125.

Fryer, P., J. B. Gill, and M. C. Jackson (1997), Volcanologic and tectonic evolution of the Kasuga seamounts, northern Mariana Trough: *Alvin* submersible investigations, *J. Volcanol. Geotherm. Res., 79,* 277-311.

Hall, R., M. Fuller, J. R. Ali, and C. D. Anderson (1995), The Philippine Sea Plate: Magnetism and Reconstructions, in *Active Margins and Marginal Basins of the Western Pacific*, B. Taylor and J. Natland eds., American Geophysical Union, Washington DC, 371-404.

ISC, (2001), *On-line Bulletin*, http://www.isc.ac.uk, Internatl. Seism. Cent., Thatcham, UK.

Jordan, T. H. and K. A. Sverdrup (1981), Teleseismic location techniques and their application to earthquake clusters in the South-Central Pacific, *Bull. Seism. Soc. Am.*, *71*(4), 1105-1130.

Kato, T., J. Beavan, T. Matsushima, Y. Kotake, J. T. Camacho, and S. Nakao (2003), Geodetic ecidence of back-arc spreading in the Mariana Trough, *Geophys. Res. Lett.*, *30*(12), DOI:10.1029/2002GL016757.

Kennett, B. L. N. (1983), *Seismic Wave Propagation in a Stratified Media*, Cambridge Univ. Press, New York, NY.

Kennett, B. L. N. and E. Engdahl (1991), Traveltimes for global earthquake location and phase idendification, *Geophsy. J. Int.*, *105*, 429-465.

Kohut, E. J., R. J. Stern, A. J. R. Kent, R. L. Nielson, S. H. Bloomer, M. Leybourne (2006), Evidence for adiabatic decompression melting in the southern Mariana arc from high-Mg lavas and melt inclusions, *Contrib. Mineral. Petrol.*, *152*, 201-221, DOI:10.1007/s00410-006-0102-7.

Kubo, A. and E. Fukuyama (2003), Stress field along the Ryukyu Arc and in the Okinawa Trough inferred from moment tensors of shallow earthquakes, *Earth Planet. Sci. Lett.*, *210*, 305-316, DOI:10.1016/S0012-821X(03)00132-8.

Lahr, J. (1999), HYPOELLIPSE: A computer program for determining local earthquake hypocentral parameters, magnitude, and first-motion pattern (y2k compliant version), 1999 version 1.0, U.S. Geol. Surv., Reston, Va.

Langston, C. A. and D. V. Helmberger (1975), A procedure for modeling shallow dislocation sources, *Geophys. J. R. Aston. Soc.*, *42*, 117-130.

Martinez, F., P. Fryer, and N. Beker (2000), Geophysical characteristics of the southern Mariana Trough 11º50'N-13º40'N, *J. Geophys. Res.*, *105*(B7), 16,591-16,607.

McCaffery, R. (1996), Estimates of modern arc parallel starin rates in fore-arcs, *Geology*, *24*(1), 27-30.

Miller, M. S., A. Gorbatov, and B. L. N. Kennett (2006), Three-dimensional visualization of a near-vertical slab tear beneath the southern Mariana arc, *Geochem. Geophys. Geosyst.*, *7*, Q06012, doi:10.1029/2005GC001110.

Pavlis, G. L., F. Vernon, D. Harvey, and D. Quinlan (2004), The generalized earthquake-location (GENLOC) package: and earthquake-location library, *Computers and Geosciences*, *30*, 1079-1091, DOI:10.1016/j.cageo.2004.06.010.

Pozgay, S. H., R. A. White, D. A. Wiens, P. J. Shore, A. W. Sauter, and J. L. Kaipat (2005), Seismicity and tilt associated with the 2003 Anatahan eruption sequence, *J. Volcan. Geotherm. Res.*, *146*(1-3), 60-76.

Pozgay, S. H., D. A. Wiens, J. A. Conder, H. Shiobara, and H. Sugioka (2007), Complex mantle flow in the Mariana subduction system: evidence from shear wave splitting, *Geophys. J. Int.*, *107*(1), 371-386, DOI:10.1111/j.1365-246X.2007.03433.x

Quinlan, D. M., D. Harvey, and G. Wagner (1996), Datascope seismic application package, *Seismol. Res. Lett.*, *67*(2), 51.

Schellart, W. P. (2005), Influence of the subducting plate velocity on the geometry of the slab and migration of the subduction hinge, *Earth Planet. Sci. Lett., 231*, 197-219.

Schellart, W. P., J. Freeman, D. R. Stegman, L. Moresi, and D. May (2007), Evolution and diversity of subduction zones controlled by slab width, *Nature, 446*, 308-311

Shaw, P. R. (1994), Age variations of oceanic crust Poisson's ration: Inversion and a porosity evolution model, *J. Geophys. Res., 99*(B2), 3057-3066.

Stern, R. J., Jackson, M. C., Fryer, P., and Ito, E. (1993), O, Sr, Nd, and Pb isotopic composition of the Kasuga Cross Chain in the Mariana Arc: A new perspective on the K-h relationships, *Earth Planet. Sci. Lett., 119,* 459-476.

Stern, R. J. and N. C. Smoot (1998), A bathymetric overview of the Mariana forearc, *The Island Arc*, *7*, 525-540.

Stern, R. J., M. J. Fouch, and S. L. Klemperer (2003), An overview of the Izu-Bonin Mariana subduction factory, in *Inside the Subduction Factory*, edited by J. M. Eiler, pp. 175-222, AGU, Washington D.C.

Stern, R. J., E. Kohut, S. H. Bloomer, M. Leybourne, M. Fouch, and J. Vervoot (2006), Subduction factory processes beneath the Guguan cross-chain, Mariana arc: No

role for sediments, are serpentinites important?, *Contrib. Mineral. Petrol.*, *151*, 202-221, DOI:10.1007/s00410-005-0055-2.

Takahashi, N., S. Kodaira, S. L. Klemperer, Y. Tatsumi, Y. Kaneda, and K. Suyehiro (2007), Crustal structure and evolution of the Mariana intra-oceanic island arc, *Geology*, *4*(3), 203-206, DOI:10.1130/G23212A.1

Webb, S. C., T. K. Deaton, and J. C. Lemire (2001), A broadband ocean-bottom seismometer based on a 1-Hz natural period geophone, *Bull. Seism. Soc. Am*, *91*(2), 304-312.

Table 2.1: Earthquake source parameters determined by regional waveform inversion

Event ID*	Date (mm/dd/yyyy)	Origin Time[1]	Latitude	Longitude	Depth (km)[1]	Strike	Dip	Slip	Mw
6250316	6/25/2003	16:55:27	15.97	145.55	22	112	88	-61	3.73
6250322	6/25/2003	22:31:33	15.97	145.55	24	78	74	-27	3.49
7110300	7/11/2003	0:11:04	15.95	145.59	13	90	78	-18	3.72
8090313	8/9/2003	13:45:54	16.63	145.28	25	94	32	151	4.28
8130322	8/13/2003	22:53:09	15.95	145.55	21	0	48	-4	3.39
8170312	8/17/2003	12:40:08	15.97	145.55	18	75	77	-53	3.29

* Event ID corresponds to labels in figures 2.3-2.5
[1] Origin time and depth determined by relocation and fixed in waveform inversion

Table 2.2: Swarm Information

Swarm Description	Number of Earthquakes	Mean Latitude	Mean Longitude	Mean Depth	Mean 2σ Depth Uncertainty (km)	Mean Magnitude	Minimum Magnitude	Maximum Magnitude	Start Date (mm/dd/yyyy)	End Date (mm/dd/yyyy)
14°40'N/ Northwest Rota	64	14.62	144.91	31.1	Fixed in inversion*	4.12[2]	3.70[2]	4.90[2]	08/29/1997	10/09/1997
Diamante	111	15.96	145.55	17.4	2.4	3.20[1]	2.81[1]	4.12[1]	06/22/2003	9/5/2003
Northwest Sarigan	33	16.84	145.56	23.2	2.2	3.13[1]	2.71[1]	3.81[1]	12/15/2003	01/14/2004
16°40'N/ Mariana Trough	21	16.63	145.28	23.7	2.2	3.41[1]	2.59[1]	4.31[1]	07/04/2003	09/11/2003
Fore arc Teleseismic	13	16.55	145.98	28.5	Fixed in inversion*	4.75[2]	4.30[2]	5.30[2]	03/29/1990	04/29/1990
Fore arc Local	19	16.65	146.14	19.6	3.3	3.12[1]	2.64[1]	3.53[1]	10/01/2003	01/10/2004

M_{local} from Antelope database
M_b from ISC database
* Due to poor depth constraint from teleseismic P-wave arrivals, earthquake depths are fixed for relative relocations of teleseismic swarms.

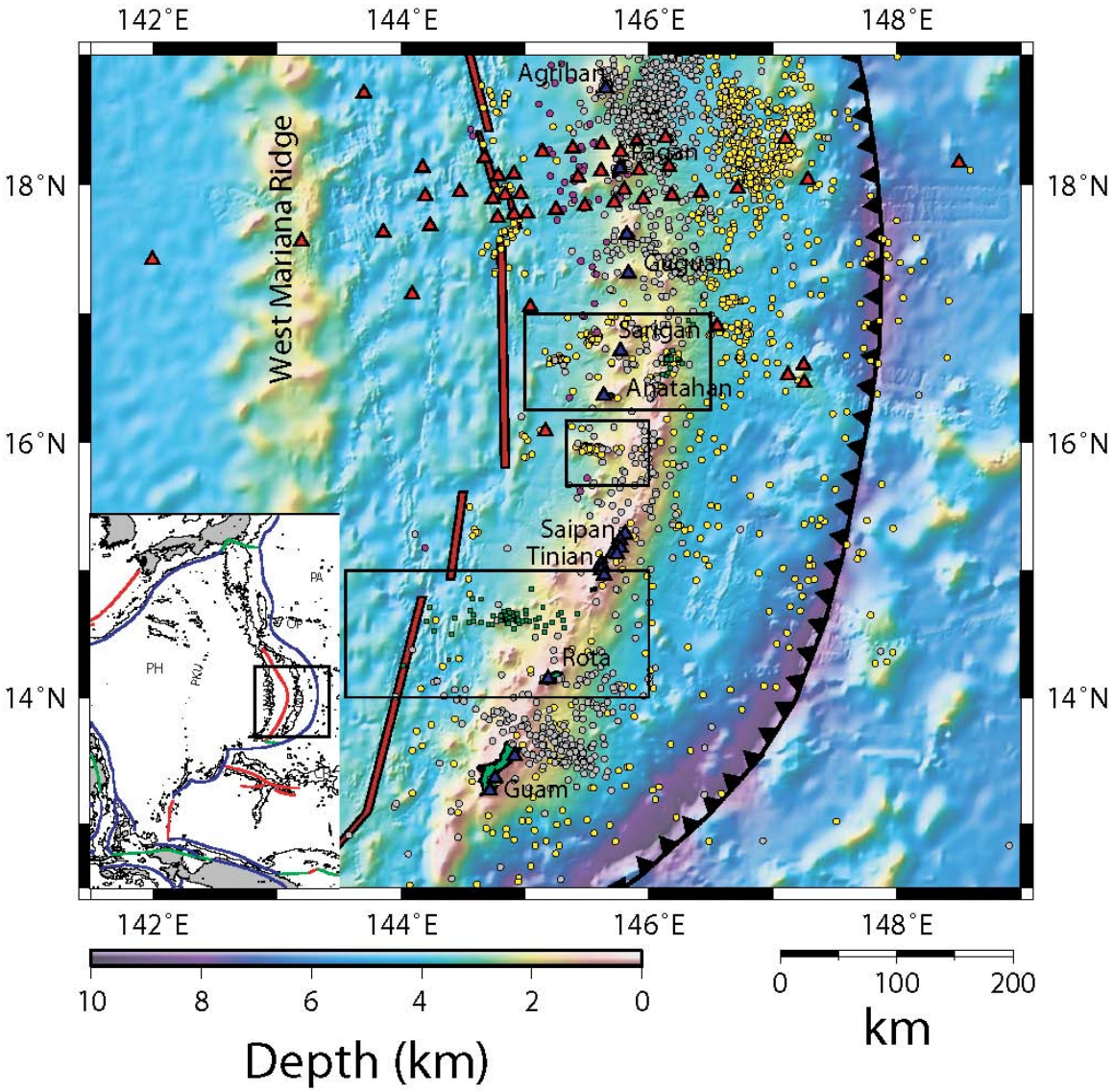

Figure 2.1: Bathymetric map of the Mariana Islands with stations marked as red and blue triangles (OBS and land stations respectively). Thick red line is spreading axis of the Mariana Trough and the thick, toothed black line marks trench location with teeth toward the overriding Mariana microplate. Shallow (0-70 km), intermediate (70-300 km), and deep (>300 km) earthquakes are plotted as yellow, grey, and purple circles respectively. Only the 2,194 best located earthquakes (those with more than 10 local arrivals and semi-major error axes of less than 5 km) are plotted here. Green squares represent teleseismically detected earthquake swarms that predate the deployment and are

discussed in this paper. Black boxes denote regions mapped in other figures. Inset: Regional map with black box around area of detail. Blue lines indicate trenches, red lines ridges, and green lines transform boundaries. The 2500 m isobath plotted to delineate major bathymetric highs. PA: Pacific Plate, PH: Philippine Plate, MA: Mariana Arc, WMR: West Mariana Ridge, PKU: Palau-Kyushu Ridge, OP: Ogasawara Plateau, CR: Caroline Ridge.

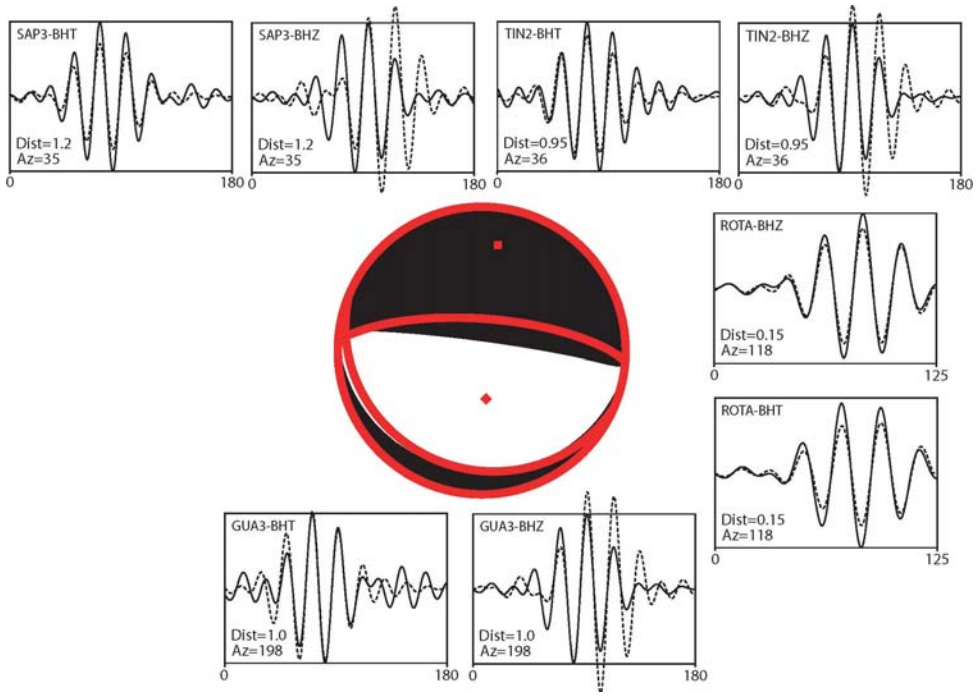

Figure 2.2: Example focal mechanism (red), in this case for test earthquake near Northwest Rota Seamount plotted over CMT solution (black). P and T axes are denoted by the red diamond and square respectively. Waveforms plotted near their respective positions with regard to the earthquake epicenter with event station distance and azimuth given in degrees. Solid line is data and dashed is synthetic, time on x-axis.

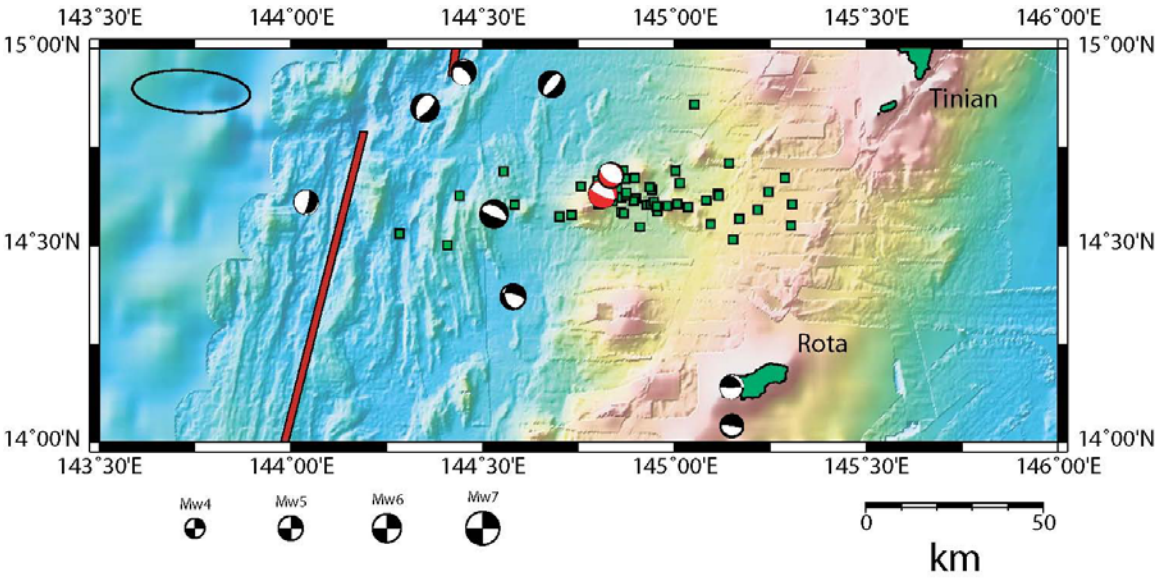

Figure 2.3: Shallow seismicity of the Northwest Rota region during the 1997 swarm. Events extending from the uplifted arc to the back-arc spreading center indicate and extensive region of deformation due to arc parallel stresses. CMT solutions for the region also indicated N-S extension. Green squares are relocated earthquakes, red CMTs are solutions for relocated events that occurred during the 1997 swarm, and black CMTs are other historical seismicity in the region that did not occur during the swarm and have not been relocated. Average 95% confidence ellipse plotted in upper left-hand corner. Due to poor earthquake depth resolution for shallow earthquakes located with teleseismic arrival times, the depths of the earthquakes are poorly constrained, and are therefore not plotted. Bathymetry color scale is the same as for figure 2.1.

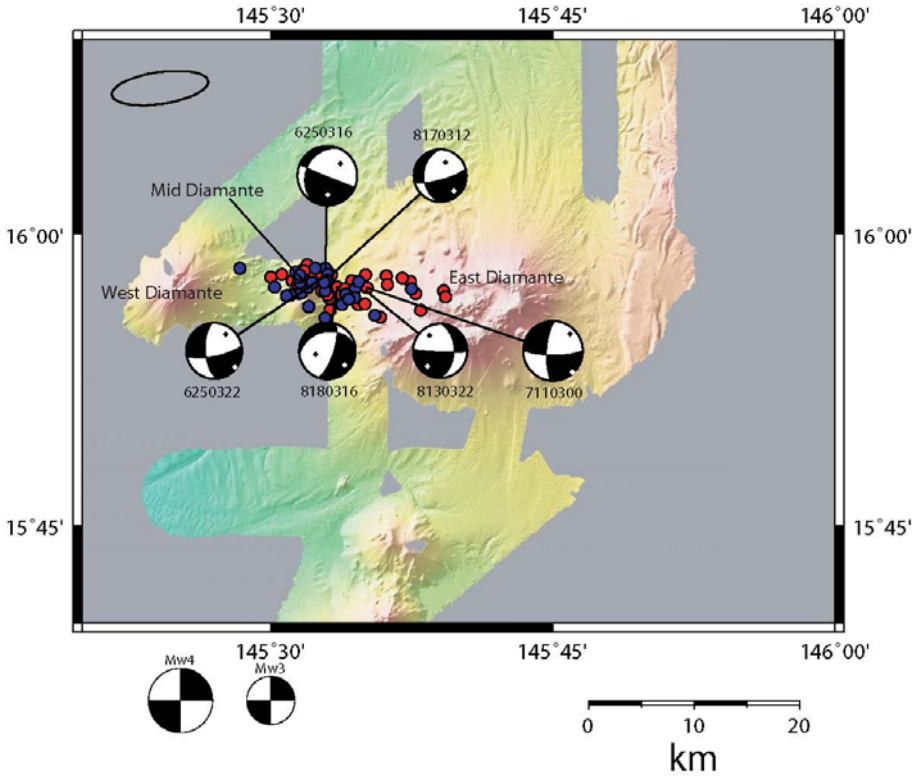

Figure 2.4: Detail of Diamante Cross-Chain area with focal mechanisms and earthquakes shown as red and blue circles representing earthquakes that are <20 km and >20 km deep respectively. East Diamante, mid-Diamante, and West Diamante seamounts are labeled. There is an E-W trending line of events centered over mid-Diamante Seamount. The focal mechanisms are largely consistent with an N-S extensional axis. Most share a steeply dipping E-W fault plane. Black and white diamonds on focal mechanisms represent compressional and tensional axes, respectively. Average 95% confidence ellipse plotted in upper left-hand corner. Bathymetry color scale is the same as for figure 2.1. (Bathymetry courtesy Robert Embley)

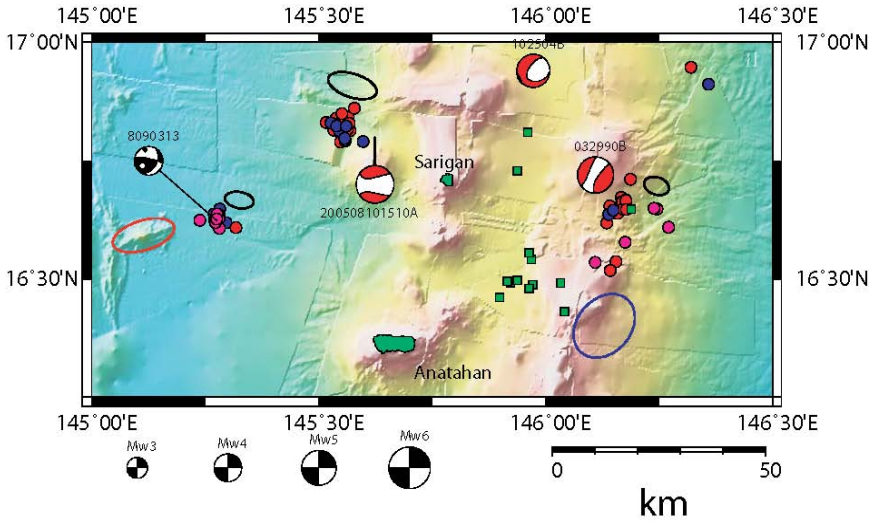

Figure 2.5: Region of Anatahan and Sarigan Islands where four swarms occurred. Earthquakes associated with the three locally detected earthquake swarms are shown as red (0-20 km), blue (20-30 km) and magenta (30-40 km) circles with average 95% confidence ellipses plotted in black near each swarm. The teleseismically detected earthquakes that predate (1990) our deployment are plotted as green squares with an average 95% confidence ellipse plotted in blue. The swarm at 16° 40'N is the only one, besides that at Diamante, for which a focal mechanism was determined. Its proximity to a small anomalous seafloor structure (red circled region) indicates potential contraction of the region between the arc and back-arc spreading center. The swarm near Northwest Sarigan along with a CMT solution for the same region suggests possible volcanic activity. The two swarms in the fore arc, of which the 1990 swarm is the most spread out, are likely the result of arc perpendicular stresses in the fore arc. Focal mechanism from this study is in black, those in red are from CMT catalog. Bathymetry color scale is the same as for figure 2.1.

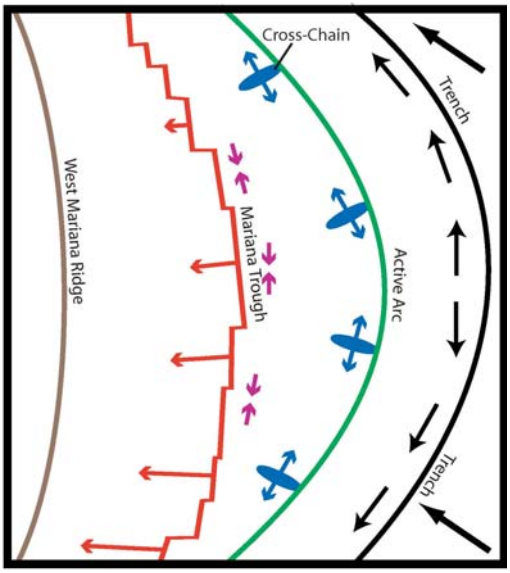

Figure 2.6: Schematic diagram of arc with showing processes causing along-strike extension. Heavy black, green, red and brown lines represent the trench, island arc, back-arc spreading center, and the West-Mariana Ridge respectively. Arc parallel extension occurs in the fore arc (black arrows) and in the arc (blue arrows) giving rise to cross-arc volcanism (blue ovals); compression (purple arrows) occurs in the back arc where increasing curvature of the arc system induces N-S compression.

Chapter 3

Aftershock locations following the May 3, 2006 M_w8.0 Tonga earthquake: Evidence for complex rupture

The Tonga subduction zone generally lacks a record of large thrust earthquakes, and is often described as decoupled. The May 3, 2006 M_w 8.0 Tonga earthquake has a Centroid Moment Tensor (CMT) solution consistent with either shallowly-dipping thrust faulting on the slab-plate interface, or reverse faulting on a steeply dipping plane. If the mainshock occurred on the thrust interface, the event would demonstrate that large thrust faulting earthquakes are possible in the Tonga trench, with important implications for tsunami risk in the region. We determine aftershock locations using a temporary seismograph deployment following the mainshock of May 3, as well as teleseismic arrival times reported by the ISC and local arrivals recorded by the sparse permanent Tonga seismic network. Most of the aftershock locations occur along a shallowly dipping feature extending from about 15 km to 55 km depth, which we interpret as the shallow thrust zone. We find that the initial mainshock rupture occurred within the downgoing slab Two distinct regions of aftershock seismicity are located. One downdip of the mainshock, along the shallow thrust interface, is likely triggered by the orientation of the mainshock. The second is a region of diffuse seismicity located updip of the mainshock and shows both convergent motion along the shallow thrust zone and extensional earthquakes representing bending in the downgoing plate. We suggest that the earthquake was a compound rupture, in which a slab-tearing event triggered slip

along the shallow thrust zone. Slip along the Tonga shallow thrust zone may often result from triggering by nearby earthquakes, as also suggested by the 2009 Samoa event.

Keywords: Tonga Subduction Zone, Shallow Seismicity, Slab Tearing, Subduction Zone Dynamics

3.1 Introduction

The Tonga subduction zone is considered anomalous in that it has not historically produced large shallow thrust such as those seen in other circum-Pacific subduction zones and typically does not produce large tsunamis (see [*Okal et al.*, 2004] for a review of historic large tsunamigenic events in the Tonga region). This has led researchers to assume the Tonga subduction zone is relatively decoupled with very limited capability for producing large earthquakes and damaging tsunamis [*Christensen and Ruff*, 1988; *Pacheco et al.*, 1993; *Ruff and Kanamori*, 1983]. [*Pacheco and Sykes*, 1992] analyzed large earthquakes that occurred between 1900 and 1989 and found only three of nineteen events in the Tonga region could be conclusively linked to thrust faulting. In addition, large normal faulting earthquakes [*Lundgren and Okal*, 1988] have been linked to decoupling between the overriding Australian Plate and the downgoing slab or complex deformation due to the subduction of the Louisville ridge which intersects the Tonga-Kermadec trench at about 26°S [*Christensen and Lay*, 1988].

However, the May 3, 2006 M_w8.0 earthquake is a large compressional earthquake that occurred in the vicinity of the shallow thrust zone and produced a small tsunami that was observed throughout the Pacific basin [*Tang et al.*, 2008]. The fault plane solution published by the global CMT project (Plane 1: strike=226°, dip=22°, slip=123°; Plane 2: strike=11°, dip=72°, slip=78°; depth=67.8 km; ISC depth=53.5 km) [*Dziewonski et al.*, 1981] and the tsunami raise questions concerning the earthquake mechanism and its relationship to the subducting Pacific plate. Did the earthquake occur on slab-plate interface and simply not produce large vertical displacements at the surface, did it rupture within the downgoing slab itself, or is the observed mainshock simply one part of a more

complex rupture? Answering these questions is essential to our understanding of tsunami risk associated with the Tonga subduction zone. In this study, we use results from a temporary array of seismometers deployed shortly after the mainshock as well as arrival times from global and local permanent seismic stations to show that the the initial mainshock occurred within the downgoing slab but that the overall rupture pattern is complex.

3.2 Methods and Data

We deployed seven stations across the southern portion of the Tonga archipelago (figure 3.1, table 3.1); three stations in the Tongatapu group and four in the Ha'apai group including one on the volcanic island, Tofua. Of the four sensors in Ha'apai, one (FOAM) was a Guralp 3-ESP broadband seismometer. The other six stations had Guralp 40-T semi-broadband seismometers, and all stations had Refraction Technologies RT-130 digital acquisition systems with GPS timing. Additional data from three permanently operating seismographs jointly operated by the Tongan government and the NEID in Japan were used. These consisted of two broadband stations, one each in Tongatapu and Va'vau and one short-period seismograph in Ha'apai. The temporary stations operated continuously for four months from June to mid-October (table 1). The remote location and logistical difficulties associated with deploying seismic stations in the Tonga archipelago prevented a truly rapid response. However, the first temporary station was deployed June 3 and the array was completed on June 19, 47 days after the mainshock table 1). During the time that the local array was incomplete, the local stations are used to detect teleseismic earthquakes.

Initial event detection was performed using the STA/LTA detection algorithm. Events were subsequently picked by hand for both P and S phases in an Antelope database [*Pavlis et al.*, 2004; *Quinlan et al.*, 1996]. Initial event location was done using the IASPEI91 velocity model [*Kennett and Engdahl*, 1991]. We isolate a large set of aftershocks during June and July that is distinct in location and timing from the other seismicity detected during the study period. We relocate all well located aftershocks and using the joint hypocentroidal decomposition method [*Jordan and Sverdrup*, 1981]. We limit our analysis to those aftershocks that have more than 10 arrivals and a maximum 95% confidence ellipsoid semiaxis length of less than 20 km. In addition to locally detected events, we utilize arrival data from the International Seismological Centre (ISC; http://www.isc.ac.uk) for the mainshock and for a number of aftershocks (table 2) which were also detected locally by the permanent network and for which there are Global CMT solutions [*Dziewonski et al.*, 1981]. During the period prior to the temporary deployment (May 3, 2006 to June 4) there were only three permanent stations of the Tonga local network operating, which do not provide enough data for good earthquake locations on their own. Therefore we only pick local arrivals for which there exists an origin based on teleseismic arrival data, and locate these events using the combined local and teleseismic data.

Also included in our data set is historical CMT data for the period 1976-2007 with ISC arrival information, which we use to better define the seismically active regions of the subduction zone within the study area. To test the influence of the historical CMT data on earthquake locations, we also ran a relocation inversion that did not contain these events. We found that while relative errors were smaller for the inversion that contained

only local events, earthquake locations were not significantly different. We utilize a 1-D velocity model for local arrivals that is based on the crustal structure of [*Crawford et al.*, 2003] underlain by PREM [*Dziewonski and Anderson*, 1981]. Travel-times for teleseismic arrivals are calculated using IASPEI91 [*Kennett and Engdahl*, 1991]. The relocation of events using both teleseismic and local arrivals significantly reduces location uncertainties. The teleseismic arrivals better constrain lateral resolution which is limited due to station geometry of the local array, and the local arrivals aid in constraining the depth of the events [*Stein and Wysession*, 2003], eliminating some of the tradeoff between depth and origin time.

3.3 Results

In all, we relocate 411 events: 287 aftershocks with only local data; 49 with both local and teleseismic arrivals; and 75 historical CMTs that occur outside the deployment period of our temporary array. Twenty-three of the located aftershocks also had CMT solutions (table 2). We find the mainshock to have a depth of 70.7±3.5 km to two standard deviations. The global CMT project estimates a depth of 67.8 km and the ISC estimate of focal depth is 53.5 km. The average uncertainty of the earthquake locations (here considered to be the mean of the three semi-axes of the 95% confidence ellipsoids) is 7.2 km with a standard deviation of 3.8 km. If we discard the historical CMT data for which the depth uncertainties are higher, the average uncertainty is 6.2 km with a standard deviation of 2.5 km.

The results clearly show a dipping plane of seismicity that intersects the trench axis if extended upward, which we interpret as the shallow thrust zone. The mainshock

hypocenter is located about 32 km below the shallow thrust zone within the downgoing Pacific plate. There are three regions of significant seismicity following the mainshock. The majority of the aftershocks occurred along the plate interface downdip of the mainshock. The updip seismicity occurs in two lobes; one extending north-northeast of the mainshock and the other south-southeast (figure 3.3). While the majority of the teleseismically detected aftershocks occur prior to the temporary deployment and updip of the mainshock, there is no strong correlation between the timing of the earthquakes and their location. We interpret the lack of time dependent location to mean that the entire aftershock region deformed in a complex manner following the mainshock of May 3.

3.4 Discussion

3.4.1 Aftershock Locations

Aftershock locations (figure 3.3) following the May 3, 2006 Tonga earthquake indicated a complex system of deformation in the shallow thrust zone of the Tonga subduction zone. The mainshock location is well constrained in both the CMT solution, and in our relocation (figure 3.3). Based on the position of the mainshock, the slab surface predicted by [*Hayes et al.*, 2009], and the location of locally detected seismicity we conclude that the primary mainshock occurred within the subducting slab, not along the shallow thrust zone. However, in light of the recent (29 September 2009) tsunamigenic earthquake near Samoa [*Beavan et al.*, 2010; *Lay et al.*, 2010], we cannot rule the possibility of a complex rupture with slip occurring first on the steeply dipping plane followed a short time (seconds) by an earthquake occurring on a shallowly dipping

plane. Based on aftershock locations and the complexity of seismicity following the mainshock, a complex rupture is the preferred interpretation. The majority of the aftershocks detected are located downdip of the mainshock along what we infer to be the slab interface (figure 3.3). The updip seismicity is of a more distributed nature both laterally and vertically (figures 3.2, 3.3). It is however, concentrated in two lobes extending NNE and SSE around the mainshock. The distribution of updip and downdip seismicity relative to the mainshock has important implications for the geometry of the mainshock fault.

3.4.2 Downdip Seismicity

The majority of earthquakes recorded by the temporary deployment are located downdip of the mainshock. These locations are consistently downdip of the observed shallow thrust interface (figure 3.2) in the region. We note that the the aftershock region on the shallow thrust zone extends to ~55 km depth, which may correspond to the downdip limit of seismic slip on this segment of the subduction interface. Studies of earthquake triggering and Coulomb stress transfer have noted increased activity along thrust interfaces downdip of large subduction related faults [*Freed*, 2005; *Lin and Stein*, 2004]. These studies are limited to only those earthquakes that occur on the shallow subduction interface, however. This supports that concept of a complex rupture with a secondary earthquake on the subduction interface occurring shortly after the initial mainshock in the downgoing slab. The earthquake locations and small magnitudes ($\overline{M}_l$=3.94) suggest that the mainshock of May 3 cause the normal stress on the plate-slab interface to be reduced along the shallow thrust zone downdip of the mainshock location

and/or an increase in shear stress on this interface. Very few CMTs consistent with thrust faulting are observed in this region either before or during the deployment period (figure 3.2). We conclude that the reduction of stress on the shallow thrust zone was not sufficient to allow large portions of the fault zone to rupture. Rather small asperities along the fault zone failed rapidly, producing the large number of small earthquakes we observe. Alternatively, a complex rupture during the mainshock in which the subduction interface ruptured shortly after the primary mainshock may have ruptured the subduction interface entirely within the aftershock region outlined in figure 3.3. This would indicate the aftershock region associated with subduction interface outlined in blue in figure 3.3 is representative of the slip region of the mainshock and may represent a region of otherwise 'slow slip' that failed seismically as a result of the mainshock.

3.4.3 Updip seismicity

The updip seismicity is more distributed laterally than that which occurs downdip of the mainshock. The general pattern of seismicity is defined by two lobes, one extending to the north-northeast of the mainshock and one to the south-southeast. These lobes also correspond to the foci of teleseismic aftershocks during the study period. These focal mechanisms are not consistent with a single mode of deformation, rather they suggest that the slab updip of the mainshock deforms in a complex manner. Eight focal mechanisms are indicative of normal faulting (figure 3.2, 3.3). There are very few normal faulting mechanisms in the historical CMT record for this region (figure 3.2 - black), so we interpret this style of deformation to be unusual for this region. This may indicate that the mainshock ruptured a large portion of the thickness of the downgoing

plate, further uncoupling it from the overriding plate. An alternative hypothesis is that a complex rupture occurred in which the mainshock initiated at the CMT location, with secondary rupture occurring in the region of observed downdip aftershocks. The normal faulting observed updip is then consistent with other observed mainshock-aftershock sequences for shallow thrust faulting [*Ammon et al.*, 2008; *Christensen and Ruff*, 1988; *Dmowska et al.*, 1988] Most CMTs are within 20 km of the slab surface. This suggests that there is significant extensional stress within the uppermost regions of the downgoing slab. However, since these events are located farthest from the regional array, they are the most poorly located. It is possible that they represent an increase in bending stress of the uppermost Pacific plate due to the mainshock rupture path.

3.4.4 Seismic Evidence for a complex rupture

When taken together, the mainshock-aftershock sequence of the May 3, 2006 Tonga earthquake suggests a complex rupture. Aftershocks occurring along the shallow thrust zone with limited updip normal faulting is consistent with more 'typical' plate interface events [*Ammon et al.*, 2008; *Dmowska et al.*, 1988]. The caveat, of course, is that the locations of both the initial mainshock and the aftershocks with normal fault focal mechanisms are located downdip of their expected locations [*Ammon et al.*, 2008; *Christensen and Ruff*, 1988; *Dmowska et al.*, 1988]. We hypothesize that the mainshock likely initiated within the downgoing Pacific plate with subsequent rupture along the shallow thrust interface. This secondary mainshock is located downdip of the typical zone of interplate thrust faulting in the Tonga subduction zone (figure 3.2) and is highlighted by the aftershock locations along the interplate interface (blue region in

figure 3.3). The region updip of the mainshock was placed in tension because of the mainshock sequence, a hypothesis borne out by the presence and concentration of normal faulting focal mechanisms in the region, which are atypical for the region they are observed in this study. Researchers have observed complex rupture in the Tonga subduction zone before, most notable the recent tsunamigenic earthquake sequence in Samoa [*Bevan et al.*, 2010; *Lay et al.*, 2010]. Furthermore, complex rupture has also been observed in other subduction zones [*Beck and Ruff*, 1985; *Bilek et al.*, 2003]. Unlike the 2009 Somoa earthquake, however, the relative locations of the initial mainshock and the 'secondary' event are vertically oriented rather than horizontally, limiting our ability to pick them apart using GPS coseismic deformational analysis [*Beavan, et al.*, 2010] or back propagation [*Lay, et al.*, 2010].

3.5 Conclusions

The May 3, 2006 earthquake is one of the first large subduction related thrust earthquakes instrumentally observed in the Tonga subduction zone. Observations of subsequent aftershocks and a comprehensive relocation of earthquakes related to the mainshock-aftershock sequence indicates that the mainshock was a complex rupture in which faulting initiated within the downgoing slab with secondary slip occurring along the plate interface. The aftershock sequence follows a pattern of interplate thrust faulting with intraplate normal faulting seen in other subduction zones. However, due to the more arcward setting of the mainshock, we observe normal faulting not in the outer rise but rather in the shallow thrust zone. The anomalous level of earthquakes occurring within

the region downdip of the historically observed shallow thrust zone indicates an activation of an otherwise non-seismogenic portion of the plate interface region.

3.6 Acknowledgements

The authors wish to thank Patrick Shore, Jim Whatman, Anna-Liisa Lahtinen, and Tevida Fatai for help in deploying seismographs in Tonga and PASSCAL and Geoscience Australia for seismic instrumentation. We also wish to acknowledge the Geology Section of the Ministry of Lands, Survey, and Natural Resources, Kingdom of Tonga for logistical support during the experiment and the National Research Institute for Earth Science and Disaster Prevention (NEID) in Japan for access to data collected by the Tonga Network. Additionally, we would like to acknowledge the global CMT project (http://www.globalcmt.org) and the International Seismological Centre (http://www.isc.ac.uk) for moment tensor and arrival time data respectively. We thank (somebody I'm sure) for helpful reviews of this manuscript. This work is funded by NSF grant EAR-0637035. Figures were produced using GMT [*Wessel and Smith*, 1998].

3.7 References

Ammon, C. J., H. Kanamori, and T. Lay (2008), A great earthquake doublet and seismic stress transfer cycle in the central Kuril islands, *Nature*, *451*, 561-565, doi:10.1038/nature06521.

Beavan, J., X. Wang, C. Holden, K. Wilson, W. Power, G. Prasetya, M. Bevis, and R. Kautoke (2010), Near-simultaneous great earthquakes at Tongan megathrust and outer rise in September 2009, *Nature*, *466*, 959-963, doi:10.1038/nature09292.

Beck, S. L., and L. Ruff, J. (1985), The rupture process of the 1976 Mindanao earthquake, *J. Geophys. Res.*, *90*(B8), 6773-6782.

Bilek, S. L., S. Y. Schwartz, and H. R. DeShon (2003), Control of seafloor roughness on earthqake rupture behavior, *Geology*, *31*(5), 455-458.

Christensen, D. H., and L. Ruff, J. (1988), Seismic coupling and outer rise earthquakes, *J. Geophys. Res.*, *93*(B11), 13,421-413,444.

Christensen, D. H., and T. Lay (1988), Large earthquakes in the Tonga region associated with subduction of the Louisville Ridge, *J. Geophys. Res.*, *93*(Bll,), 13,367-313,389.

Coffin, M. F., L. M. Gahagan, and L. A. Lawver (1998), Present-day Plate Boundary Digital Data Compilation, *University of Texas Institute for Geophysics Technical Report 174*, 5 pp.

Crawford, W. C., J. A. Hildebrand, L. M. Dorman, S. C. Webb, and D. A. Wiens (2003), Tonga Ridge and Lau Basin crustal structure from seismic refraction data, *J. Geophys. Res.*, *108*(B4), 2195, doi:10.1029/2001JB001435.

Dmowska, R., J. R. Rice, L. C. Lovison, and D. Josell (1988), Stress transfer and seismic phenomena in coupled subduction zones during the earthquake cycle, *J. Geophys. Res.*, *93*(b7), 7869-7884.

Dziewonski, A. M., and D. L. Anderson (1981), Preliminary reference Earth model, *Phys. Earth Planet. Int.*, *35*(4), 297-356, doi:10.1016/0031-9201(81)90046-7.

Dziewonski, A. M., T.-A. Chou, and J. H. Woodhouse (1981), Determination of earthquake source parameters from wavform data for studies of global and regional seismicity, *J. Geophys. Res.*, *86*(B4), 2825-2852.

Freed, A. M. (2005), Earthquake triggering by static, dynamic, and postseismic stress transfer, *Annu. Rev. Earth Planet. Sci.*, *33*, 335-367, doi:10.1146/annurev.earth.33.092203.122505.

Hayes, G. P., D. J. Wald, and K. Keranen (2009), Advancing techniques to constrain the geometry of the seismic rupture plane on subduction interfaces a priori: Higher-order functional fits, *Geochem. Geophys. Geosys.*, *10*, Q09006, doi:10.1029/2009GC002633.

Jordan, T. H., and K. A. Sverdrup (1981), Teleseismic location techniques and their application to earthquake clusters in the South-Central Pacific, *Bull. Seism. Soc. Am.*, *71*(4), 1105-1130.

Kennett, B. L. N., and E. Engdahl (1991), Traveltimes for global earthquake location and phase identification, *Geophys. J. Int.*, *105*, 429-465, doi:10.1111/j.1365-246X.1991.tb06724.x.

Lay, T., C. J. Ammon, H. Kanamori, L. Rivera, K. D. Koper, and A. R. Hutko (2010), The 2009 Samoa-Tonga great earthquake triggered doublet, *Nature*, *466*, 964-968, doi:10.1038/nature09214.

Lin, J., and R. S. Stein (2004), Stress triggering in thrust and subduction earthquakes and stress interaction between the southern San Andreas and nearby thrust and strike-slip faults, *J. Geophys. Res.*, *109*, B02303, doi:10.1029/2003JB002607.

Lundgren, P. R., and E. A. Okal (1988), Slab decoupling in the Tonga Arc: The June 22, 1977 earthquake, *J. Geophys. Res.*, *93*(B11), 13,355-313,366.

Okal, E. A., J. Borrero, and C. E. Synolakis (2004), The earthquake and tsunami of 1865 November 17: evidence for far-field tsunami hazard from Tonga, *Geophys. J. Int.*, *157*, 164-174, doi:10.1111/j.1365-246X.2004.02177.x.

Pacheco, J. F., and L. R. Sykes (1992), Seismic moment catalog of large shallow earthquakes, 1900 to 1989, *Bull. Seism. Soc. Am.*, *82*(3), 1306-1349.

Pacheco, J. F., L. R. Sykes, and C. H. Scholz (1993), Nature of seismic coupling along simple plate boundaries fo the subduction type, *J. Geophys. Res.*, *98*(B8), 14133-14159.

Pavlis, G. L., F. Vernon, D. Harvey, and D. Quinlan (2004), The generalized earthquake location (GENLOC) package: An earthquake-location library, *Comput. Geosci.*, *30*, 1079-1091, doi:10.1016/j.cageo.2004.06.010.

Quinlan, D. M., D. Harvey, and G. Wagner (1996), Datascope seismic application package, *Seismol. Res. Lett.*, *67*(2), 51.

Ruff, L., J., and H. Kanamori (1983), Seismic coupling and uncoupling at subduction zones, *Tectonophysics*, *99*, 99-117.

Stein, S., and M. Wysession (2003), *An Introduction to Seismology, Earthquakes, and Earth Structure*, Blackwell Publishing, Malden, MA, USA.

Tang, L., V. V. Titov, Y. Wei, H. O. Mofjeld, M. Spillane, D. Arcas, E. N. Bernard, C. Chamberlin, E. Gica, and J. Newman (2008), Tsunami forecast analysis for the May 2006 Tonga tsunami, *J. Geophys. Res.*, *113*(C12), C12015, doi:10.1029/2008JC004922.

Wessel, P., and W. H. F. Smith (1998), New, improved version of Generic Mapping Tools released, *Eos. Trans. AGU*, *79*(47), 579.

Table 3.1: Station locations and operating dates. Stations that are part of the permanent network denoted by a *. Station types: SBB – Guralp 40-T, BB – broadband seismometer, SP – short period seismometer. On/off dates for temporary network denote installation/removal.

Station	Latitude	Longitude	Type	On Date	Off Date
EUAS	-21.44	-174.91	SBB	06/06/06	10/11/06
TPU	-21.15	-175.18	BB	---	---
NUIA	-21.06	-175.32	SBB	06/03/06	10/13/06
ATA	-21.06	-175.00	SBB	06/19/06	10/12/06
TKVA	-20.32	-174.52	SBB	06/11/06	10/16/06
NMKA	-20.26	-174.80	SBB	06/09/06	10/16/06
HAP	-19.83	-174.35	SP	---	---
FOAM	-19.74	-174.29	BB	06/12/06	10/14/06
TOFA	-19.71	-175.06	SBB	06/14/06	10/17/06
VAV	-18.66	-173.98	BB	---	---

Table 3.2 Summary of relocated CMTs during the study period for which local arrival data exists. M_w from CMT solution, M_l from P-S amplitude ratio recorded by local array. Origin information is final location, arrivals include both teleseismic arrivals from ISC and local arrivals recorded by temporary and permanent arrays in Tonga, uncertainty is average of the 3 semiaxes for the 95% uncertainty ellipsoid. Event number corresponds to CMT plotted in figures 3.2 and 3.3.

Event Number	Date MM/DD/YYYY	Origin Time HH:MM:SS	Latitude °N	Longitude °E	Depth (km)	M_W	M_L	Arrivals	Relative Uncertainty (km)
1	05/03/2006	15:26:41	-20.10	-173.99	70.71	8.0	7.5	303	3.4
2	05/04/2006	11:25:27	-20.64	-173.75	16.39	5.9	5.6	196	5.7
3	05/05/2006	04:19:43	-20.25	-173.68	27.75	5.5	5.8	205	4.2
4	05/05/2006	05:33:25	-19.92	-173.44	19.54	5.2	5.6	113	4.7
5	05/05/2006	06:16:18	-19.84	-174. 34	21.07	5.9	6.6	174	3.8
6	05/05/2006	08:49:08	-19.92	-173.71	24.94	5.1	4.8	63	8.2
7	05/07/2006	02:33:47	-20.10	-174.15	39.12	5.6	5.3	170	4.6
8	05/07/2006	12:30:33	-20.05	-173.82	38.24	4.9	5.0	75	6.1
9	05/07/2006	22:06:25	-20.12	-173.75	39.74	4.9	4.7	49	8.0
10	05/09/2006	10:27:52	-19.87	-174.28	7.36	5.1	6.0	75	6.0
11	05/14/2006	04:54:15	-20.11	-174.27	42.22	5.0	5.6	77	4.9
12	05/16/2006	20:55:49	-20.71	-173.83	21.03	5.7	5.6	169	4.8
13	05/17/2006	03:06:17	-20.66	-173.76	16.00	5.8	6.3	193	4.2
14	05/17/2006	21:57:50	-20.70	-173.74	16.90	5.5	6.2	142	4.4
15	05/28/2006	03:36:19	-19.93	-174.26	54.22	5.7	6.2	218	3.8
16	06/01/2006	22:31:27	-20.16	-173.56	29.24	4.9	5.0	159	5.7
17	06/02/2006	01:28:26	-20.17	-173.50	19.78	5.1	5.1	211	5.0
18	06/02/2006	06:59:42	-20.12	-173.55	29.48	5.2	4.8	102	4.8
19	06/03/2006	13:26:54	-20.97	-173.83	23.54	5.1	5.1	53	7.0
20	06/03/2006	15:27:51	-20.55	-174.10	25.64	5.2	5.2	187	4.9
21	06/17/2006	03:45:59	-20.04	-174.21	68.74	4.9	5.2	182	3.1

22	06/28/2006	13:00:30	-20.80	-173.82	45.65	5.0	4.9	49	4.9
23	07/05/2006	03:44:10	-20.58	-173.83	20.53	5.6	6.0	257	3.1

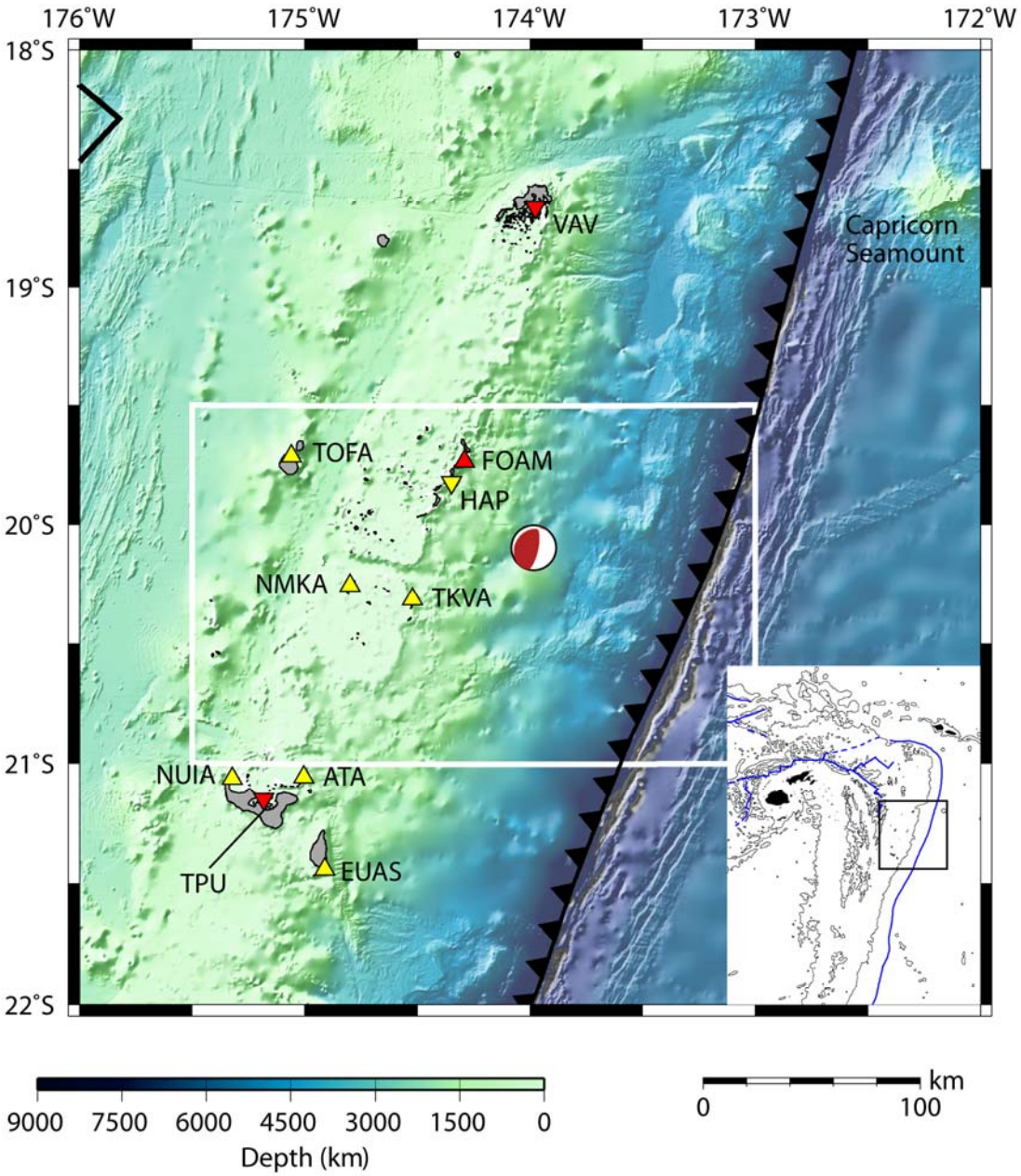

Figure 3.7: Map of station locations with upright triangles and inverted triangles representing temporary and permanent stations respectively. Broadband stations are in red, and semi-broadband and short period stations are plotted in yellow. Station name and Capricorn Seamount labeled on map. The trench axis is denoted by a heavy, toothed black line, and the Lau spreading is center marked with heavy black line. Region of figures 3.2 and 3.3 is bounded by heavy white line, and the mainshock focal mechanism

from the globalCMT catalog is plotted at it updated location. Plate boundaries plotted on map are from the PLATES project [*Coffin et al.*, 1998]. Inset: Regional setting of array. Study region outlined in black, blue lines plate denote plate boundaries. 2500m bathymetric contour plotted to denote major structural features. Color scale is constant throughout.

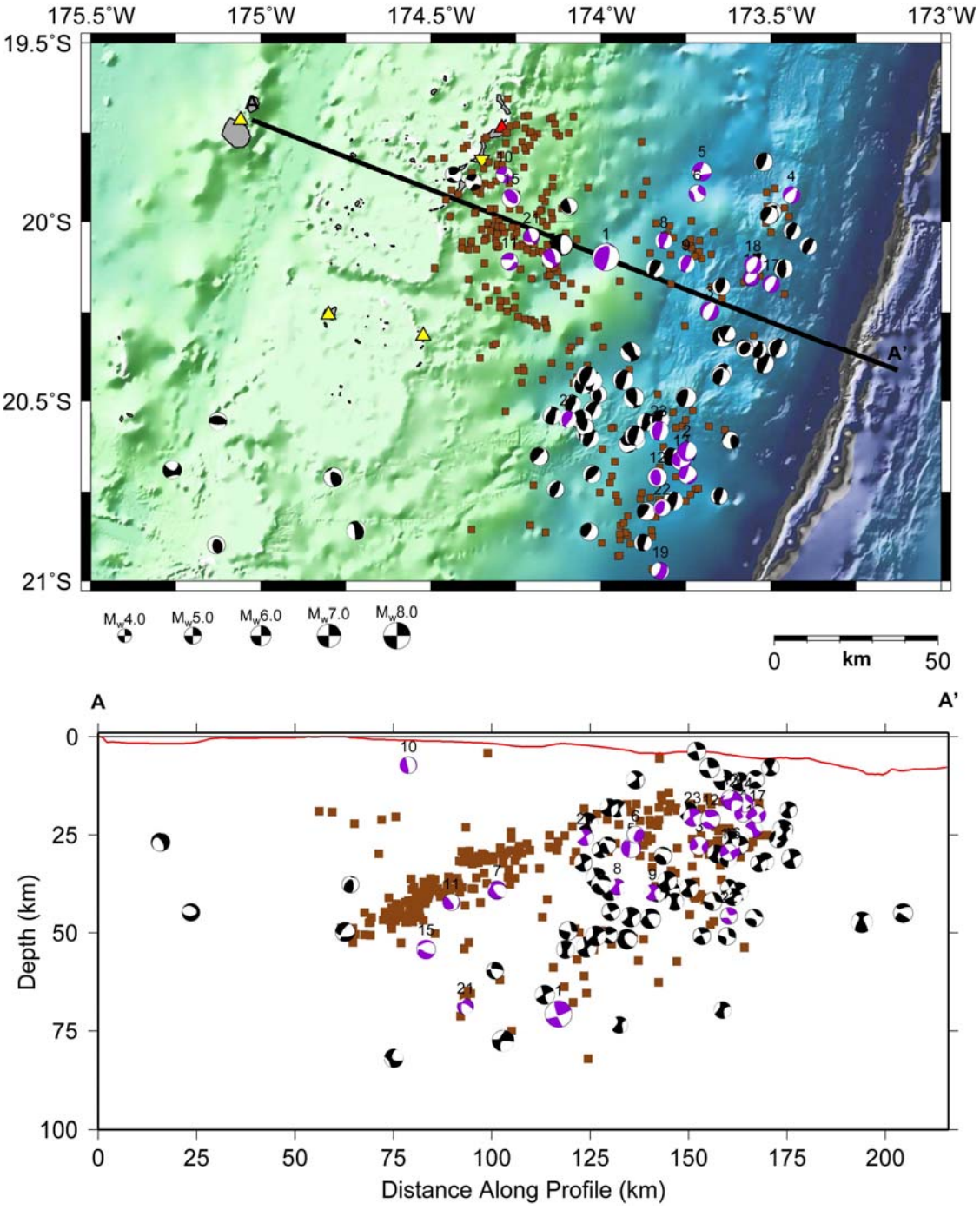

Figure 3.2: Map (upper) and cross-section (lower) of relocated seismicity. Locally detected earthquakes in brown, locally detected CMTs in violet, historical CMTs in black (1976-2007). Historical CMTs are located well laterally, but depth precision is poor due to the lack of permanent seismic stations in the Tonga archipelago. Heavy black line is

profile location in lower. Bathymetric profile in red. Mainshock of May 3, 2006 occurred within the down going slab. Majority of aftershocks occur down dip of mainshock. Two lobes of updip seismicity are apparent in map view. Bathymetric scale same as in figure 3.1. Numbers above locally detected CMTs correspond to table 2.

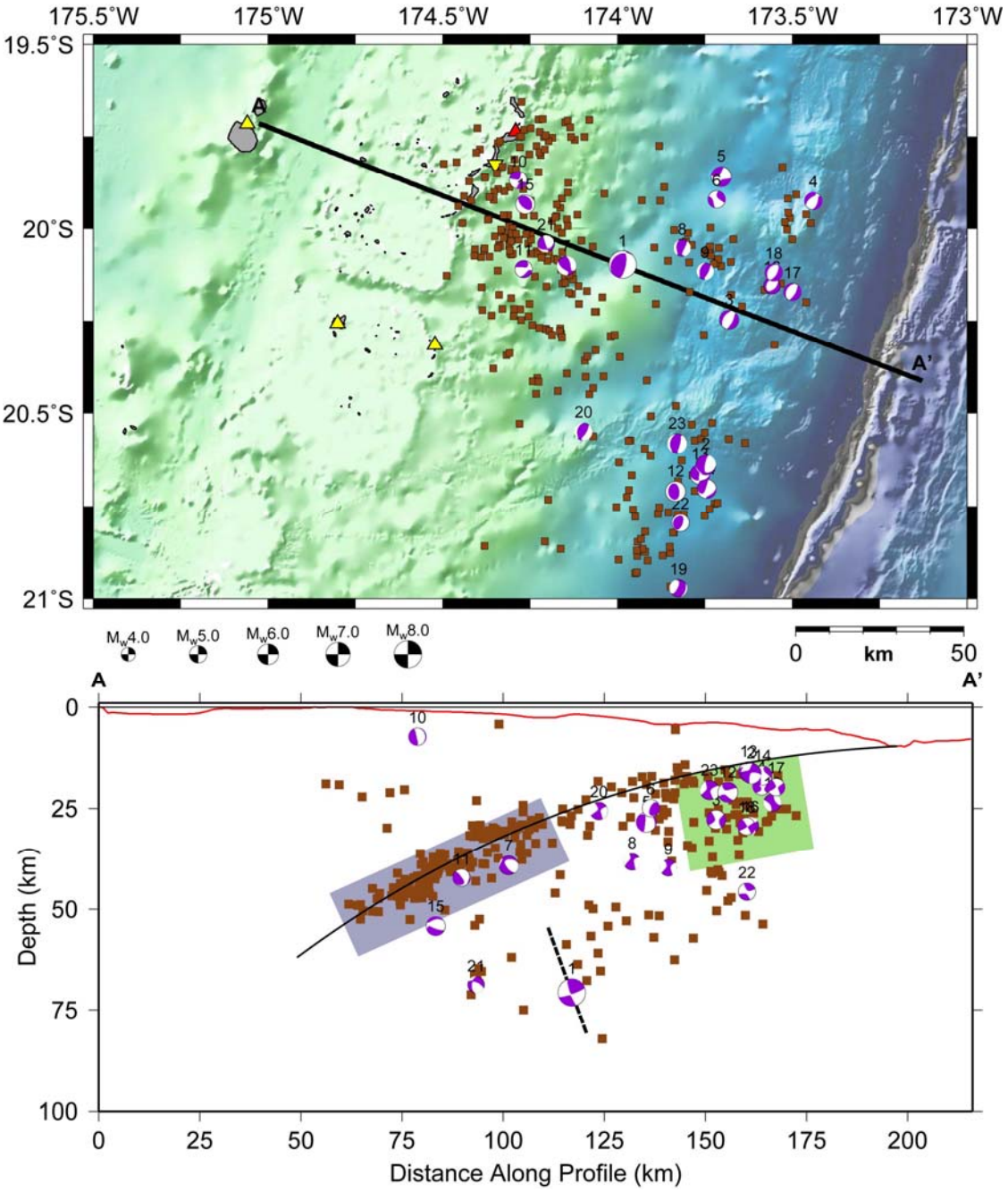

Figure 3.3: Same as figure 3.2 with historic data removed. Cross section of locally detected seismicity has tectonic interpretations. Dashed black line - preferred fault plane of mainshock; red line – bathymetric profile; heavy black line – interpreted slab interface; blue rectangle - zone of thrust faulting along plate-slab interface; green rectangle: zone of slab tension. Numbers above CMT correspond table 2.

Chapter 4

Shear velocity structure of the Gamburtsev Subglacial Mountains, East Antarctica from inversion of teleseismic Rayleigh waves

The Gamburtsev Subglacial Mountains (GSM), located near the center of East Antarctica, remain one of the least explored and most enigmatic mountain ranges on earth, and their geological history is almost totally unconstrained. We utilize teleseismic Rayleigh wave data from a two-year deployment of 28 broadband seismic stations across the region to image the shear velocity structure of the GSM and surrounding regions. We utilize the two plane-wave method of *Forsyth and Li* [2005] to perform phase velocity inversions. These phase velocities are then inverted for shear velocity and refine by conducting Monte Carlo modeling. Beneath the core of the GSM, we observe crustal thicknesses in excess of 55 km. Additionally, we see shear velocities in the mantle that remain faster than AK135 to depths of more than 200 km. Crustal thickness and mantle velocities in the surrounding regions are consistent with a cratonic setting. The extension of the Lambert Graben into the northern part of the study region can clearly be seen in the phase and shear velocity inversions. We compare our 1-D phase velocity results with global phase velocity maps and crustal ages. We find that our phase velocity structure is most consistent with Early-Middle Proterozoic regions globally. Radiometric age dates for zircons believed to have come from the GSM are consistent with a Neoproterozoic to Early Paleozoic origin for the mountains. The mechanism of long-term support for such an old mountain belt is an open question. An extremely low erosion rate coupled with a

viscous cratonic lithosphere that limits crustal delamination may allow for the continued presence of high elevations in the GSM.

Keywords: Antarctica, Gamburtsev Subglacial Mountains, Shear Velocities, Crustal Structure, Mantle Structure, Phase Velocities

4.1 Introduction

The Gamburtsev Subglacial Mountains (GSM) are located near the center of the East Antarctic Ice Sheet underlying Dome Argus (figure 4.4.1a). With bedrock elevations in excess of 2000m [*Bo et al.*, 2009; *Lythe et al.*, 2001], this region is a proposed nucleation point for the formation of the continental ice sheets at ~34Ma [*DeConto and Pollard*, 2003a; b]. However, despite the region's importance for our understanding of past climate change, the topography of the GSM has been poorly constrained prior to the recent International Polar Year (IPY) efforts . The subglacial bedrock topography model, BEDMAP [*Lythe et al.*, 2001], indicates that the GSM are defined by a large plateau surrounded by regions of lower topography (figure 4.1b). However, the resolution of the BEDMAP model is too low to give any indication of what, if any topographic relief occurs within the GSM. Recent ground based and airborne radar surveys indicate that there is a large amount of relief within the GSM province [*Bell et al.*, 2009; *Bo et al.*, 2009; *Ferraccioli et al.*, 2010; *Jordan et al.*, 2009; *Wolovick et al.*, 2009]. The amount of observed topographic relief and the overall pattern and structure of valleys suggest that there has been both fluvial and glacial erosion.

Persistent questions regarding the origin of the GSM are their mechanism of uplift and age. These questions have important implications for the development of glaciers and ice sheets within central East Antarctica [*DeConto and Pollard*, 2003b]. Historically, it has been assumed that the central region of Antarctica is composed of a single Archean aged crustal block [*Tingey*, 1991]. More recent studies have suggested a more complicated tectonic history for the region [*Boger*, 2011; *Fitzsimons*, 2003; *Studinger et al.*, 2003], though the interior of East Antarctica is still believed to be

comprised of Archean and Early Proterozoic crustal blocks. A fundamental question, then, is how a mountain range can exist within a region of little to no tectonic activity over the last several hundred million years. Researchers have suggested that they are a thermally supported plateau [*Sleep*, 2006] or the result of far field stresses related to the formation of Pangea during the late Carboniferous – early Permian [*Veevers*, 1994; *Veevers et al.*, 2008a; *Veevers et al.*, 2008b]. A variation on this idea is a two stage uplift in which the crust was thickened during the Early Permian and additional uplift occurred during the Cretaceous during rifting in the Lambert Graben due to the breakup of Gondwana [*Lisker et al.*, 2003; *Phillips and Läufer*, 2009]. Other researchers have suggested that the GSM formed during multiple late Proterozoic – early Paleozoic orogenic events that led to the formation of Gondwana [*Fitzsimons*, 2000; 2003; *Liu et al.*, 2002; *Liu et al.*, 2006; *Zhao et al.*, 1995]. Despite the importance of the GSM in our understanding of Antarctic tectonics and speculation regarding their provenance, no direct observations of their geology exist due to the thick ice cover (>1000m). Recent geochronology results from an ODP site in Prydz Bay have dated detrital zircons to 529-546Ma [*van de Flierdt et al.*, 2008; *Veevers et al.*, 2008a] supporting a Neoproterozoic or early Paleozoic origin for the region, possibly related to the formation of Gondwana.

Comprehensive studies of crust and upper mantle structure are also lacking for the Gamburtsevs. Previous seismological investigations of the region are limited to continent wide studies using global datasets [*Morelli and Danesi*, 2004; *Ritzwoller et al.*, 2001; *Roult and Rouland*, 1992] and have lateral resolutions greater than 500 km. While these studies have shown that the structure of the Gamburtsev Mountains is defined by a thickened lithosphere, they have been unable to image the crustal thickness of the region

to a high degree of certainty. Crustal thickness estimates from gravimetric and satellite data provide some insight, estimates vary widely from ~42-65 km [*Block et al.*, 2009; *von Frese et al.*, 1999]. Recent receiver function analysis of the GSM found crustal thicknesses in excess of 55 km beneath the central region of the GSM and thicknesses of ~40-45 km in the surrounding regions [*Hansen et al.*, 2009; *Hansen et al.*, 2010]. These crustal thickness estimates are consistent with studies of the region surrounding the Lambert Graben [*Reading*, 2006].

The recent Gamburtsev Antarctic Mountain Seismic Experiment (GAMSEIS), which is part of the Antarctica's Gamburtsev Province (AGAP) IPY project, extends across the GSM and provides us with the opportunity to image the crust and upper mantle structure of the region to a resolution not previously achievable. Surface wave studies are well suited to such a deployment as they are able to take advantage of a relatively sparse network of stations scattered over a large region. In this study we utilize teleseismic Rayleigh waves to image the GSM at periods of 18-182s. This period range allows us to image, in detail, the crust and upper mantle shear-wave velocity structure of the region.

4.2 Data Acquisition

Data were collected by a temporary array of 28 broadband seismographs deployed across the GSM by the United States, Japanese, and Chinese Antarctic programs as part of a joint International Polar Year initiative to study the region (table 4.1). The United States and Japanese stations consisted of either cold rated Guralp 3-T or Nanometrics T-240 broadband sensors coupled with Quanterra Q330 digitial acquisition systems with

GPS timing. The Chinese stations used cold rated Guralp 3-T sensors with Guralp DM24 data loggers. Using a novel station design developed for polar applications, we were able to operate most of the US-deployed stations throughout the polar night [*Johns et al.*, 2006]. Sensors were placed on insulated piers buried slightly below (~1m) the snow surface. Station electronics were located nearby in insulated boxes that also contained the batteries. Summer power was provided by solar panels and in some cases wind generators connected to AGM batteries while winter power was provided by a bank of primary lithium batteries. A heating pad that operated directly from the solar panel provided some internal heating. This station design was capable of consistently maintaining temperatures within the electronics box greater than 20°C above the ambient temperature.

The US and Japanese stations were installed using DeHavilland Twin Otter aircraft equipped with skis. Chinese stations were installed by overland traverse along the route from Zhongshan station on the coast to Dome A. The US deployment consisted of a pilot year (12/2007- 12/2008) of ten stations (figure 4.1) and a second year (12/2008- 12/2009) of 24. Two Japanese operated stations near Dome Fuji were installed in late 2008 and the two Chinese stations were operated during the 2007-2008 and 2008-2009 austral summers.

4.3 Methods

4.3.1 Data Processing

We utilize fundamental mode Rayleigh wave data generated by teleseismic earthquakes at epicentral distances of 30-150° and depths of less than 100 km. For the

two years of the deployment, we collect seismograms for 514 earthquakes that meet initial selection requirements. For earthquakes with epicentral distances of between 30° and 60°, we set a minimum surface wave magnitude (M_S) of 4.5. For events with epicentral distance greater than 60° we set the minimum M_S at 5.5. We apply this dual selection criterion to take advantage of the relatively small earthquakes that occur at smaller epicentral distances along the circum-Antarctic ridge system. After removing the instrument response for all data, we visually analyze the vertical component of the seismogram to select for high signal-noise-ratio, lack of data glitches or interfering phases, and good overall quality.

Earthquakes that pass the initial quality control selection (figure 4.2) are windowed in the time domain at twenty-five periods between 18 and 182 s around the fundamental mode Rayleigh wave. The filters are composed of two-pass four-corner Butterworth bandpass filters. Filter corner frequencies are set to ±10% of the center frequency. We visually select time windows around the fundamental mode Rayleigh wave arrival and eliminate waveforms with signs of significant beating, low signal-to-noise ratio, or interfering phases that may have been missed in the initial quality control phase. We reject any earthquake/frequency band combination that has good data from less than seven stations. Below this level, the uncertainty in the wavefront parameters for the two plane wave inversion is too high to be considered reliable [*Yang and Forsyth*, 2006a]. The number of waveforms and events for each period are summarized in figure 4.3.

4.3.2 Phase Velocity Inversion

Phase velocity inversion is done using the two plane wave method [*Forsyth and Li*, 2005]. This method uses the phase and amplitude information from each station to model the incoming wavefield as the interference of two plane waves. The method is better able to account for off great-circle path effects, scattering, and multipathing caused by velocity heterogeneity between the source and the study area when compared to traditional surface wave methods [*Forsyth and Li*, 2005; *Li et al.*, 2003]. The two-plane wave method solves for the phase, amplitude, and propagation direction of two incoming wavefronts for each observed event. This information is used to invert for the average phase velocity structure (1-D) and the phase velocity at each node (2-D). Additionally, the method is able to solve for azimuthal anisotropy terms for specific regions.

For inversions allowing for two-dimensional variations in phase velocity, we incorporate the use of finite-frequency sensitivity kernels [*Yang and Forsyth*, 2006a] using the Born approximation [*Zhou et al.*, 2004]. The use of finite frequency kernels improves the discrimination and location of off-great circle energy in the inversion scheme. The use of the two-plane wave method along with the application of finite frequency kernels has been successfully applied during previous regional studies in a variety of tectonic settings [*Pyle et al.*, 2010; *Weeraratne et al.*, 2007; *Yang and Forsyth*, 2006a; b; *Yang and Ritzwoller*, 2008].

Our inversion region is comprised of 486 nodes with a primary central region having a grid spacing of 80 km and an outer region of nodes having a spacing of 160 km. This outer region is necessary to absorb some of the effects of misfit to the two plane wave approximation, primarily due to wavefield scattering outside of the study region. We transform the imaged region into a local reference frame to avoid the problem of

solving for anisotropy directions near the pole. This transformation defines the northing direction as 107.5°E longitude with the origin at the South Pole (figure 4.1). This coordinate rotation simplifies plotting phase and shear velocity maps in the study region and in locating equally spaced grid nodes necessary for inversion.

The inversion scheme solves for the phase velocity continuously across the study region. A 2-D Gaussian weighted interpolation is then used to determine the phase velocity at the nodes. The smoothing length of the Gaussian interpolation represents a compromise between resolution and variance. A greater smoothing length reduces variance at the cost of resolution. To test this tradeoff, we apply a variety of smoothing lengths between 60 and 300 km at 20 km increments. We find that a smoothing length of 100 km provides the best resolution in the period range of 18-58s. Using this smoothing length provides good resolution on the structure of the crust and uppermost mantle, providing us with the most information about variations in crustal thickness across the study region. A greater smoothing length would provide better variance reduction, particularly at longer periods where our dataset is sparser, but since the 2-D phase velocities would be unlikely to deviate strongly from the 1-D starting model, we choose to focus our efforts on imaging the shallow structure at high resolution. An *a priori* variance estimate of 0.2 is applied to the inversion and all periods are inverted for separately.

The two-plane wave inversion includes a station correction term. This term is an amplitude factor designed to account for site effects and discrepancies in instrument response. We find that the station correction term for the majority of the stations is approximately one. This implies that the amplitudes at the stations are being modeled

well by the inversion, and that amplitude anomalies caused by errors in the instrument response are negligible. Several stations near the edge of the array and which did not operate for the entire deployment time. (e.g. EGLE, GM07) have station corrections that deviate strongly from 1, yet generally show similar waveform amplitudes to the rest of the stations. To test the necessity of applying the station correction term for these stations, we perform a separate inversion using only events for which these stations have waveforms. We find a significant reduction in the station correction term for these sites under these circumstances and hypothesize that the large observed station correction is due to the greater distance of these stations from the interior of the array and their absence from many of the events analysed. The distance and lack of data. causes greater difficulty in fitting waveforms from these stations compared to the more centrally located stations. Based on these observations, we choose not to apply the calculated station corrections in our final phase velocity inversions as they arbitrarily down-weight data that provides important constraints on structure outside the central region of the array.

4.3.3 Shear Velocity Inversion

4.3.3.1 Linear Inversion

The shear wave velocity inversion takes a two-step approach similar to that outlined by [*Ritzwoller et al.*, 2001]. We first extract a 1-D phase velocity curve at each node and invert for the shear velocity in a linear least-squares sense using the method of [*Herrmann and Ammon*, 2004]. To investigate the model space around the resulting inverse model we conduct Monte Carlo modeling of the region around the initial model.

These 1-D models are then compiled and smoothed using the same 2-D Gaussian smoothing operator applied to the phase velocity maps.

An important constraint on the inversion of shallow shear velocity structure is the thickness of the ice layer. We use the ice thickness values of BEDMAP [*Lythe et al.*, 2001]. Crustal thickness estimates and average crustal velocities are based on S-wave receiver functions [*Hansen et al.*, 2010] supplemented with data from surrounding regions [*Hansen et al.*, 2009; *Reading*, 2006; *Studinger et al.*, 2003]. We interpolate these thickness estimates at the same length scale as the 2-D Gaussian smoothing used in the phase velocity inversions in order to produce a smooth 2-D crustal thickness map. We divide the crust into three layers a thin upper crust, a thicker mid-crust, and a lower crust. The upper 100 km of the mantle is divided into 10 km thick layers. We divide the next 80 km into 20 km thick layers and the remainder of the upper mantle at 40 km. We are most interested in crustal and uppermost (<250 km) mantle structure. However, we allow for some changes in the velocity model to depths of 400 km to limit smearing of deeper structure into our shallow imaging. We use the upper mantle structure of AK135 [*Kennett et al.*, 1995] as a starting model, and layer thicknesses are fixed in the inversion. Additionally, we fix V_P/V_S ratios at values set out in *Hansen et al* [2010] for the region.

4.3.3.2 Monte Carlo Modeling

One pitfall of inverting phase velocity data for shear velocity structure is the tradeoff between crustal thickness and the velocity structure of the lowermost crust and uppermost mantle. In order to better constrain these uncertainties, we conduct a Markov-chain Monte Carlo simulation of the model space surrounding the 1-D result. Monte

Carlo modeling performs a random walk around the initial model and generates a number of acceptable shear velocity models that produce phase velocity curves that fit the data within an acceptable uncertainty window. The Markov-chain approach uses the most recent acceptable model as the starting model for the next search sequence. These methods have become increasingly common as a means to parameterize uncertainties in shear velocity inversion [*Sambridge and Mosegaard*, 2002]. We parameterize the crust in the same way as in the linear inversion. We allow the crustal velocity structure to vary by ±5% and to include low velocity layers, though the ice layer remains unaffected. Layer thicknesses are fixed as in the linear inversion with the exception of the lowermost crust. Here the layer thickness is allowed to change by ±5 km to allow for uncertainties in the Moho depth estimated from receiver function analysis and the extrapolation of these values to regions of no station coverage. The shear velocity of the upper 200 km of the mantle is allowed to change by up to 7% and depths of 200 - 280 km by 3%. We seek to search the model space around the inverse solution while minimizing complexity of the model in the mantle. To this end, we attempt to minimize the equation:

$$C = \chi^2_{red} \times \sqrt{ISE} \quad (1)$$

$$\chi^2_{red} = \frac{1}{N}\sum_{i=1}^{n}\frac{(d_i^{obs} - d_i^{pred})^2}{(\sigma_i^{obs})^2} \quad (2), \quad ISE = \sum_{i=1}^{m}\left(\frac{\partial^2 V}{\partial z^2}_{inverse} - \frac{\partial^2 V}{\partial z^2}_{model}\right)^2 \quad (3)$$

where C is the cost function, χ^2 is the reduced chi-square misfit of the velocity model to the phase velocity data, *N* is the number of periods, *d* is the observed and predicted phase velocity, σ is the standard deviation of the observed phase velocities, and ISE is the an estimate of model roughness relative to the initial inverse model. This parameterization minimizes misfit to the observed dispersion curve while also limiting complexity in the

resulting velocity model. To further limit models to those that are geologically reasonable, we limit velocity changes between adjacent layers in the mantle to be twice the maximum ΔV of the inverse model. If a velocity model falls within the corridor of acceptable misfit ($5 \times C_{inverse}$), we include it in the probability weighted mean model. We define the probability of a model occurring as $p = ke^{\frac{-C}{2}}$ where k is a normalization constant. This probability weighted approach is similar to that applied by other researchers [*Deschamps et al.*, 2008; *Peter et al.*, 2008]. In order to limit the effect of varying V_P or density on the models, we fix the V_P/V_S ratio for the crust and upper mantle to average values set out in [*Hansen et al.*, 2010] for each model and hold density constant.

Often, the mean model is similar to the starting model, though there can be a significant difference between the mean model and the model with minimum cost (figure 4.8). The minimum cost model fits the observed phase velocities best, but it suffers from being irreproducible between multiple runs of the simulation and a higher degree of roughness between layers. The mean model often 'smears' seismic structure vertically, limiting interpretations of depth dependent seismic velocities. Therefore, we prefer the results of the linear inverse models and use the standard deviation of acceptable models generated during the Monte Carlo simulation as a proxy of model uncertainty for interpretation purposes.

4.4 Results

4.4.1 Phase velocities

4.4.1.1 Uniform Phase velocities

An average 1-D phase velocity curve is presented in figure 4.5. Overall, our results differ greatly from the dispersion curve predicted by the reference model AK135 [*Kennett et al.*, 1995]. The phase velocities are significantly (~ 1.8%) slower at 18s and faster than the global model at periods of 48-124s within the 2σ error bounds of the inversion. An important observation is that 1-D dispersion curves for different regions are not significantly different from either each other or the average model. This is a consistent feature even when considering a three-region inversion where the regions are defined by slow velocity anomalies at intermediate periods in the 2-D phase velocity maps [*Heeszel et al.*, 2010].

4.4.1.2 Laterally Varying Phase Velocities

We use the average dispersion curves for each sub-region as a starting model for 2-D inversions that solve for laterally varying phase velocities at each node. The inversion incorporates finite frequency kernels and includes terms for uniform anisotropy. Resulting phase velocity maps are created by applying a 2-D Gaussian averaging function to interpolate between nodes. Estimates of *a posteriori* standard error are made by applying the same smoothing function to the model covariance matrix. These error maps are a useful tool in estimating the resolution of the phase velocity maps at a given location. For comparison, we also ran an inversion with a uniform starting velocity based on the average dispersion curve for the entire region. Major observed features in the resulting phase velocity maps are similar. Maps presented in figure 4.6 are masked to highlight areas of good resolution.

Phase velocities across the region are relatively homogeneous at 20 seconds period with slower velocities underlying the Vostok Highlands and faster velocities extending from near AGO1 towards the South Pole. In the period range of 25-40 seconds, fast phase velocities dominate in the northwest and southeast of the study region (in the local reference frame). The fast phase velocities in the northwest reach a maximum perturbation of 5% at 30 seconds, and correlate well with the inland extension of the Lambert Rift System. Slow phase velocities dominate the central region of the Gamburtsev Mountains. This anomaly extends generally from the northeast to the southwest, is centered beneath the GSM, and is present across a number of periods, only approaching the average phase velocity at 84 seconds. In general the anomalies in the 25-40 s period range probably delineate variations in crustal thickness, with high velocities showing thin crust in the Lambert Graben area and low velocities showing thick crust beneath the GSM. At longer periods, the amplitude of phase velocity anomalies decreases along with resolution. However, phase velocity variation of ±2% are resolvable throughout the period range of study.

4.4.1.3 Azimuthal Anisotropy

Our inversion scheme allows for the inclusion of an azimuthal anisotropy term. We include inversions for both a single region and for multiple regions in our analysis. The inversion for a single region (figure 4.7a,b) is sub parallel to shear-wave splitting results for the region [*Hernandez et al.*, 2010]. Inversions for multiple regions (figure 4.7c,d) are more complex. Region one (blue nodes in figure 4.4) is largely sub parallel to the shear-wave splitting results in the same region, while region two is significantly

noisier making interpretation difficult. The greater scatter in azimuth and amplitude of the second region is likely due to our incorporating multiple small regions of varying anisotropy into a single region. However, without *a priori* knowledge of the geologic structure in the region it would be arbitrary to place boundaries that minimize scatter in the anisotropy results. Overall, we observe about 1% anisotropy at periods below 100 s. At longer periods, the amplitude of the anisotropy measurements increases greatly along with the uncertainty. This increase in uncertainty can be linked to the rapid decrease in raypath coverage at periods beyond 100s.

4.4.2 Shear Velocities

4.4.2.1 1-D Shear Velocity

Shear velocity results for the study region are summarized in figure 4.8. Crustal velocities are 3.6-3.9 km/s. The model average crustal thickness for the region based on the regional phase velocity curve is 48 km. This is fit well by our phase velocity curve fitting analysis (figure 4.9). The upper mantle structure is comparable to other cratonic regions, but the overall crustal thickness is greater than for many regions. The mantle structure, however, is consistent with other regions around the world that date to the Precambrian. It most closely resembles an aggregate of cratonic regions. The upper mantle is similar to a number of models, particularly including the West African craton and the Siberian shield [*Shapiro and Ritzwoller*, 2002] (figure 4.9, 4.14f).

4.4.2.2 3-D Shear Velocities

By inverting for 1-D shear velocity structure at each node and applying the same Gaussian averaging scheme as in the phase velocity inversions, we construct quasi 3-D shear velocity models of the study region. This model is then refined by applying Monte Carlo modeling. This analysis aids in constraining crustal thickness across the region (figure 4.12). The 30 km depth velocity map (figure 4.10a) shows an average lower crust shear wave velocity of ~3.9 km/s throughout the majority of the study region with slower velocities in the northeast, northwest and southwest of the region. Small regions of faster and slower velocities are present within the GSM proper. The 50 km depth map (figure 4.10b) shows the crustal root beneath the GSM, with the uppermost mantle velocity of 4.1- 4.75 in the surrounding regions. The fastest region of uppermost mantle velocities occurs directly to the northwest of the GSM between the inland extension of the Lambert Rift and the region of thickest crust (figure 4.10b, c). We observe this region of relatively faster shear wave velocities to depths in excess of 100 km. Slower shear wave velocities are present beneath the GSM throughout the mantle to depths of ~150 km. At depths greater than 150 km the velocities are largely homogeneous with the exception of the extreme western region of the study region extending from the Lambert Rift south. Shear velocities decrease to ~4.6 km/s at depths greater than 250 km indicating that the seismic lithosphere is probably limited to shallower depths, a result consistent with globally based studies of the region [*Danesi and Morelli*, 2001; *Ritzwoller et al.*, 2001].

Cross-sections of the region are informative in understanding the lateral extent of depth anomalies in the study region. The seismically fast region of the upper mantle extending from approximately 125-250km in depth is non-contiguous in the study region.

A significant gap occurs between -1400 km and -1100 km in the easting (x) direction (figure 4.11a). This region correlates roughly to the inland extension of the Lambert Rift. This velocity anomaly is intriguing as it suggests that the Lambert Rift caused small changes in the structure of the mantle beneath a large section of the Antarctic continent and may have extended further inland than is indicated by topography alone. We note however that this velocity anomaly does not extend to the region beneath the GSM proper, and is unlikely to have significantly affected the mantle in this region. The north-south cross section (figure 4.11b) extends across the center of the GSM passing through station N173. We observe little variation in mantle structure across the GSM.

4.5. Discussion

4.5.1 Comparison with Previous Studies

Because this study represents the first regional seismic analysis of the Gamburtsev Subglacial Mountains, it is informative to compare our results with results derived from global datasets. Two relatively recent surface wave studies have focused on the Antarctic continent. One, [*Ritzwoller et al.*, 2001] utilized fundamental mode phase and group velocity measurements of both Rayleigh and Love waves to perform anisotropic shear velocity tomography of the entire Antarctic continent. These researchers found a thickened crust beneath the GSM and a lithospheric root extending to nearly 250 km depth. This study however lacked the resolution (maximum resolution in the GSM region was 500-600 km at 50s and >800 km at 150s) to image the sharp structural boundaries between the GSM and the Lambert rift system seen in results presented in this paper. A more recent study [*Danesi and Morelli*, 2000; 2001; *Morelli*

and Danesi, 2004] utilized a more limited dataset and imaged similar lithospheric thicknesses in the GSM, though it too lacked the resolution to image sharp structural boundaries within East Antarctica. Overall, our results compare will with both studies. We too observe thickened lithosphere beneath the GSM, though we image significantly more variation in crustal thickness than either previous study. Additionally, we clearly image the extension of the Lambert Rift System into the study region.

Studies of the region based on satellite gravity data [*Block et al.*, 2009] and those based on receiver functions [*Hansen et al.*, 2010] have significant discrepancies in crustal thickness estimates. Our results are offset by a constant value of ~6 km throughout the study region. This may represent a lack of lateral resolution within the study area in the gravity models. An additional possibility is that a thicker, denser crust and a depleted, buoyant lithospheric root that can compensate additional crustal thickness. This interpretation is supported by our crustal thickness estimates from the Monte Carlo modeling, which are in close agreement with the receiver function results for the region (figure 4.12) and show little change from the starting model (figure 4.13). Due to the parameterization of the lower crust as 1/2 the total crustal thickness, we are unable to resolve thin layers of partially eclogitized material at the base of the crust.

4.5.2 Lithospheric Age Constraints

In hopes of better constraining the age of the Gamburtsev Mountains and surrounding regions, we compare our average phase velocity curve to those of differing ages using a global phase velocity structure [*Visser et al.*, 2008] and a simplified crustal age map [*Mooney et al.*, 1998]. We compare our results with the median curve for

different tectonic ages in an attempt to account for differing tectonic histories. By coupling phase velocity curves with crustal age estimates, we can place rough bounds on the age of the GSM lithosphere. While this analysis does not place absolute age constraints on the formation of the GSM, it does aid in providing an upper and lower bound on that age and informs attempts at interpreting their evolution. Our results are summarized in figure 4.14. At periods between 50 and 175 seconds our results correlate best with regions where mapped crustal ages (and presumably mantle ages) are Early – Middle Proterozoic (2500 – 1700Ma) and the 'undefined' Proterozoic which corresponds with regions of Proterozoic age crust that have significant Phanerozoic sedimentary cover [*Artemieva*, 2006; *Artemieva and Mooney*, 2001; *Mooney et al.*, 1998; *Poupinet and Shapiro*, 2009]. It is worth noting that regions of young mountain building such as the Himalayas or Andes are absent from regions of acceptable fit in our analysis (figure 4.14f). This suggests that the processes responsible for the creation of the GSM lithosphere are not recently active, but rather that the GSM lithosphere is an old feature. From this analysis we can infer that the lithosphere of the GSM dates to the Precambrian, probably the Early-Middle Proterozoic (~2500 – 2000Ma) and age range largely consistent with recent tectonic reconstructions of the region [*Boger*, 2011; *Veevers and Saeed*, 2008]. We cannot rule out an Archean (>2500Ma) origin for the GSM lithosphere as the fit to the median global curve is nearly as good as that for the Early-Middle Proterozoic. This analysis encompasses a large region of East Antarctica, and it is possible that there are multiple, small cratonic blocks within it. Additionally, regions such as the Lambert Rift System have undergone Phanerozoic extension, which likely

modified the upper mantle. The region as a whole however, is consistent with an Early-Middle Proterozoic origin.

4.5.3 Preservation of Topography

Our results show thickened crust underlying the GSM and a seismically fast upper mantle within the study region that is consistent with an Early-Middle Proterozoic origin. Coupled with high elevations [*Bo et al.*, 2009; *Lythe et al.*, 2001; *Wolovick et al.*, 2009] and geochronology that suggests an early Paleozoic origin [*van de Flierdt et al.*, 2008; *Veevers et al.*, 2008a], an important question about the long-term stability of the GSM is how significant topography and crustal thicknesses can be preserved over such a long time period. Climate models indicate that the GSM have been ice covered for at least the past 34Ma [*DeConto and Pollard*, 2003a; b]. In order to preserve topography in excess of 2 km and crustal thicknesses in excess of 55 km in the central region of the GSM multiple processes must be active. Surface processes must act to limit erosion with the GSM and processes within the lowermost crust and upper mantle must limit degradation of the crustal root in order to retain crustal buoyancy.

Crustal thickness estimates from receiver function analysis indicate that erosion within the GSM must be extremely low if the mountains are of any significant age. Recent ground based radar work has found large, deeply incised valleys in the central GSM consistent with glacial steepening of existing stream valleys [*Bo et al.*, 2009]. Long term erosion rates have been estimated to be as low as 0.01-0.02 km/Ma for the last 250Ma [*Cox et al.*, 2010]. This would correspond to removing 2.5-5 km of crustal material from the GSM over this period. Using some simple assumptions about the age

and crustal thickness of the GSM we can extrapolate these results further into the past. The GSM region has a maximum crustal thickness of ~57 km [*Hansen et al.*, 2010]. If we assume an original crustal thickness of 80 km, a time and thickness averaged crustal density of 2800kg/m^3 and an end to mountain building processes at 480Ma based on detrital zircons [*van de Flierdt et al.*, 2008] then we can infer a maximum average erosion rate of 0.05 km/Ma. This value is at least double that of the last 250Ma and more than 20 times that determined to be appropriate for the last 118Ma for sediment thicknesses in Prydz Bay [*Jamieson et al.*, 2005].

In order to preserve significant relief over hundreds of millions of years, processes other than low erosion rates must be active. The buoyancy force of crustal roots declines over geologic time [*Fischer*, 2002, and references therein] and they can be removed entirely through the processes of post-orogenic collapse and lithospheric delamination [*Fischer*, 2002; *Kay and Kay*, 1993; *Leech*, 2001]. In order to maintain a buoyant crustal root over the timescale suggested by *van de Flierdt et al.* [2008], the process of post orogenic collapse, whereby the crustal root undergoes metamorphism and structural weakening must be limited. *Leech* [2002], proposed that this process could occur under 'dry' conditions when insufficient fluid is present to complete the eclogitization of the lower crust. Preservation of thickened crust has been observed in the Tran-Hudson orogeny, an Early Proterozoic suture zone [*Chulick and Mooney*, 2002; *French et al.*, 2009; *Zelt and Ellis*, 1999], and Svecofennia, an Early Proterozoic collisional belt in the Fennoscandian Shield [*Bruneton et al.*, 2004; *Kozlovskaya et al.*, 2008]. These regions, however, exhibit little of the topographic relief observed in the GSM [*Fischer*, 2002; *French et al.*, 2009]. This suggests that maintaining a buoyant

crustal root over long periods is difficult and topographic relief within the GSM is unlikely to be solely related to crustal thickening and uplift during the Neoproterozoic – early Paleozoic. An alternative and perhaps more likely hypothesis is a hybrid model in which initial crustal thickening occurred intermittently during the assembly of cratonic blocks throughout the Proterozoic culminating in the formation of Gondwana. Uplift along extant faults was reactivated during the mid-Carboniferous-Permian during the assembly of Pangea. Numerical modeling of crustal roots has shown high viscosity in the lithosphere can aid in the preservation of crustal roots over long periods [*Koyi et al.*, 1999; *Marotta et al.*, 1998; *Schott and Schmeling*, 1998]. By combining low erosion rates, crust that has undergone multiple instances of thickening, and late reactivation of existing faults it is possible to produce a modern mountain range such as the GSM.

4.6 Conclusions

The mysteries of the Gamburtsev Subglacial Mountains are many and varied. Due to a scarcity of data, questions about their age, provenance, and mode of structural support have plagued Antarctic researchers since their discovery in the 1950s. Through an analysis of teleseismic surface waves recorded at an array of temporary broadband seismometers, we have imaged the shear velocity structure of the region at an unprecedented scale. We observe fast seismic velocity extending to depths of greater than 200 km indicating a thickened cratonic lithosphere that is consistent in age with the Early-Middle Proterozoic and a crust that is greater than 55 km thick in the central region under laying Dome A. We suggest that the Gamburtsev Mountains formed through multiple processes operating through geologic time form their initial development as an

Early Proterozoic collisional zone, continued periods of uplift and crustal thickening during the Proterozoic and extending into the early Paleozoic as the assembly of Gondwana occurred followed by reactivation of extant faults during the Carboniferous-Permian formation of Pangea. Long term, cold-based glaciation following the most recent uplift event combined with a thick high viscosity lithospheric root that further limits delamination processes has limited erosion of the GSM from the top and delamination/ductile rebound from the base.

4.7 Acknowledgements

The authors would like to acknowledge the hard work and support of the field teams responsible for collecting these data. We would also like to thank staff and polar specialists at IRIS/PASSCAL who provided both instrumentation and field support during the operation of this array. We thank the pilots and staff of Kenn Borek Air and the New York Air Guard for flight support and the staff at AGAP-S camp, South Pole Station, McMurdo Station, and Raytheon Polar Services for logistical support. This project was supported by the United States NSF grant ANT-0537597, the Japanese Antarctic Program, and China National Science Foundation grant NSFC-40874021. The majority of figures presented in this paper were produced using GMT [*Wessel and Smith*, 1998].

4.8 References

Artemieva, I. M. (2006), Global 1°x1° thermal model TC1 for the continental lithosphere: Implications for lithosphere secular evolution, *Tectonophysics*, *416*, 245-277.

Artemieva, I. M., and W. D. Mooney (2001), Thermal thickness and evolution of Precambrian lithosphere: a global study, *J. Geophys. Res*, *106*(B8), 16387-16414.

Barklage, M., D. A. Wiens, A. Nyblade, and S. Anandakrishnan (2009), Upper mantle seismic anisotropy of South Victoria Land and the Ross Sea coast, Antarctica from SKS and SKKS splitting analysis, *Geophys. J. Int.*, *178*, 729-741.

Bassin, C., G. Laske, and G. Masters (2000), The current limits of resolution for surface wave tomography in North America, *Eos. Trans. AGU*, *81*(48), Fall Meet. Suppl., Abstract S12A-03.

Bell, R. E., et al. (2009), The East Antarctic Ice Sheet and the Gamburtsev Subglacial Mountains, *Eos. Trans. AGU*, *90*(52), Fall Meet. Suppl., Abstract G52B-03.

Block, A. E., R. E. Bell, and M. Studinger (2009), Antarctic crustal thickness from satellite gravity: Implications for the Transantarctic and Gamburtsev Subglacial Mountains, *Earth Planet. Sci. Lett.*, *288*, 194-203.

Bo, S., M. J. Seigert, S. M. Mudd, D. Sugden, S. Fujita, C. Xianbin, J. Yunyun, T. Xueyuan, and L. Yuansheng (2009), The Gamburtsev mountains and the origin and early evolution of the Antarctic Ice Sheet, *Nature*, *459*, 690-693.

Boger, S. D. (2011), Antarctica - Before and after Gondwana, *Precam. Res.*, *19*, 335-371.

Bruneton, M., et al. (2004), Complex lithospheric structure under the central Baltic Shield from surface wave tomography, *J. Geophys. Res*, *109*.

Chulick, G. S., and W. D. Mooney (2002), Seismic structure of the crust and uppermost mantle of North America and adjacent oceanic basins: A synthesis, *Bull. Seism. Soc. Am.*, *92*(6), 2478-2492.

Cox, S. E., S. N. Thomson, P. W. Reiners, S. R. Hemming, and T. van de Flierdt (2010), Extremely low long-term erosion rates around the Gamburtsev Mountains in interior East Antarctica, *Geophys. Res. Lett.*, *37*.

Danesi, S., and A. Morelli (2000), Group velocity of Rayleigh waves in the Antarctic region, *Phys. Earth Planet. Int.*, *122*, 55-66.

Danesi, S., and A. Morelli (2001), Structure of the upper mantle under the Antarctic Plate from surface wave tomography, *Geophys. Res. Lett.*, *28*(23), 4395-4398.

DeConto, R. M., and D. Pollard (2003a), A coupled climate-ice sheet modeling approach to Early Cenozoic history of the Antarctic ice sheet, *Palaeogeography, Palaeoclimatology, Palaeoecology*, *198*, 39-52.

DeConto, R. M., and D. Pollard (2003b), Rapid Cenozoic glaciation of Antarctica induced by declining atmospheric CO_2, *Nature*, *421*, 245-249.

Deschamps, F., S. Lebedev, T. Meier, and J. Trampert (2008), Stratified seismic anisotropy reveals past and present deformation beneath the East-central United States, *Earth Planet. Sci. Lett.*, *274*, 489-498.

Ferraccioli, F., T. H. Jordan, C. Finn, R. E. Bell, D. Damaske, D. A. Braaten, and M. Studinger (2010), New aerogeophysical insights into the Gamburtsev Sublacial Mountains enigma, *Eos. Trans. AGU*, *91*(52), Fall Meet. Suppl., Abstract T21D-2192.

Fischer, K. M. (2002), Waning Bouyancy in the crustal roots of old mountains, *Nature*, *417*, 933-936.

Fitzsimons, I. C. W. (2000), Grenville-age basement provinces in East Antarctica: Evidence for three separate collisional orogens, *Geology*, *28*(10), 879-882.

Fitzsimons, I. C. W. (2003), Proterozoic basement provinces in southern and southwestern Australia, and their correlation with Antarctica, in *Proterozoic East Gondwana: Supercontinent Assembly and Breakup*, edited by M. Yoshida, B. F. Windley and S. Dasgupta, pp. 93-130, Geological Society, London, Special Publication, London.

Forsyth, D. W., and A. Li (2005), Array analysis of two-dimensional variations in surface wave phase velocity and azimuthal anisotropy in the presence of multipathing interference, in *Seismic Earth: Array Analysis of Broadband Seismograms*, edited by A. Levander and G. Nolet, pp. 81-97, AGU, Washington D.C.

French, S. W., K. M. Fischer, E. M. Syracuse, and M. E. Wysession (2009), Crustal structure beneath the Florida-to-Edmonton broadband seismometer array, *Geophys. Res. Lett.*, *36*.

Hansen, S. E., J. Julia`, A. A. Nyblade, M. L. Pyle, D. A. Wiens, and S. Anandakrishnan (2009), Using S wave receiver functions to estimate crustal structure beneath ice sheets: An application to the Transantarctic Mountains and East Antarctic craton, *Geochem. Geophys. Geosyst.*, *10*(8).

Hansen, S. E., A. A. Nyblade, D. S. Heeszel, D. A. Wiens, P. J. Shore, and M. Kanao (2010), Crustal structure of the Gamburtsev Mountains, East Antarctica, from S-wave receiver functions and Rayleigh wave phase velocities, *Earth Planet. Sci. Lett.*, *300*, 395-401.

Heeszel, D. S., X. Sun, D. A. Wiens, A. Nyblade, M. Kanao, M. An, Y. Zhao, S. Anandakrishnan, and R. C. Aster (2010), Shear velocity structure of the Gamburtsev Mountains, Transantarctic Mountains and East Antarctica from surface wave tomography, IPY Oslo Sci. Conf., Abstract PS1-D.91

Hernandez, S., D. A. Wiens, and A. Nyblade (2010), East Antarctic seismic anisotropy from Shear-wave splitting analysis of AGAP seismograms, *Abstract DI13A-1849 presented at 2010 Fall Meeting, AGU, San Francisco, Calif., 13-17 Dec.*

Herrmann, R. B., and C. J. Ammon (2004), Computer Programs in Seismology: Surface Waves, Reciever Functions and Crustal Structure, edited, St. Louis Univ., St. Louis, MO.

Jamieson, S. S. R., N. R. J. Hulton, D. Sugden, A. J. Payne, and J. Taylor (2005), Cenozoic landscape evolution of the Lambert Basin, East Atarctica: The relative role of rivers and ice sheets, *Global and Planetary Change*, *45*, 35-49.

Johns, B., K. R. Anderson, B. C. Beaudoin, J. Fowler, T. Parker, and S. White (2006), Development of a power and communications system for remote autonomous polarr observations, *Eos. Trans. AGU*, *87*(52), Fall Meet. Suppl., Abstract S41A-1314.

Jordan, T. H., F. Ferraccioli, M. Studinger, R. E. Bell, D. Damaske, S. Elieff, C. Finn, D. A. Braaten, and H. Corr (2009), Investigating the subglacial landscapes and crustal structure of the Gamburtsev Province in East Antarctica with the aid of new airborne gravity data, *Eos. Trans. AGU*, *90*(52), Fall Meet. Suppl., Abstract C43A-0484.

Kay, R. W., and S. M. Kay (1993), Delamination and delamination magmatism, *Tectonophysics*, *219*, 177-189.

Kennett, B. L. N., E. R. Enghdal, and R. Buland (1995), Constraints on seismic velocities in the Earth from travel times, *Geophys. J. Int.*, *122*, 108-124.

Koyi, H. A., A. G. Milnes, H. Schmeling, C. J. Talbot, C. Juhlin, and H. Zeyen (1999), Numerical models of ductile rebound of crustal roots beneath mountain belts, *Geophys. J. Int.*, *139*, 556-562.

Kozlovskaya, E., G. Kosarev, I. Aleshin, O. Riznichenko, and I. Sanina (2008), Structure and composition of the crust and upper mantle of the Archean-Proterozoic

boundary in the Fennoscandian sheild obtained by joint inversion of receiver function and surface wave phase velocity of recording of the SVEKALAPKO array, *Geophys. J. Int.*, *175*, 135-152.

Leech, M. L. (2001), Arrested orogenic development: eclogitization, delamination, and tectonic collapse, *Earth Planet. Sci. Lett.*, *185*, 149-159.

Li, A., D. W. Forsyth, and K. M. Fischer (2003), Shear velocity structure and azimuthal anisotropy beneath eastern North America from Rayleigh wave inversion, *J. Geophys. Res*, *108*(B8).

Lisker, F., R. Brown, and D. Fabel (2003), Denudational and thermal history along a transect across the Lambert Graben, northern Prince Charles Mountains, Antarctica, derived from apatite fission track thermochronology, *Tectonics*, *22*(5).

Liu, X., Y. Zhao, and X. Liu (2002), Geological aspects of the Grove Mountains, East Antarctica, *Bull. R. Soc. NZ*, *35*, 161-166.

Liu, X., B. Jahn, Y. Zhao, M. Li, M. Li, and X. Liu (2006), Late Pan-African granitoids from the Grove Mountains, East Antarctica: Age, origin ant tectonic implications, *Precam. Res.*, *145*, 131-154.

Lythe, M. B., D. G. Vaughan, and t. B. Consortium (2001), BEDMAP: A new ice thickness and subglacial topographic model of Antarctica, *J. Geophys. Res*, *106*(B6), 11335-11351.

Marotta, A. M., M. Fernandez, and R. Sabadini (1998), mantle unrooting in collisional settings, *Tectonophysics*, *296*, 31-46.

Mooney, W. D., G. Laske, and T. G. Masters (1998), Crust 5.1: A global crustal model at 5 x 5, *J. Geophys. Res*, *103*(B1), 727-747.

Morelli, A., and S. Danesi (2004), Seismological imaging of the Antarctic continental lithosphere: a review, *Global and Planetary Change*, *42*, 155-165.

Peter, D., L. Boschi, F. Deschamps, B. Fry, G. Ekstrom, and D. Giardini (2008), A new finite-frequency shear-velocity model of the European-Mediterranean region, *Geophys. Res. Lett.*, *35*.

Phillips, G., and A. L. Läufer (2009), Brittle deformation relating to the Carboniferous-Cretaceous evolution of the Lambert Graben, East Antarctica: A precursor for Cenozoic relief development in an intraplate and glaciated region, *Tectonophysics*, *471*, 216-224.

Poupinet, G., and N. M. Shapiro (2009), Worldwide distribution of ages of the continental lithosphere derived from a global seismic tomographic model, *Lithos*, *109*, 125-130.

Pyle, M. L., D. A. Wiens, D. S. Weeraratne, P. J. Shore, H. Shiobara, and H. Sugioka (2010), Shear velocity structure of the Mariana mantle wedge from Rayleigh wave phase velocities, *J. Geophys. Res*, *115*, B11304.

Reading, A. M. (2006), The seismic structure of Precambrian and early Palaeozoic terranes in the Lambert Glacier region, East Antarctica, *Earth Planet. Sci. Lett.*, *244*, 44-57.

Ritzwoller, M. H., N. M. Shapiro, A. L. Levshin, and G. M. Leahy (2001), Crustal and upper mantle structure beneath Antarctica and surrounding oceans, *J. Geophys. Res*, *106*(12), 30645-30670.

Roult, G., and D. Rouland (1992), Antarctica I: deep structure investicagions inferred from seismology: a review, *Phys. Earth Planet. Int.*, *84*, 15-32.

Sambridge, M., and K. Mosegaard (2002), Monte Carlo methods in geophysical inverse problems, *Rev. Geophys.*, *40*(3), 1-29.

Schott, B., and H. Schmeling (1998), Delamination and detachment of a lithospheric rot, *Tectonophysics*, *296*, 225-247.

Shapiro, N. M., and M. H. Ritzwoller (2002), Monte-Carlo inversion for a global shear-velocity model of the crust and upper mantle, *Geophys. J. Int.*, *151*, 88-105.

Sleep, N. H. (2006), Mantle plumes from top to bottom, *Earth-Science Reviews*, *77*, 231-271.

Studinger, M., G. D. Karner, R. E. Bell, V. Levin, C. A. Raymond, and A. A. Tikku (2003), Geophysical models for the tectonic framework of the Lake Vostok region, East Antarctica, *Earth Planet. Sci. Lett.*, *216*, 663-677.

Tingey, R. J. (1991), The regional geology of Archaean and Proterozoic rocks in Antarctica, in *The Geology of Antarctica*, edited by R. J. Tingey, pp. 1-73, Oxford University Press, Oxford, UK.

van de Flierdt, T., S. R. Hemming, S. L. Goldstein, G. E. Gehrels, and S. E. Cox (2008), Evidence against a young volcanic origin of the Gamburtsev Subglacial Mountains, Antarctica, *Geophys. Res. Lett.*, *35*.

Veevers, J. J. (1994), Case for the Gamburtsev Subglacial Mountains of East Antarctica originating by mid-Carboniferous shortening of an intracratonic basin, *Geology*, *22*, 593-596.

Veevers, J. J., and A. Saeed (2008), Gamburtsev Subglacial Mountains provenance of Permian-Triassic sandstones in the Prince Charles Mountains and offshore Prydz Bay: Integrated U-Pb and T_{DM} ages and host-rock affinity from detrital zircons, *Gondwana Res.*, *14*, 316-342.

Veevers, J. J., A. Saeed, and P. E. O'Brien (2008a), Provenance of the Gamburtsev Subglacial Mountains from U-Pb and Hf analysis of detrital zircons in Cretaceous to Quaternary sediments in Prydz Bay and beneath the Amery Ice Shelf, *Sed. Geo.*, *211*, 12-32.

Veevers, J. J., A. Saeed, N. Pearson, E. Belousova, and P. D. Kinny (2008b), Zircons and clay from morainal Permian siltstone at Mt. Rymill (73S, 66E), Prince Charles Mountains, Antarctica, reflect the ancestral Gamburtsev Subglacial Mountains - Vostok Subglacial Highlands complex, *Gondwana Res.*, *14*, 343-354.

Visser, K., J. Trampert, and B. L. N. Kennett (2008), Global anisotropic phase velocity maps for higher mode Love and Rayleigh waves, *Geophys. J. Int.*, *172*, 1016-1032.

von Frese, R. R. B., L. Tan, J. W. Kim, and C. R. Bently (1999), Antarctic crustal modeling from the spectral correlation of free-air gravity anomalies with the terrain, *J. Geophys. Res*, *104*(B11), 2522275-2525296.

Weeraratne, D. S., D. W. Forsyth, Y. Yang, and S. C. Webb (2007), Rayleigh wave tomography beneath intraplate volcanic ridges in the South Pacific, *J. Geophys. Res*, *112*.

Wessel, P., and W. H. F. Smith (1998), New, improved version of Generic Mapping Tools released, *Eos. Trans. AGU*, *79*(47).

Wolovick, M., N. Frearson, A. E. Block, R. E. Bell, M. Studinger, F. Ferraccioli, D. A. Braaten, and D. Damaske (2009), Preliminary analysis of the Gamburtsev Subglacial Mountains morphology from AGAP airborne radar data, *Eos. Trans. AGU*, *90*(52), Fall Meet. Suppl., Abstract C43A-0486.

Yang, Y., and D. W. Forsyth (2006a), Regional tomographic inversion of the amplitude and phase of Rayleigh waves with 2-D sensitivity kernels, *Geophys. J. Int.*, *166*, 1148-1160.

Yang, Y., and D. W. Forsyth (2006b), Rayleigh wave phase velocities, small-scale convection, and azimuthal anisotropy beneath southern California, *J. Geophys. Res*, *111*.

Yang, Y., and M. H. Ritzwoller (2008), Teleseismic surface wave tomography in the western U.S. using the Transportable Array component of USArray, *Geophys. Res. Lett.*, *35*.

Zelt, B. C., and R. M. Ellis (1999), Receiver-function studies in the Trans-Hudson Orogen, Saskatchewan, *Can. J. Earth Sci.*, *36*, 585-603.

Zhao, Y., B. Song, Z. Zhang, Y. Fu, T. Chen, Y. Wang, L. Ren, Y. Yao, J. Li, and X. Liu (1995), Early Paleozoic (Pan African) thermal event of the Larsemann Hills and its neighbours, Prydz Bay, East Antarctica, *Sci. Sin.*, *38*, 74-84.

Zhou, Y., F. A. Dahlen, and G. Nolet (2004), Three-dimensional sensitivity kernels for the surface-wave observables, *Geophys. J. Int.*, *158*, 142-168.

Table 4.1. Station names and locations for the GAMSEIS experiment. Chinese stations operated only during the austral summer.

Station Name	Latitude	Longitude	Operating Nation	Operating Years
N124	−82.0745	107.6406	US	12/2007-12/2009
N132	−82.0751	101.9534	US	12/2008-12/2009
N140	−82.0086	96.7692	US	12/2007-12/2009
N148	−81.8625	91.5076	US	12/2008-12/2009
N156	−81.6726	86.5045	US	12/2007-12/2009
N165	−81.4084	81.7604	US	12/2008-12/2009
N173	−81.1122	77.4736	US	12/2007-12/2009
N182	−80.7363	73.1898	US	12/2008-12/2009
N190	−80.3275	69.431	US	12/2008-12/2009
N198	−79.8597	65.9607	US	12/2007-12/2009
N206	−79.3947	62.8556	US	12/2008-12/2009
N215	−78.9045	59.9943	US	12/2008-12/2009
P061	−84.4996	77.2238	US	12/2007-12/2009
P071	−83.6465	77.3347	US	12/2008-12/2009
P080	−82.8054	77.364	US	12/2007-12/2009
P090	−81.9361	77.3142	US	12/2008-12/2009
P116	−79.5669	77.0451	US	12/2008-12/2009
P124	−78.8718	77.657	US	12/2008-12/2009
GM01	−83.9858	104.7291	US	12/2007-12/2009
GM02	−79.4251	97.5815	US	12/2008-12/2009
GM03	−80.2169	85.9439	US	12/2008-12/2009
GM04	−82.9997	61.1124	US	12/2007-12/2009
GM05	−81.1841	51.1588	US	12/2008-12/2009
GM06	−79.3328	44.3148	Japan	12/2008-12/2009
GM07	−77.3136	39.6132	Japan	12/2008-12/2009
AGO1	−83.8596	129.6121	US	12/2007-12/2009
EGLE	-76.4175	77.0297	China	2007/2008 2008/2009
CHNB	-77.1745	76.9762	China	2008/2009

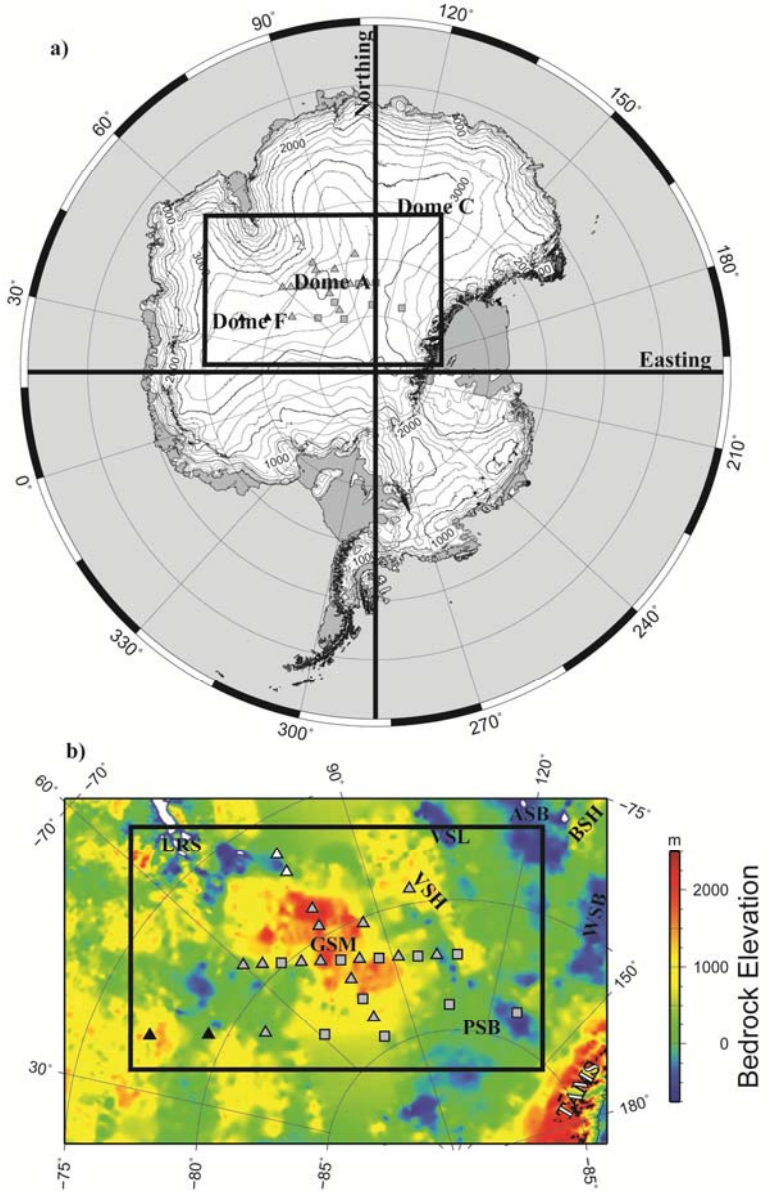

Figure 4.1: a) Topographic Map of Antarctica. Stations in grey operated by the US, squares ran for two years, triangles for one. Stations in black operated by Japan, and those in white by China (table 4.1). Major ice domes in East Antarctica labeled Region plotted in (b) outlined by heavy black line. Northing and Easting directions used in figures 4, 6, and 10 are labeled. b.) Subglacial bedrock topography of Antarctica [*Lythe et al.*, 2001], stations as in (a). GSM – Gamburtsev Subglacial Mountains, VSH – Vostok Subglacial Highlands, LRS – Lambert Rift System, VSL – Vostok Subglacial

Lake, ASB – Aurora Subglacial Basin, BSH – Belgica Subglacial Highlands, PSB – Polar Subglacial Basin, TAMS – Transantarctic Mountains Box denotes region imaged in this study.

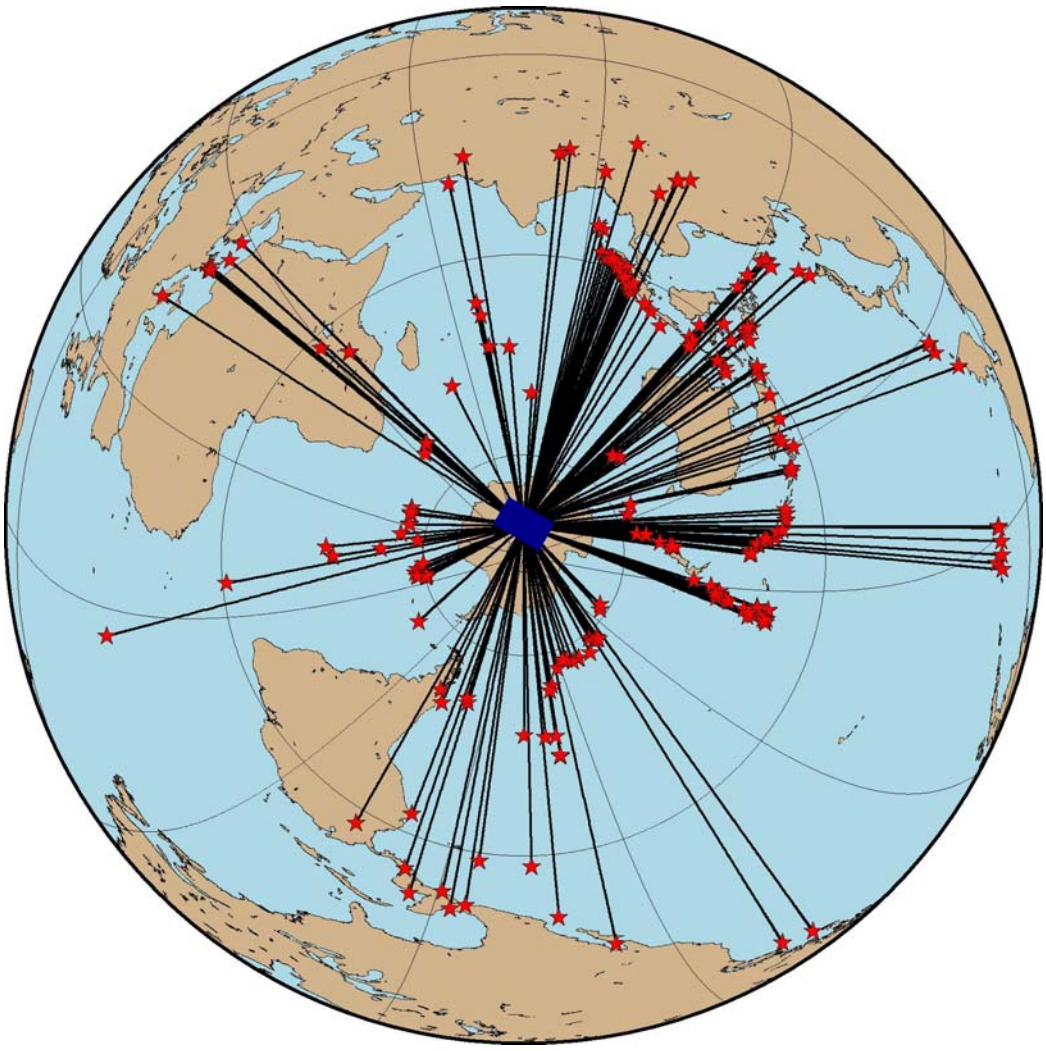

Figure 4.2: Azimuthal equidistant map of earthquakes (red stars) used in this study. Great circle paths to station N173 near the center of the array plotted in black, study region in dark blue.

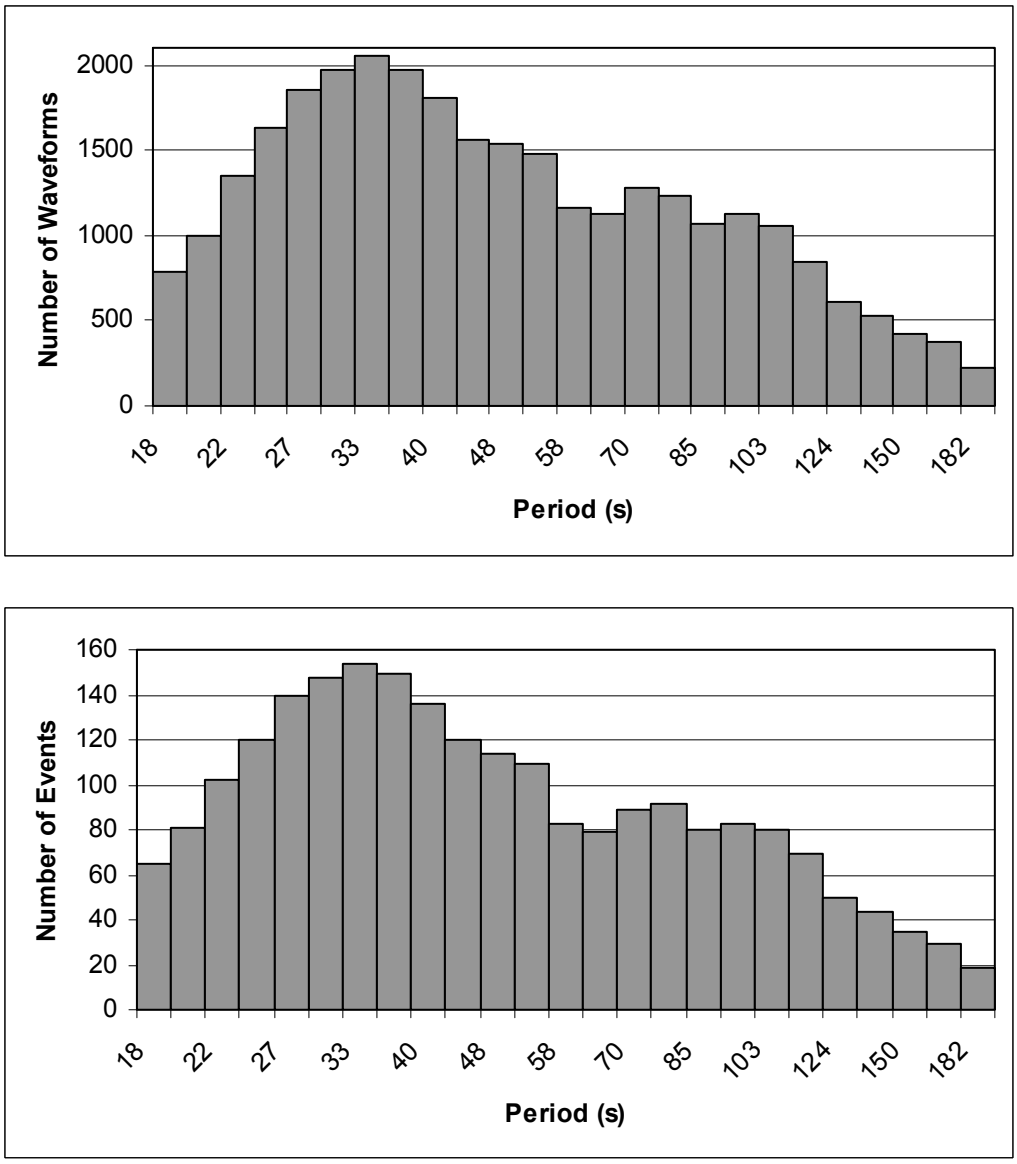

Figure 4.3: Event and period distribution for study. We observe a maximum number of event/station pairs at 33s with a secondary peak at 70s providing us with peak resolution in the lowermost crust and upper mantle.

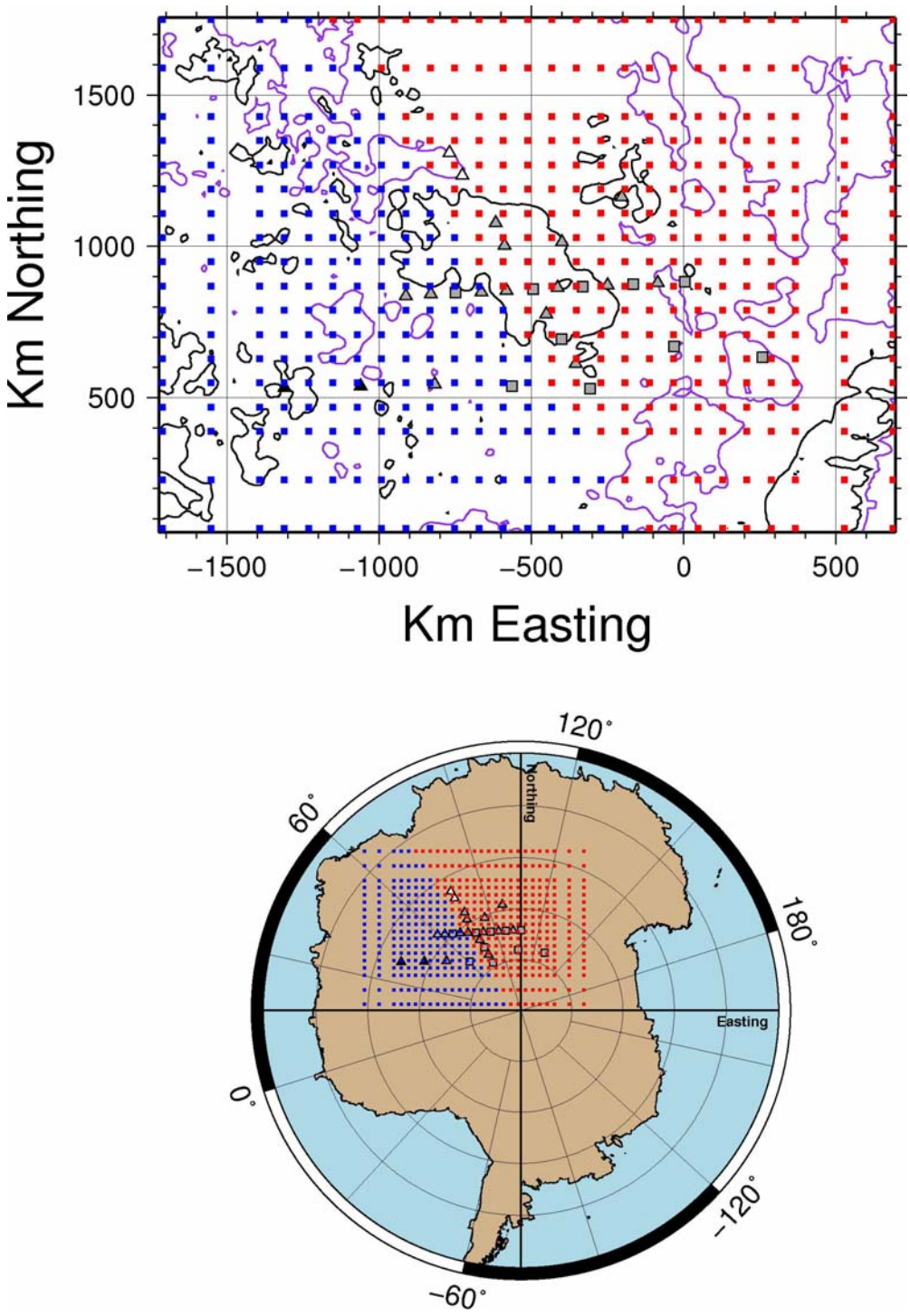

Figure 4.4: Location of nodes used in this study (upper) local geographic distribution of nodes. Black contours: bedrock elevation of 1000m, violet contours: bedrock elevation of 0m. Region 1 (blue) and region 2 (red) used for inversions with multiple regions of

anisotropy. Location of region 1 and region 2 determined by shear-wave splitting measurements of [*Hernandez et al.*, 2010]. Stations as in figure 4.1. Lower: node locations with respect to Antarctic continent, colors are same as in a. X and y-axes defined in km easting or northing respectively with the origin located at the South Pole and the y-axis along 107.5°E longitude.

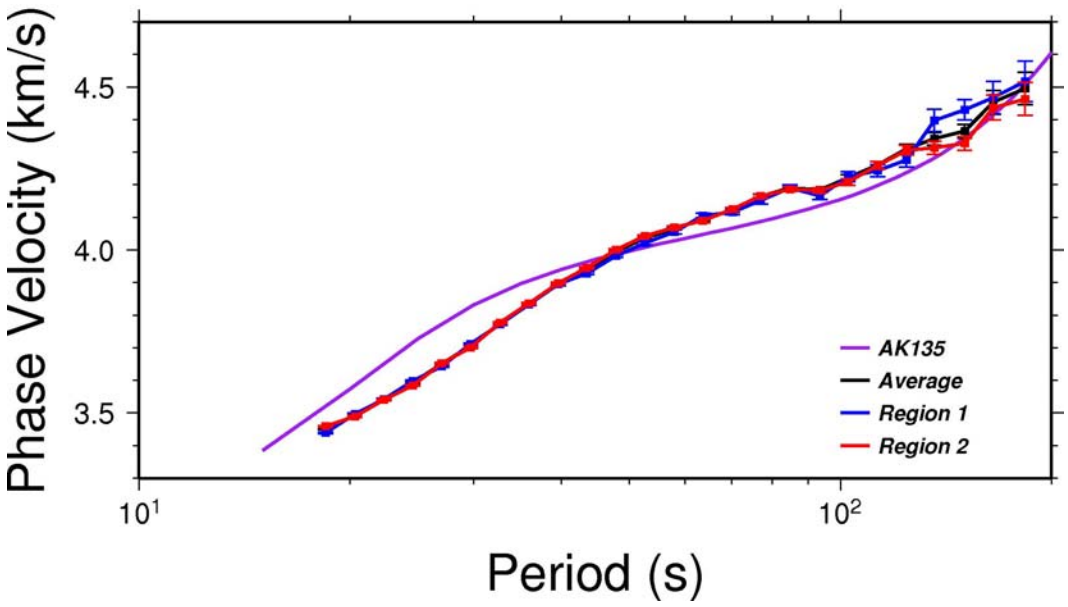

Figure 4.5: 1-D phase velocity curve (black) for study region. Also shown; curves for two regions (blue, red) used in determining anisotropy for multiple regions and predicted dispersion curve (violet) of AK135 [*Kennett et al.*, 1995]. Error bars on y-axis are 2σ uncertainties.

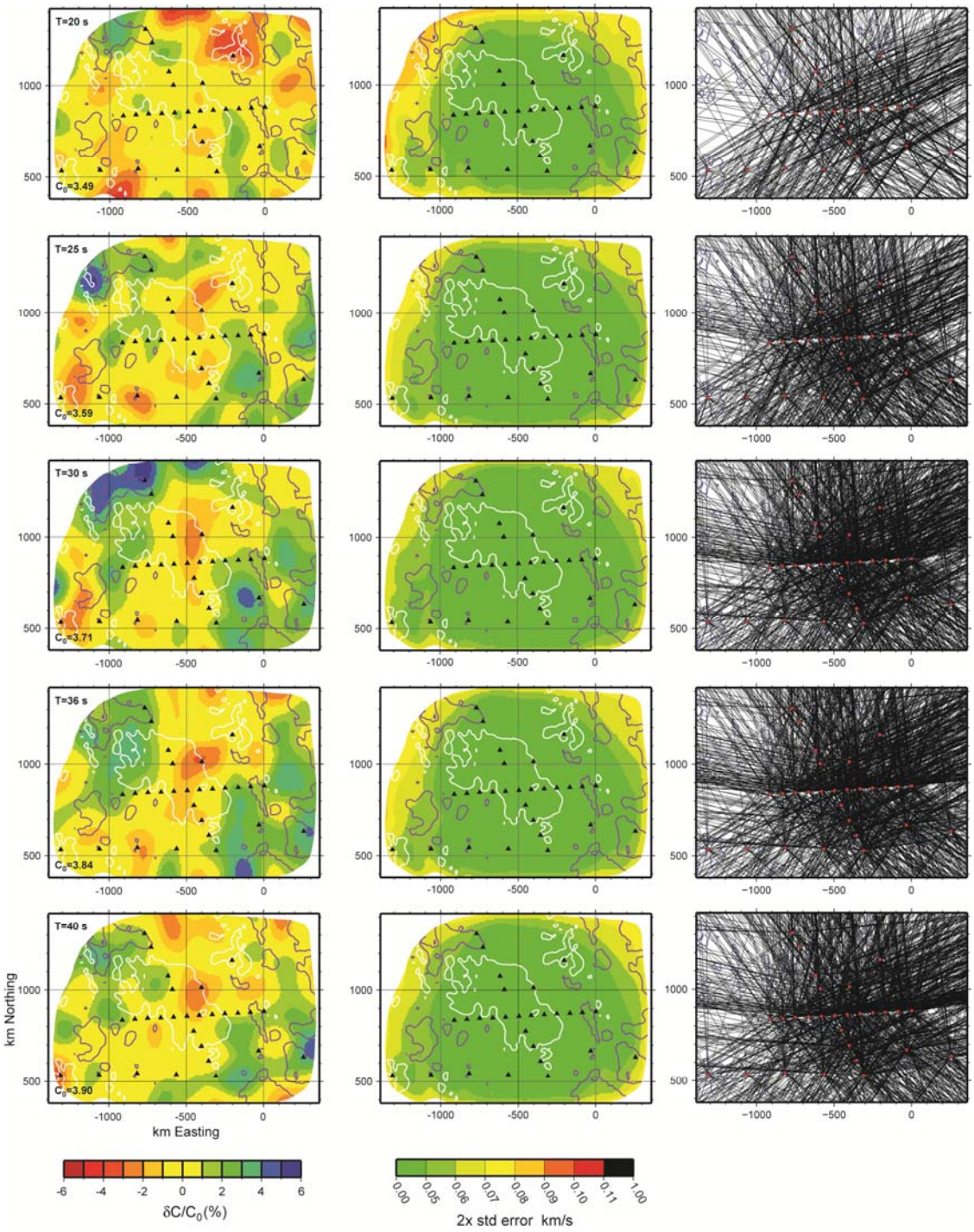
T=20 s
C0=3.49
T=25 s
C0=3.59
T=30 s
C0=3.71
T=36 s
C0=3.84
T=40 s
C0=3.90
km Northing
km Easting
δC/C0(%)
2x std error km/s

Figure 4.6

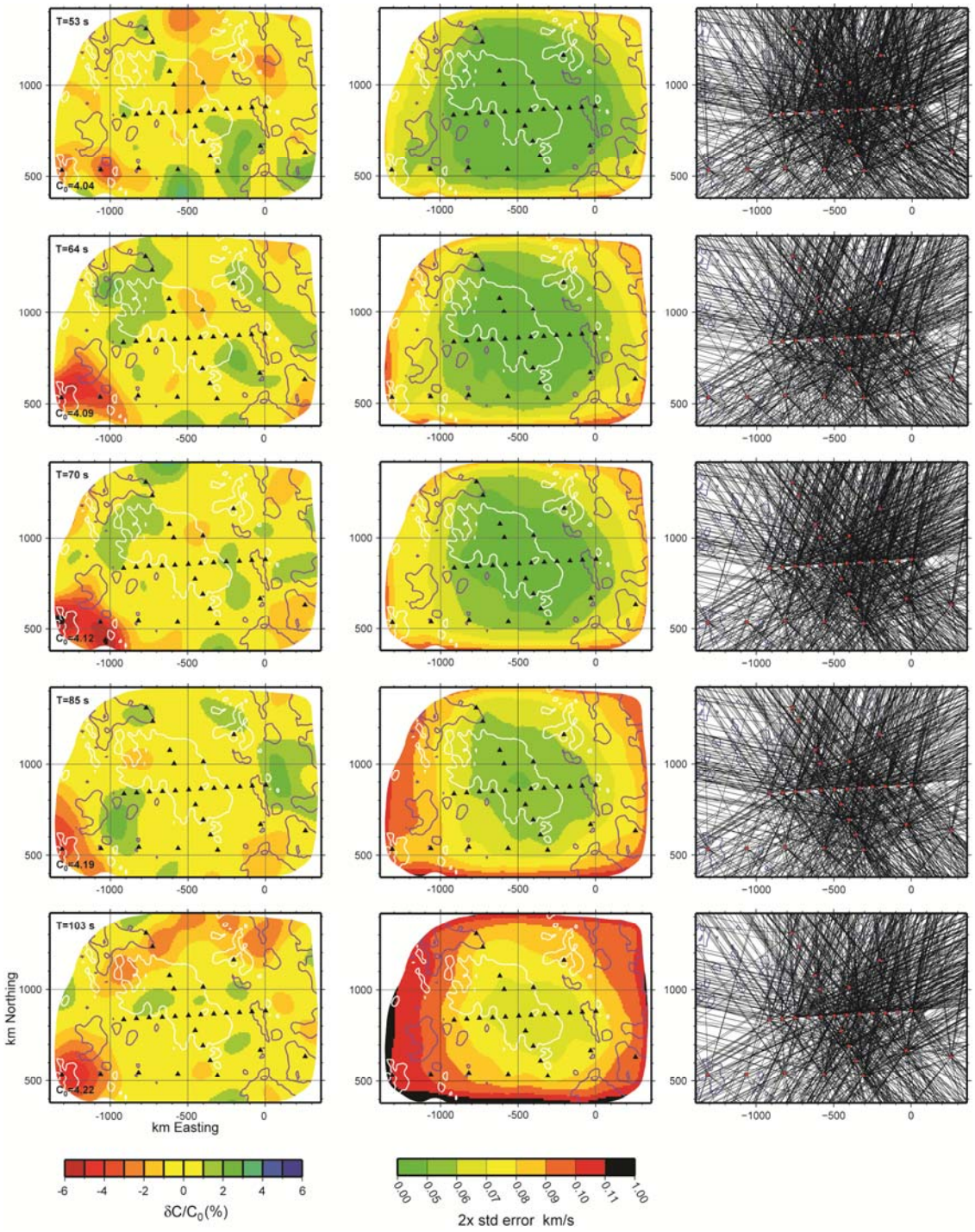

Figure 4.6: Phase velocity maps of the study region masked at the 0.07 km/s uncertainty contour at 33s. Column one is phase velocity, column two 2x standard error, and column three is raypath coverage at period. Period is given in upper left corner of phase velocity map, and average 1-D phase velocity is in lower left. Violet and white contours represent

0m and 1000m bedrock elevations respectively. Triangles/squares are station locations. X and y-axes defined in km easting or northing respectively from the South Pole with the y-axis along 107.5°E longitude.

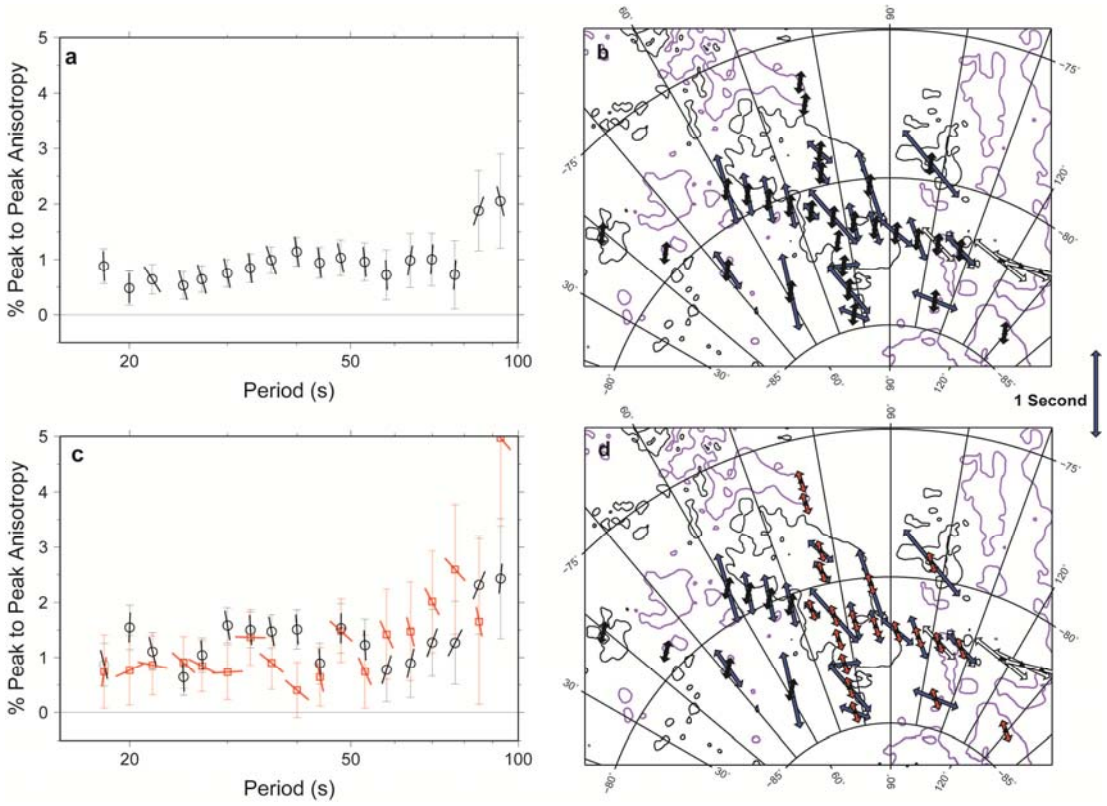

Figure 4.7: Peak-to-peak azimuthal anisotropy amplitude results (a, c) for 2-D phase velocity inversions. Anisotropy amplitude is low <~1% for periods shorter than 100s. Beyond 100s amplitudes increase along with uncertainties. and isotropic velocity model is preferred. Maps (b, d) of fast direction from phase velocities at 53 seconds compared to shear wave splitting results [*Barklage et al.*, 2009; *Hernandez et al.*, 2010] (c,d) Anisotropy results for two regions indicated a more complicated pattern. Amplitudes remain low for periods shorter than 100s, but azimuthal scatter and amplitude uncertainties are greater.

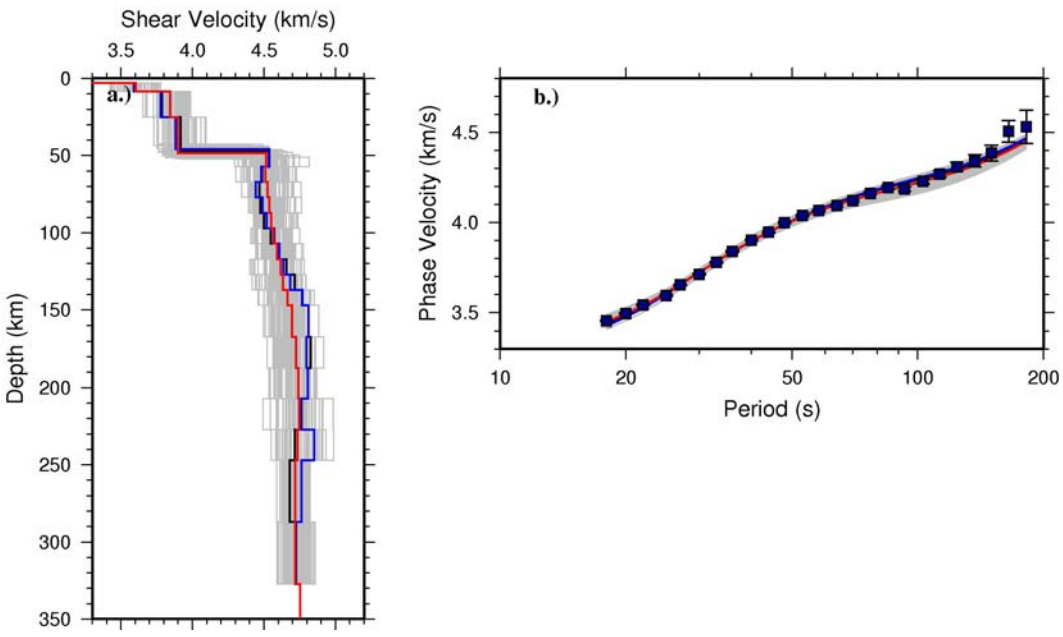

Figure 4.8: 1-D shear velocity model (a) using Monte Carlo method outlined in text and corresponding phase velocity curves (b). Black curve initial velocity model from 1-D inversion. Red curve represents probability-averaged model resulting from 100 acceptable models (grey lines). Monte Carlo resampling of velocity model induces vertical smearing of model. Blue curve is best fitting model, which is rougher than average model and non-reproducible between modeling runs. Blue points in (b) are values from 1-D phase velocity inversion with error bars in y direction representing 2σ uncertainties.

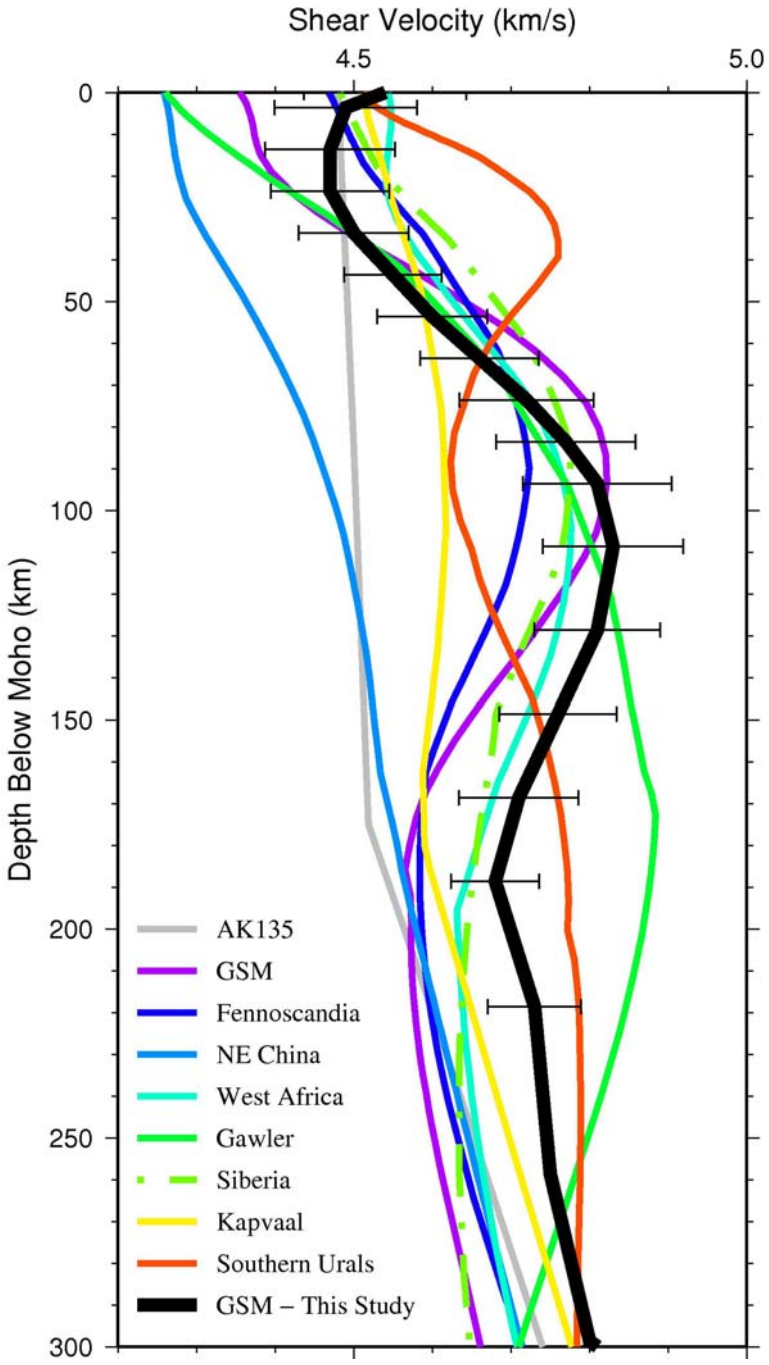

Figure 4.9: Comparison of 1-D mantle shear velocity from this study with cratonic regions around the world extracted from the S_v model of *Shapiro and Ritzwoller*, [2002]. The GSM region fits a variety of cratonic regions at different depths. Most notably, the structure from 70-150 km fits the Southern Ural Mountains, while the uppermost mantle corresponds well with the Kaapvaal Craton of southern Africa1-D model is inverse model

derived from average phase velocity curve. Horizontal error bars denote standard deviation of acceptable models from Monte Carlo modeling.

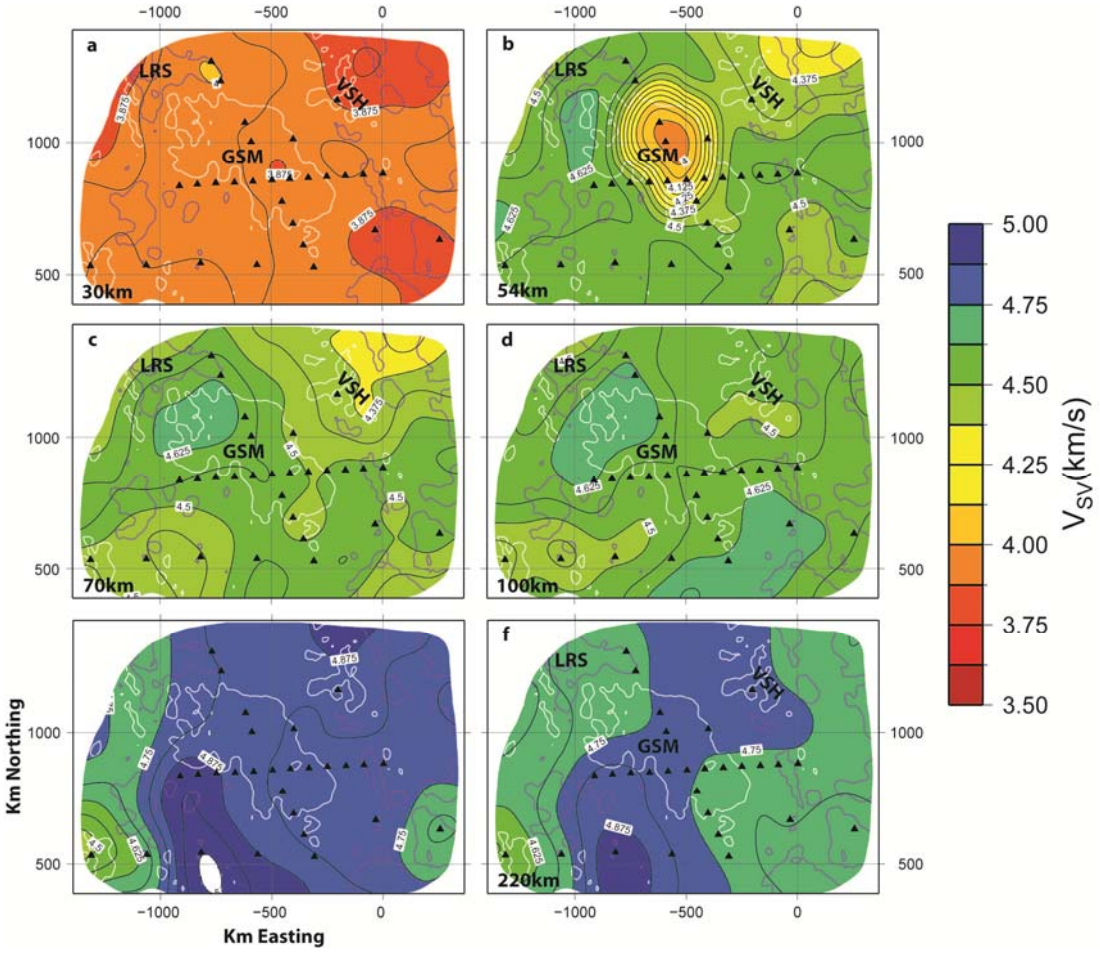

Figure 4.10: Shear velocity maps at a variety of depths. Violet and white contours are 0m and 1000m subglacial bedrock contours respectively and station locations are black triangles. Shear velocities are relatively constant in the crust (a). Differences in crustal thickness are apparent (b) and upper mantle velocities are variable, but not extremely so (c-e).

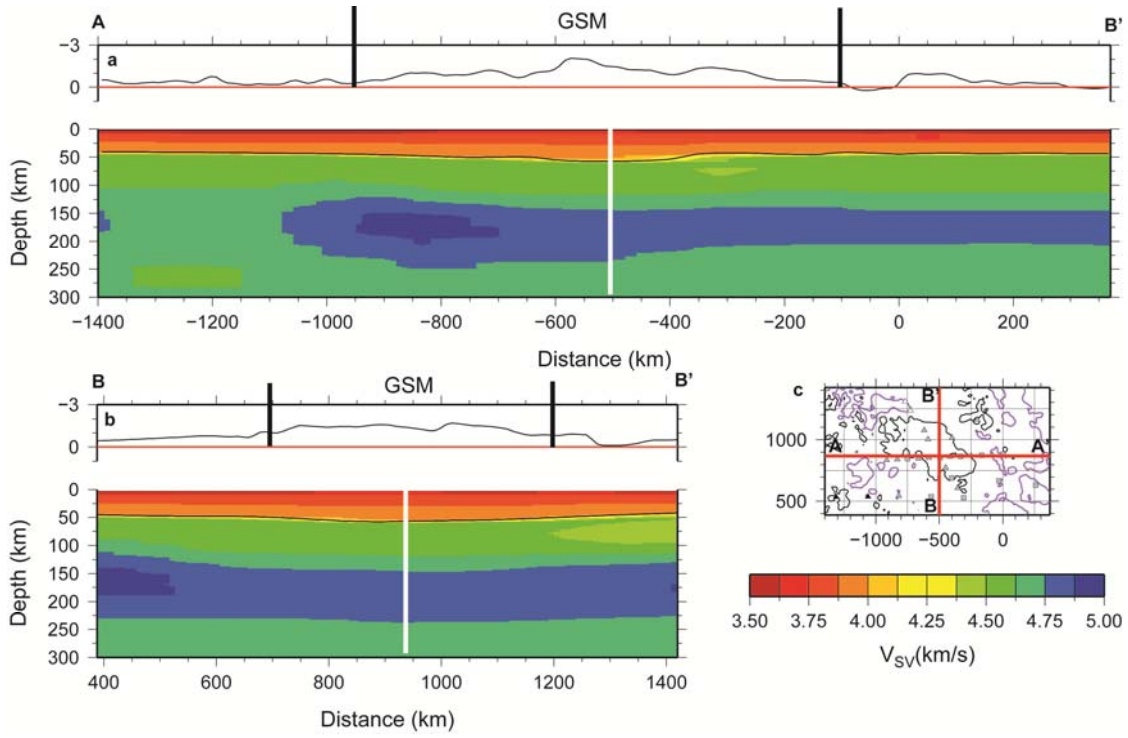

Figure 4.11: Cross sections of shear velocity through the study region. Long cross section (a) closely parallels the N-line of seismic stations across the GSM and the short cross section (b) is perpendicular. Location of cross sections shown in map view in (c). Point of crossover is marked with heavy white line in both cross sections, and approximate location of high elevation associated with GSM (1000m contour (c, black)) marked with black in subglacial topography profiles located above shear velocity models. Moho from receiver functions is marked by black line in velocity profiles.

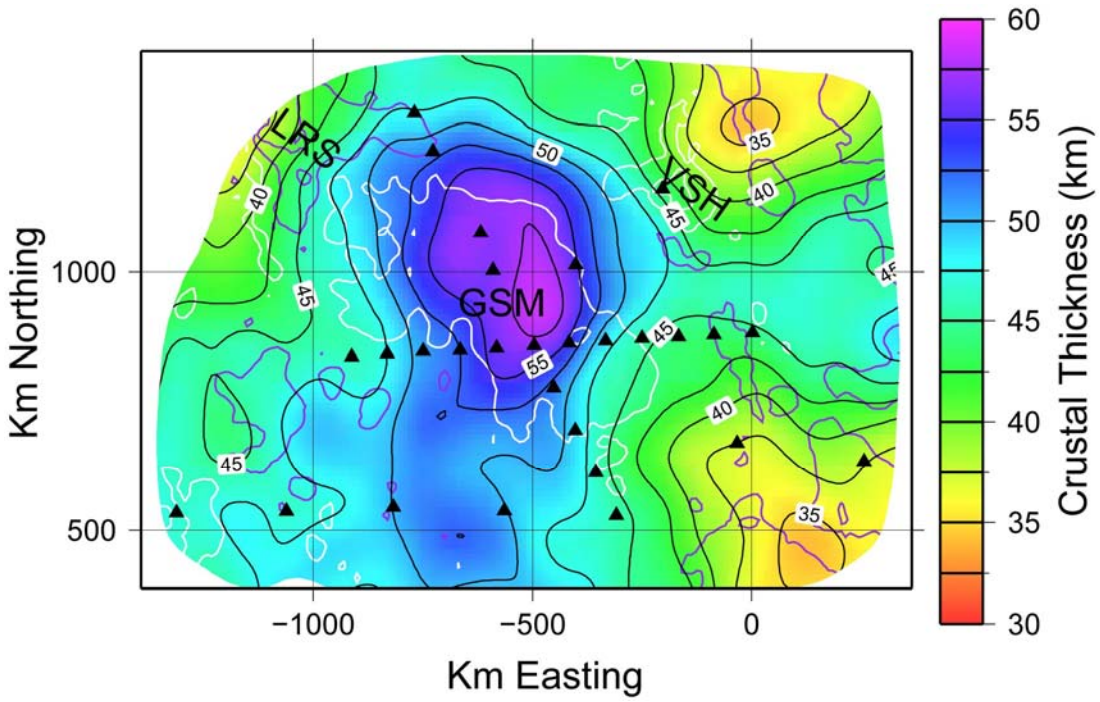

Figure 4.12: Crustal thickness from Monte Carlo resampling of initial estimates based on receiver function studies. The crustal thickness is sampled using the same Gaussian-smoothing operator as the phase/shear velocity inversions. Contour interval is 2.5 km with labels every 5 km. Major topographic features are labeled: Gamburtsev Subglacial Mountains (GSM), Lambert Rift System (LRS), and the Vostok Subglacial Highlands (VSH). We observe the thickest crust beneath the GSM while the thinnest crust is in the LRS and northeast of the VSH in the region of Lake Vostok. Thinner crust is also located extending to the southeast towards the Transantarctic Mountains (figure 4.1).

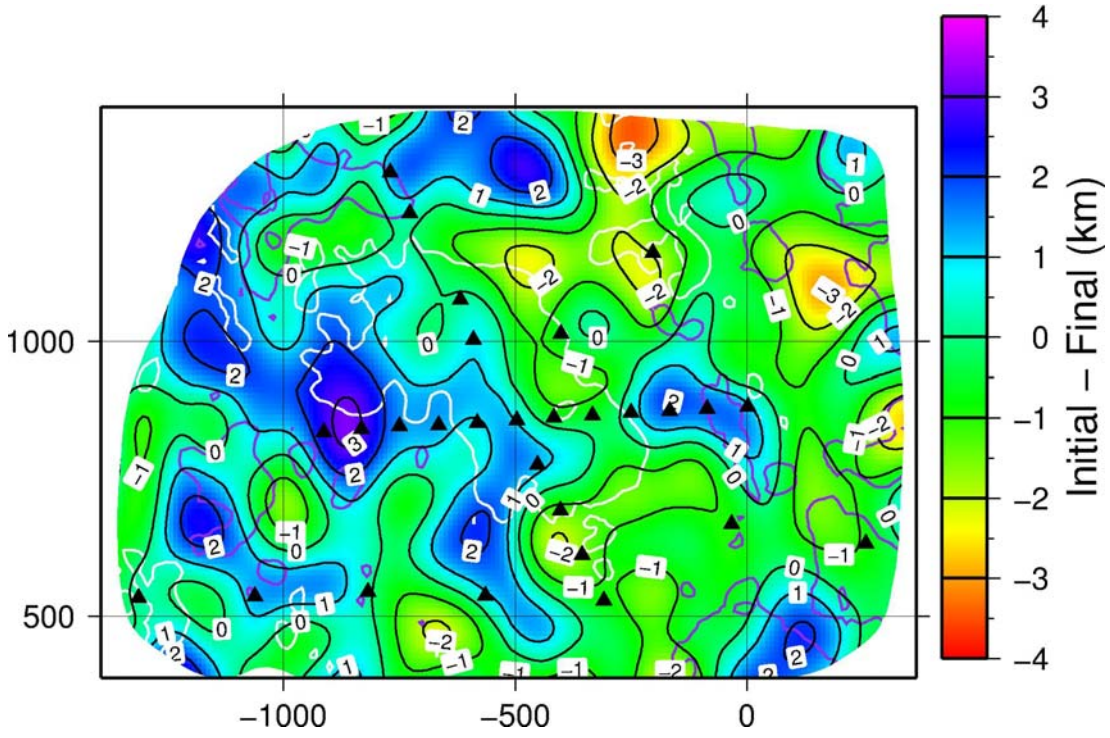

Figure 4.13: Change in crustal thickness between initial model and minimum misfit Monte Carlo model. Regions of positive change signify crustal thinning. The region of thickest crust underlying the GSM shows relatively little change. The region of greatest change in crustal thickness extends from the Lambert Rift System inland beneath the western edge of the GSM.

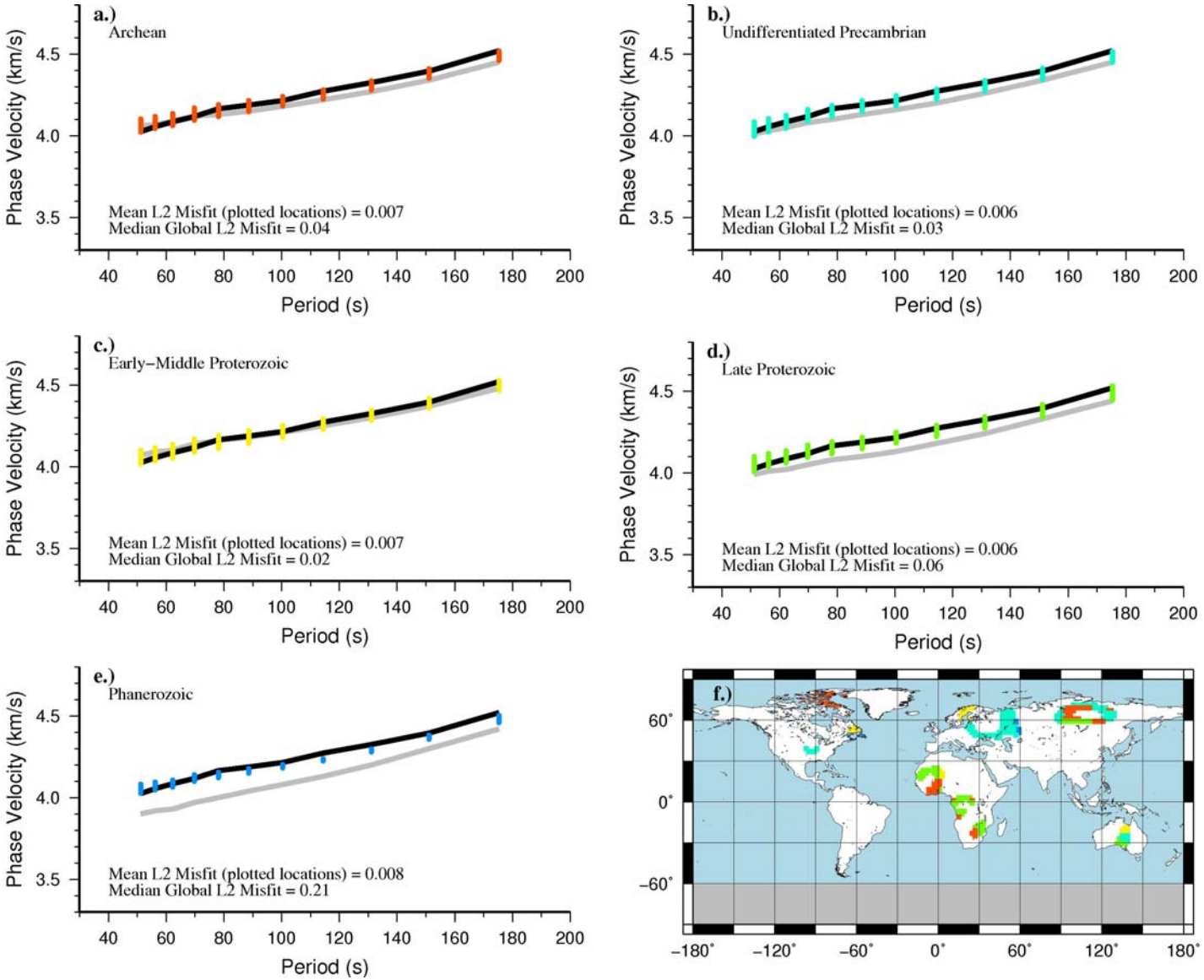
a.)
Archean
Mean L2 Misfit (plotted locations) = 0.007
Median Global L2 Misfit = 0.04
b.)
Undifferentiated Precambrian
Mean L2 Misfit (plotted locations) = 0.006
Median Global L2 Misfit = 0.03
c.)
Early–Middle Proterozoic
Mean L2 Misfit (plotted locations) = 0.007
Median Global L2 Misfit = 0.02
d.)
Late Proterozoic
Mean L2 Misfit (plotted locations) = 0.006
Median Global L2 Misfit = 0.06
e.)
Phanerozoic
Mean L2 Misfit (plotted locations) = 0.008
Median Global L2 Misfit = 0.21
f.)
Phase Velocity (km/s)
Period (s)

Figure 4.14: a-e.) Comparison of 1-D phase velocity results with regions of differing ages using global phase velocity model [*Visser et al.*, 2008]. Ages based on simplified tectonic age map in the crust2.0 model [*Bassin et al.*, 2000; *Mooney et al.*, 1998]. 1-D phase velocity results most closely match the global median (heavy grey lines) for Early-Middle Proterozoic (c) and undifferentiated Proterozoic terranes (b). f.) Map of regions plotted in phase velocity curves. Region south of -60 latitude was not analyzed due to uncertainties in crustal ages.

Chapter 5

Shear velocity structure of central Antarctica from the Gamburtsev Subglacial Mountains to Marie Byrd Land and the Ellsworth-Whitmore Block

The seismic velocity of the Antarctic continent has previously been determined only by large-scale, low resolution studies that utilize little locally recorded data due to the lack of broadband seismometers in the continental interior. Recent temporary broadband seismic deployments allow us to image the upper mantle structure of a large region of the Antarctic continent and resolve features that were previously unrecognizable. Utilizing teleseismic Rayleigh-waves, we perform phase velocity tomography across a study region using the two plane-wave method. Our study region encompasses the Gamburtsev Subglacial Mountains, Transantarctic Mountains, and West Antarctica with the exception of the Antarctic Peninsula. We then invert phase velocities for shear velocity in a damped least-squares manner to develop a three-dimensional velocity structure for the study region. We find that the observed dichotomy in seismic structure between the East Antarctic craton and West Antarctica found in global models is preserved at higher resolution, with West Antarctica showing much thinner crust and slower upper mantle velocity. The thickest crust within the study region underlies the Gamburtsev Mountains East Antarctica. The Central Transantarctic Mountains, a region that others have suggested is underlain by thickened crust is instead marked by a broad, slow velocity

anomaly in the uppermost mantle, suggesting thermally rather than isostatically supported topography. The Ellsworth-Whitmore block, a region of Precambrian crust in Phanerozoic West Antarctica, is underlain by a thicker lithosphere than that under the WARS or Ronne Ice Shelf. Marie Byrd land is also underlain by a thicker lithosphere than the WARS. Additionally, this is the region of deepest slow velocity anomalies.

5.1 Introduction

Due to the challenges associated with deploying seismometers in the harsh climate of Antarctica, the seismic velocity structure of the continent is known primarily through continent scale studies based on teleseismic surface waves [*Danesi and Morelli*, 2000; 2001; *Morelli and Danesi*, 2004; *Ritzwoller et al.*, 2001; *Roult and Rouland*, 1992]. Regional tomography studies to date have focused on the temporary seismic array TAMSEIS [*Lawrence et al.*, 2006a; b; c; *Pyle et al.*, 2010; *Watson et al.*, 2006] and have provided insight into the structure and tectonic setting of the Transantarctic Mountains (TAMS) in the South Victoria Land and Ross Sea region. Two recent International Polar Year deployments of temporary broadband seismic stations across the continent (figure 5.1), particularly in West Antarctica (POLENET) and in the Gamburtsev Subglacial Mountains (GAMSEIS), now allow us to image the seismic structure of a large part of the Antarctic continent to an unprecedented resolution. We utilize data from these deployments as well as from the previous TAMSEIS deployment to conduct teleseismic Rayleigh-wave phase velocity tomography using the two-plane wave method of *Forsyth and Li* [2005]. We then invert the derived phase velocity maps for a three dimensional shear velocity structural model and discuss the implications of the velocity variations for the structure and history of Antarctica.

5.2 Tectonic Setting

The large-scale tectonic framework of the interior of the Antarctic continent is largely unknown. With the exception of rock outcrops near the edges of the continent and in the TAMS, which define the boundary between East and West Antarctica, direct

sampling of subglacial bedrock is limited due to the thick ice cover. Recent tectonic reconstructions, therefore, are based almost solely on extrapolating observed boundaries within regions of outcrop beneath the ice cap, particularly in East Antarctica where outcrop is scarcer than in West Antarctica [*Boger*, 2011; *Dalziel*, 1991; *Dalziel and Lawver*, 2001; *Fitzsimons*, 2000a; b; 2003; *Goodge and Fanning*, 2010; *Moores*, 1991]. Our study region encompasses much of the area within East and West Antarctica covered by the ice sheets and will provide insight into the formation and evolution of the Antarctic continent. What follows is a brief outline of the study region from a local north to south and west to east (upper left to lower right in figure 5.1).

The Gamburtsev Subglacial Mountains (GSM) region in East Antarctica encompass the inland extension of the Lambert Rift System, a Permian rift system associated with the breakup of Pangaea [*Hofmann*, 1991] that was reactivated during the Cretaceous during Gondwana breakup [*Boger and Wilson*, 2003; *Hofmann*, 1991; *Lisker et al.*, 2003]. The GSM themselves are enigmatic and their origin mechanism is debated [*Hansen et al.*, 2010; *van de Flierdt et al.*, 2008]. A focused tomography study of the region (chapter 4) found thickened crust and a fast lithosphere extending to depths of ~225 km. We hypothesize that the modern GSM are of Permian origin and represent a reactivation of an older structure possibly dating to the Early Proterozoic (chapter 4). A series of subglacial basins and intervening highlands lie between the GSM and the TAMS. These basins represent major subglacial topographic lows and their large scale, internal structure is known primarily through geophysical studies [*Ferraccioli et al.*, 2009; *Pyle et al.*, 2010; *Stern and ten Brink*, 1989; *Studinger et al.*, 2004; *ten Brink and Stern*, 1992; *ten Brink et al.*, 1993]. The TAMS represent the boundary between East and

West Antarctica. Through geologic time, the region has undergone multiple instances of orogenesis including the Nimrod (~1.7 Ga) [*Dalziel*, 1991; *Goodge et al.*, 2001; *Moores*, 1991] and the Ross-Delamarian orogenies (550-450Ma) [*Fitzsimons*, 2000b]. Current uplift of the TAMS has been linked to flexural uplift associated with the West Antarctic Rift System (WARS) [*Stern and ten Brink*, 1989; *ten Brink and Stern*, 1992; *ten Brink et al.*, 1993], with crustal thickening [*Studinger et al.*, 2004], or a hybrid model of flexural uplift coupled with limited crustal thickening [*Lawrence et al.*, 2006c].

West Antarctica is comprised of several small tectonic blocks [*Dalziel and Elliot*, 1982; *Jankowski and Drewry*, 1981]. The WARS, extending from the Ross Sea to the Ellsworth-Whitmore block, has been undergoing continental rifting beginning in the Mesozoic and extending into the Cenozoic [*Cooper and Davey*, 1985; *Davey and Brancolini*, 1995; *T J Wilson*, 1995]. Evidence from the Ross Sea Embayment indicates multiple pulses of extension are required to fit paleomagnetic observations in the southern Pacific Ocean [*Cande et al.*, 2000; *Davey et al.*, 2006; *DiVenere et al.*, 1994; *D S Wilson and Luyendyk*, 2006]. Mylonite shear zones in Marie Byrd Land indicate an end to extension on this flank of the WARS at ~ 85-90 Ma [*Siddoway et al.*, 2004]. However, there is good evidence for continued Cenozoic extension in the Ross Sea [*Davey et al.*, 2006; *D S Wilson and Luyendyk*, 2009]. This is consistent with geodynamic modeling that supports an progression from a broad region of extension during the early stages of WARS formation to a more focused form of extension along the TAMS during later stages [*Huerta and Harry*, 2007]. The TAMS and the Ellsworth-Whitmore Mountain block, a region of Precambrian East Antarctica that has separated and rotated to West Antarctica, bound the west of the region [*Dalziel and Elliot*, 1982; *Grunow et al.*, 1991].

To the west of the Ellsworth-Whitmore block is a series of granitic nunataks that formed as a result of the rotation of the Ellsworth-Whitmore block into West Antarctica and connect the region to the Thiel Mountains in East Antarctica [*Dalziel and Elliot*, 1982].

Marie Byrd Land and the Thurston Island Block define the other edge of the rift system within the study area. Marie Byrd Land is an uplifted region of crust that has undergone Cenozoic magmatic and volcanic activity [*Corr and Vaughan*, 2008; *Hole and LeMasurier*, 1994; *Paulson and Wilson*, 2010]. Recent work has supported a plume hypothesis for uplift of Marie Byrd Land. Lines of evidence include igneous rocks with a plume affinity [*Panter et al.*, 1997; *Weaver et al.*, 1994] and deep seated thermal anomalies observed seismically [*Sieminski et al.*, 2003]. Topography results indicating ~3 km of uplift since 28-30 Ma also support a plume hypothesis for the development of the Marie Byrd Land dome [*LeMasurier and Landis*, 1996].

5.3 Data and Methods

5.3.1 Seismic Arrays and Data Selection

Data for this study were collected from three large seismic arrays and are supplemented by data from three permanent seismic stations, one at the South Pole, and two in the Ross Sea region (VNDA and SBA). The TAMSEIS array consisted of a temporary deployment of 47 seismic stations during the Austral summers of 2001-2003 (table 5. 1). The array consisted of three sub-arrays: a coastal array on the Ross Sea in the region of Ross Island; an east-west array extending from McMurdo station, across the TAMS, and onto the East Antarctic Ice Sheet; and a north-south array that ran form Terra Nova Bay, across the TAMS, and onto the East Antarctic Ice Sheet. The GAMSEIS

array (table 5. 2) was a multinational, temporary deployment of 28 broadband seismic stations designed to study the seismic structure of the Gamburtsev Subglacial Mountains in East Antarctica during the 2007-2010 International Polar Year. The array consisted of two lines of stations, one being an extension of the north-south TAMSEIS deployment and the other crossing near Dome A. The final temporary array utilized in this study is the Antarctic portion of the POLENET study (table 5. 3). This ongoing seismic array consists of 33 stations for which data has been collected and is designed to study the crustal and upper mantle structure of West Antarctica. It consists of two elements; a backbone array of 23 stations located throughout TAMS and at strategic locations throughout the West Antarctic Ice Sheet and Ellsworth Mountains and a shorter term transect of 10 stations extending from the Whitmore Mountains to Marie Byrd Land, crossing the West Antarctic Rift System (WARS). Both the POLENET data and the TAMSEIS data are supplemented with data from permanent stations associated with the Global Seismic Network (GSN). Together these three arrays allow us to image the seismic structure of the Antarctic continent from the GSM to Marie Byrd Land at unprecedented levels of detail.

We select Rayleigh wave data based on distance from the array and the surface wave magnitude of the earthquake (figure 5.3). We select earthquakes with $M_S \geq 4.5$ for epicentral distances of 30-60 degrees. For distance of 60-150 degrees, we reset the minimum M_S at 5.5. Less stringent magnitude requirements for earthquakes occurring nearer the arrays allows us to take advantage of the circum-Antarctic ridge system and subduction zones in the southern hemisphere (figure 5.4). All earthquakes used in this study have a depth less than 100 km. Instrument response is removed from all data, and

we visually inspect data for high signal-noise ratio and a lack of data glitches. We filter high quality data at 25 periods between 18 and 182 seconds and apply a time window around the fundamental mode Rayleigh wavetrain. The filters are composed of two-pass four-corner Butterworth filters with corners at ±10% of the center frequency.

5.3.2 Phase velocity inversion

We conduct teleseismic Rayleigh wave tomography with these three arrays using the two plane-wave method [*Forsyth and Li*, 2005]. By utilizing both phase and amplitude information, we model the incoming surface wave as the interference of two plane waves. The method improves on traditional surface wave tomography methods by better reducing the errors associated with wavefield scattering, multipathing, and off great-circle path effects [*Forsyth and Li*, 2005; *Li et al.*, 2003]. We further utilize modifications to the method that reduce the effect of off-great circle path energies by including 2-D sensitivity kernels [*Yang and Forsyth*, 2006] based on the Born approximation[*Zhou et al.*, 2004].

Here we provide a short description of the inversion scheme. For a more complete description of the two plane-wave inversion scheme and its application to Antarctica, see Chapter 4. In order to preserve the plane-wave assumption that our inversion scheme is based on, we adopt an approach in which we break the seismic array into multiple sub-arrays and process a single earthquake observed across the entire array as a separate earthquake in each sub-array (white boxes in figure 5.1). This allows us to preserve the plane-wave assumption locally and invert all of the data at the same time, constructing a single phase velocity model [*Yang et al.*, 2008b]. The alternative to this

approach is to invert for each sub-array separately and average regions of overlap [*Yang and Ritzwoller*, 2008], which would add computational complexity to the models and increasing uncertainty in the regions of overlap. In the first stage we invert for 1-D phase velocity structure across the East Antarctic and West Antarctic subregions within the study area (figure 5.2). This division is necessary as the crust and upper mantle velocity structure in the two regions differ greatly (figure 5.5) [*Block et al.*, 2009; *Danesi and Morelli*, 2001; *Lawrence et al.*, 2006c; *Ritzwoller et al.*, 2001]. In the second stage, we invert for both 2-D phase velocity variations across the study region and azimuthal anisotropy in the subregions. We discretize the study region into 1120 nodes with primary, central region having a node spacing of 110 km. Two rows of nodes around the edges have a spacing of 220 km to act as a buffer and absorb the effects of seismic structure outside of the study region.

The inversion scheme solves for the 2-D phase velocities in a continuous manner. To produce phase velocity maps, we perform Gaussian interpolation of the results with a smoothing length of 200 km, and we assume an *a priori* data variance estimate of 0.2. We define a local reference frame with north along 107.5° longitude and the origin at the South Pole, and plot results in this local frame of reference. All phase velocity, and subsequently derived shear velocity maps are plotted within this local frame of reference.

5.3.3 Shear Velocity Inversion

In order to make meaningful tectonic interpretations of surface wave tomography, we must invert the observed seismic structure for depth dependent shear velocity. We do this by extracting a phase velocity curve at each node and inverting for shear velocity

using a damped least-squares approach [*Herrmann and Ammon*, 2004]. We then construct a 3-D velocity model by applying the same smoothing constraints to the shear velocity model as we did to the phase velocities.

The thickness of the ice layer is important to the accurate inversion of phase velocity structure for shear-wave velocities [*Ritzwoller et al.*, 2001]. Therefore, we extract an estimated ice thickness from the BEDMAP subglacial topography model [*Lythe et al.*, 2001]. Although phase velocities can provide constraints on crustal thickness, an estimate of the crustal thickness is required for the starting model. Crustal thickness estimates derived from global compilations of past data, such as Crust5.1 [*Mooney et al.*, 1998] are unreliable throughout much of Antarctica because of the paucity of seismic refraction results. To estimate crustal thickness across the study region we instead compile receiver function estimates of crustal thickness for the study region and surrounding areas [*Agostinetti et al.*, 2004; *Chaput et al.*, 2011; *Finotello et al.*, 2011; *Hansen et al.*, 2009; *Hansen et al.*, 2010; *Reading*, 2006; *Studinger et al.*, 2003; *Winberry and Anandakrishnan*, 2004]. We then construct a model of crustal thickness at node locations that is a smoothed average of the receiver function estimates using the same Gaussian smoothing operator applied in the phase and shear velocity models. We divide the crust into three layers; a thin upper crust that is $1/8^{th}$ the total crustal thickness, a thicker mid-crust ($3/8^{ths}$ the total crustal thickness), and a lower crust (1/2 the total crustal thickness). The upper 100 km of the mantle is divided into 10 km thick layers. We divide the next 80 km into 20 km thick layers and the remainder of the upper mantle at 40 km. We are most interested in crustal and uppermost (<250 km) mantle structure. However, we allow for some changes in the velocity model to depths of 400 km to limit

smearing of deeper structure that the longest period data is sensitive to into our upper mantle imaging. We use the upper mantle structure of AK135 [*Kennett et al.*, 1995] as a starting model.

$$C = \chi^2_{red} \times \sqrt{ISE} \quad (1)$$

$$\chi^2_{red} = \frac{1}{N}\sum_{i=1}^{n}\frac{(d_i^{obs} - d_i^{pred})^2}{(\sigma_i^{obs})^2} \quad (2), \quad ISE = \sum_{i=1}^{m}\left(\frac{\partial^2 V}{\partial z^2}_{inverse} - \frac{\partial^2 V}{\partial z^2}_{model}\right)^2 \quad (3)$$

In order to constrain the uncertainty of shear velocity inversion, we conduct Markov chain Monte Carlo simulations of the average 1-D structure for both regions. The method is discussed in detail in chapter 4, but we provide a brief review here. We conduct our Monte Carlo modeling by first randomly perturbing the crustal and upper mantle velocity structure (±5% in crust, ±7% in upper 100 km of mantle, and ±3% in next 80 km) and the crustal thickness (±5 km). A phase velocity curve is then generated and a cost function (1), which is a combination of the misfit between the observed and predicted phase velocity curves (2) model roughness (3), calculated. If the cost of the model is below a threshold ($5xC_{inverse}$) then it is considered acceptable and we include it in a probability weighted mean and standard deviation. Due to the large number of nodes (2.3x those used in chapter 4), it is computationally unfeasible to conduct a 3-D Monte Carlo simulation. Rather we estimate our model uncertainty based on the 1-D model for the regional averages (figure 5.11).

5.4 Results

5.4.1 Phase velocities

5.4.1.1 1-D phase velocities

One dimensional phase velocity curves are presented in figure 5.5. The phase velocity structure of East and West Antarctica are distinctly different, a result that is consistent with other surface wave studies of the region [*Danesi and Morelli*, 2000; 2001; *Lawrence et al.*, 2006b; *Ritzwoller et al.*, 2001]. The phase velocity curve that represents an average of the entire study region is a hybrid of the two regional models. Our results are broadly similar to those determined for the eastern Ross Sea and adjacent parts of East Antarctica by *Lawrence et al.* [2006c] at periods less than 100 seconds, though they vary significantly at longer periods. The larger geographic region imaged in this study limits direct comparisons of our results to the more spatially limited results of *Lawrence, et al.* [2006c].

5.4.1.2 2-D phase velocities

The results of the 2-D phase velocity inversions show large and well resolved variability in structure across the study region (figures 6-9). Slow phase velocities characterize East Antarctica relative to West Antarctica to periods of 20-30 seconds (figure 5.8). The most notable slow velocity anomalies are concentrated beneath the Gamburtsev Subglacial Mountains the central portion of the TAMS (figure 5.8). These are both regions of elevated topography, and the GSM are characterized by thickened crust [*Block et al.*, 2009; *Hansen et al.*, 2010; *von Frese et al.*, 1999], which accounts for the slow phase velocities in the region. The central TAMS are also defined by slower than average phase velocities but this anomaly extends to significantly greater periods than are observed beneath the GSM (figure 5.9). *Block et al.* [2010] found crustal thicknesses in excess of 45 km in the region based on satellite gravity lows, a result that

is consistent with the observed phase velocities at periods of 18-50 seconds. However, phase velocity observations within the central region of the TAMS, which are relatively slow to periods in excess of 100 seconds, indicate that there is thermal rather than isostatic argument for the bedrock elevations observed in this region.

At longer periods, consistent with mantle depths, we observe phase velocities that are faster than the 1-D average model in the interior of East Antarctica. The observed phase velocity anomalies in this region are consistent with a cratonic lithosphere, which supports the hypothesis that the bulk of East Antarctica is comprised of Archean/Paleoproterozoic crustal blocks that were assembled during the Precambrian [*Boger*, 2011; *Boger et al.*, 2001; *Dalziel*, 1991; *Elliot*, 1975; *Fitzsimons*, 2000a; b; 2003; *Goodge and Finn*, 2010; *Goodge et al.*, 2010]. Due to the smoothing length (200 km) required in assembling this geographically extensive model, we are unable to image the East Antarctic craton with high resolution. This limits our ability to say anything about the numerous possible suture zones that have been proposed to cross East Antarctica by various authors [*Boger*, 2011; *Fitzsimons*, 2000a; b; *Goodge et al.*, 2008; *Studinger et al.*, 2003]. Chapter 4 presents a higher resolution model focused on East Antarctica and discusses the implications in more detail.

West Antarctica is distinctly different from East Antarctica in two-dimensional phase velocity inversions, as was seen in the 1-D average inversions. The shortest period observations (18-30 seconds) have significantly faster than average phase velocities (figure 5.8). The central region of the WARS is 3-4% faster than the continental velocity model AK135 and ~6% slower than PREM. This observation is consistent with a continental crust that has undergone thinning by extensional processes (figure 5.12,b)

[*Weeraratne et al.*, 2003; *West et al.*, 2004; *D Wilson et al.*, 2005]. At longer periods (>36 seconds), phase velocities in West Antarctica are consistently slower than global averages. Slow velocity anomalies are concentrated beneath Marie Byrd Land and in the Ross Sea region, extending inland towards the Central Transantarctic Mountains. These relatively narrow and concentrated phase velocity anomalies appear to broaden with increasing period (figure 5.9). At the longest periods (150-182 seconds) the slow velocity anomaly that defines West Antarctic narrows and is centered beneath Marie Byrd Land.

5.4.2 Shear Velocities

5.4.2.1 1-D Shear Velocities

The 1-D shear velocity models for East and West Antarctica are distinctly different, with resolvable differences extending to at least 220 km (figure 5.10). We invert average phase velocity for both regions using a 1.5 km thick ice layer, an average crustal thickness from receiver functions (EA = 42 km; WA = 28 km), and a starting model with upper mantle velocities from AK135 [*Kennett et al.*, 1995]. East Antarctica is underlain by a mantle that has a slight velocity minimum at depths of 60-110 km, consistent with other cratonic regions [*Yuan and Romanowicz*, 2010]. Below this, seismic velocities increase to a depth of 185 km, and then decrease to a depth of 270 km before returning to values consistent with the global average. West Antarctica, on the other hand, is defined by a marked slow velocity anomaly in the upper mantle. From directly below the Moho to a depth of 105 km shear velocities are consistently

decreasing. While velocity increases below this, slow seismic velocities persist to a depth of 250 km.

It is informative to compare our shear velocity results to others from around the world. To that end, we chose several locations with similar tectonic settings and compare our results to the SV shear velocities of the CUB model [*Shapiro and Ritzwoller*, 2002], an anisotropic shear velocity model generated by inverting surface wave phase and group velocities. East Antarctica has a structure similar to other cratonic regions around the world (figure 5.11,a) and is faster than AK135 [*Kennett et al.*, 1995] to a depth of ~250 km. In contrast, West Antarctica has an upper mantle that is significantly slower than the global average and is similar in structure to other regions undergoing continental scale extension (figure 5.11,b). Notably different from some other regions undergoing continental extension is the presence of a lithospheric lid. This lid may be indicative of a region of slowing or failing extension [*Huerta and Harry*, 2007].

5.4.2.2 3-D Shear Velocities

In order to generate a three-dimensional shear velocity volume for the study region, we extract a phase velocity curves at each inversion node and invert for depth dependent shear velocity. We then construct our 3-D model from these 1-D models by applying the same Gaussian averaging length as is used to generate the phase velocity maps [*Li et al.*, 2002; *Weeraratne et al.*, 2003; *Yang et al.*, 2008a]. We can then extract 2-D shear velocity maps illustrating lateral variation at a constant depth (figures 12-13) or cross sections of shear velocity as a function of depth (figures 14-16).

While crustal thicknesses are fixed in the inversion, *a priori* predictions from receiver function studies fit our phase velocity curves well. The thickest crust is located beneath the GSM where crustal thickness exceeds 50 km [*Hansen et al.*, 2010]. In contrast, fast seismic velocities in excess of 3.8 km/s are located at a depth of only 10 km in the West Antarctic Rift System (figure 5.12a) and phase velocities for West Antarctica are fit best by a significantly thinner crust than that of East Antarctica.

Strong shear velocity variations within the upper mantle of the study region closely parallel those observed in phase velocity. We observe the fastest mantle velocities in East Antarctica extending from the edge of the map in the northeast across the Wilkes Subglacial Basin and the Vostok Highlands to the central region of the GSM (figure 5.13). Mantle velocities are reached across West Antarctica at depths of only 20-25 km across much of West Antarctica in contrast to >40 km in East Antarctica. At depths of 70-140 km slow shear velocity anomalies expand from a relatively narrow region along the TAMS front and the central WARS to encompass the entirety of West Antarctica with the exception of the Ellsworth-Whitmore Subglacial Mountains (figure 5.13). Instead, faster seismic velocities, intermediate between East and West Antarctica characterize this region at depths of 70-150 km. Shear velocities in Marie Byrd Land are also different than those in the WARS. Here we observe faster velocities than those in the WARS from depths of 70-150 km, indicating a thicker lithosphere.

5.5 Discussion

5.5.1 East Antarctica

The East Antarctic craton is defined by fast seismic velocities to depths of greater than 200 km throughout most of the region imaged. Cross sections extending from the southward extension of the Lambert Rift System (RFS) across the Gamburtsev Subglacial Mountains (GSM) and Wilkes Subglacial Basin and terminating in the Ross Sea region (figure 5.14) show high mantle seismic velocities and thick crust underlying much of the craton. The region of greatest lithospheric thickness (figure 5.13d) underlies the proposed inland extension of the 'Mawson craton' [*Boger*, 2011; *Fitzsimons*, 2003; *Goodge et al.*, 2010]. However, rather than following the curve of the TAMS as has been proposed, it extends across the GSM. Fast velocities within the mantle lie well poleward of the central TAMS (figure 5.14, 5.15) suggesting that the region directly underlying the highest region of the Transantarctic Mountains has undergone significant thermal modification during the process of continental extension in the WARS.

5.5.2 Central Transantarctic Mountains, West Antarctic Rift System, and the Ross Sea Region

As noted previously, the Central Transantarctic Mountains are underlain by slow shear velocities to a depth of 150 km (figure 5.15). This anomaly extends eastward beneath the Ross Ice Shelf and the Ross Sea, where it deepens. The region of shallowest slow anomalies generally lies along the TAM front from Ross Island in the north to the Ellsworth Mountains in the south, with the exception of the central portion of the WARS (figure 5.13a). *Watson et al.* [2006] noted this feature in the Ross Island region of their study, but due to the limited extent of the array across the Ross Embayment, they were unable resolve the structure fully or comment on it lateral extent. We find that this strong

horizontal gradient continues southwest along the edge of the TAMS before broadening beneath the onshore portion of the rift system and ultimately continues south to the Ellsworth Mountains. *Huerta and Harry* [2007] modeled extension in the Ross Sea portion of the WARS and found evidence for a progression from diffuse extension early in rift history to focused extension along the Victoria Land Basin near the boundary of East and West Antarctica. We propose that a similar progression can be seen in the velocity structure extending from the Ross Sea inland to the central TAMS and that the last stage of extension within the WARS was concentrated along the TAM front consistent with paleotopography analysis of the Ross Sea basin [*D S Wilson and Luyendyk*, 2009].

5.5.3 Marie Byrd Land

There is significant variation in the thickness of the lithospheric lid across Marie Byrd Land (figure 5.13). The northern portion underlying the Ford Ranges has a thicker lithosphere (~90 km) than the central and southern region (~75km). Additionally, the maximum depth of slow velocities in the region is located beneath the central portion of Marie Byrd Land (figure 5.13d). Northern regions, particularly the Ford Ranges and Fosdick Mountains are underlain by granodiorites of Devonian and Cretaceous age with Cretaceous mafic dikes and minor Pleistocene volcanics [*Luyendyk et al.*, 2003]. Magnetic trends in the region are linked to extension during the development of the WARS and Marie Byrd Land's separation from the Campbell Plateau and New Zealand [*Ferraccioli et al.*, 2002]. Further south, at Mount Sidley in central Marie Byrd Land, surface rocks are more mafic and show a strong plume affinity [*Panter et al.*, 1997]. A

plume hypothesis for the central region of Marie Byrd Land is also consistent with our shear velocity results in the region which indicate a deep seated slow velocity anomaly beneath the central region of Marie Byrd Land. While we are unable to image the bottom extent of this anomaly, other researchers have suggested a transition zone source for the Marie Byrd Land hotspot [*Sieminski et al.*, 2003].

5.5.4 Ellsworth – Whitmore Mountains

The Ellsworth Whitmore Mountains of West Antarctica are a region of Precambrian crust that has been incorporated into West Antarctica [*Dalziel and Elliot*, 1982]. Phase velocities in the region are fit well by a crustal thickness greater than that of the WARS [*Chaput et al.*, 2011], a finding consistent with the thicker crust that underlies East Antarctica. However, the upper mantle of the Ellsworth Mountains is distinct from East Antarctica. We observe a significant shear velocity anomaly underlying the Ellsworth Mountains to depths of ~125 km (figures 13 and 16). West of the Ellsworth Mountains, towards the Ronne Ice Shelf, this velocity anomaly ends; marking the westward extent of WARS related seismic velocity anomalies in the region. We suggest that much like the Central Transantarctic Mountains, thermal effects in the upper mantle rather than simple isostatic compensation of their thicker crust support the Ellsworth Mountains, in part. East of the Ellsworth Mountains lies the southern extent of the WARS. In this portion of the WARS, slow velocities extend to depth of ~175 km. Lithospheric thickening occurs from west to east across the rifted crust and reaches a maximum of 125 km beneath Marie Byrd Land (figure 5.16). This is consistent with observations further north.

5.6 Conclusions

We determine phase velocities from teleseismic Rayleigh waves and invert them to create a three-dimensional model of the Antarctic continent extending from the Gamburtsev Subglacial Mountains in East Antarctica to Marie Byrd Land and the Ellsworth-Whitmore Mountains in West Antarctica. East Antarctica is defined by a thick crust and fast lithospheric root extending to depths of ~250 km. In contrast, thin crust and slow mantle velocities consistent with regions undergoing extension underlie West Antarctica. A sharp vertical velocity contrast defines the Ross Sea region, whereas the boundary is diffuse beneath central TAMS, and slow velocities extend across the WARS into Marie Byrd Land. We find little evidence for thick crust beneath the central TAMS, rather we suggest that observed topography within the region is due to thermal uplift. The Ellsworth Subglacial Mountains represent an old lithospheric block that has undergone thermal modification of its lithosphere, though there is still evidence for a lithosphere. In the WARS we observe thin, seismically fast crust and slow upper mantle velocities consistent with continental rifting. Marie Byrd Land is underlain by a thicker lithosphere than the WARS, but slow mantle velocities are observed here as well. These slower velocities are observed to depths of >200 km beneath the center of Marie Byrd Land.

5.7 Acknowledgements

We would like to acknowledge the hard work and support of all the field teams associated with the collection of data presented here. We would also like to thank the

staff and polar support specialists at PASSCAL who developed and aided in the deployment of the equipment for these projects. We thank the pilots and staff of Kenn Borek Air and the New York Air Guard for flight support and the staff at AGAP-S camp, Byrd Camp, South Pole Station, McMurdo Station, ALE, and Raytheon Polar Services for logistical support. This research is supported by NSF grants ANT-0537597, ANT-0838934, ANT- 0632209, and ANT- 9909603. The majority of figures in this work were produced in GMT [*Wessel and Smith*, 1998].

5.8 References

Agostinetti, N. P., A. Amato, M. Cattaneo, and M. D. Bona (2004), Crustal structure of Northern Victoria Land from receiver function analysis, *Terra Antarctica*, *11*(1), 5-14.

Block, A. E., R. E. Bell, and M. Studinger (2009), Antarctic crustal thickness from satellite gravity: Implications for the Transantarctic and Gamburtsev Subglacial Mountains, *Earth Planet. Sci. Lett.*, *288*, 194-203, doi: 10.1016/j.epsl.2009.09.022.

Boger, S. D. (2011), Antarctica - Before and after Gondwana, *Precam. Res.*, *19*, 335-371, doi: 10.1016/j.gr.2010.09.003.

Boger, S. D., and C. J. L. Wilson (2003), Brittle faulting in the Prince Charles Mountains, East Antarctica: Cretaceous transtensional tectonics related to the break-up of Gondwana, *Tectonophysics*, *367*, 173-186, doi: 10.1016/S0040-1951(03)00125-2.

Boger, S. D., C. J. L. Wilson, and C. M. Fanning (2001), Early Paleozoic tectonism within the East Antarctic craton: The final suture between east and west Gondwana?, *Geology*, *29*(5), 463-466, doi: 10.1130/0091-7613(2001)029<0463:EPTWTE>2.0.CO;2.

Cande, S. C., J. M. Stock, R. D. Muller, and T. Ishihara (2000), Cenozoic motion between East and West Antarctica, *Nature*, *404*(145-150).

Chaput, J. A., R. C. Aster, A. Nyblade, D. A. Wiens, A. D. Huerta, and T. J. Wilson (2011), Receiver functions on ice: Crust and upper mantle exploration of the POLENET array, in *11th International Symposium on Antarctic Earth Sciences*, edited, p. PO15.12, Edinburgh.

Cooper, A. K., and F. J. Davey (1985), Episodic rifting of Phanerozoic rocks in the Victoria Land Basin, western Ross Sea, Antarctica, *Science*, *229*(4718), 1085-1087.

Corr, H. F. J., and D. G. Vaughan (2008), A recent volcanic eruption beneath the West Antarctic Ice Sheet, *Nature Geosc.*, *1*, 122-125, doi: 10.1038/ngeo106.

Dalziel, I. W. D. (1991), Pacific margins of Laurentia and East Antarctica - Australia as a conjugate rift pair: Evidence and implications for an Eocambrian supercontinent, *Geology*, *19*, 598-601.

Dalziel, I. W. D., and D. H. Elliot (1982), West Antarctica: Problem child of Gondwanaland, *Tectonics*, *1*(1), 3-19.

Dalziel, I. W. D., and L. A. Lawver (2001), The lithospheric setting of the West Antarctic Ice Sheet, in *The West Antarctic Ice Sheet: Behavior and Environment*, edited, pp. 29-44.

Danesi, S., and A. Morelli (2000), Group velocity of Rayleigh waves in the Antarctic region, *Phys. Earth Planet. Int.*, *122*, 55-66, doi: 10.1016/S0031-9201(00)00186-2

Danesi, S., and A. Morelli (2001), Structure of the upper mantle under the Antarctic Plate from surface wave tomography, *Geophys. Res. Lett.*, *28*(23), 4395-4398.

Davey, F. J., and G. Brancolini (1995), The late Mesozoic and Cenozoic structural setting of the Ross Sea region, *Antarctic Research Series*, *68*, 167-182.

Davey, F. J., S. C. Cande, and J. M. Stock (2006), Extension in the western Ross Sea region-links between Adare Basin and Victoria Land Basin, *Geophys. Res. Lett.*, *33*, doi: 10.1029/2006GL027383.

DiVenere, V. J., D. V. Kent, and I. W. D. Dalziel (1994), Mid-Cretaceous paleomagnetic results from Marie Byrd Land, West Antarctica: A test of post-100 Ma relative motion between East and West Antarctica, *J. Geophys. Res*, *99*(B8), 15,115-115,139.

Dziewonski, A. M., and D. L. Anderson (1981), Preliminary reference Earth model, *Phys. Earth Planet. Int.*, *25*, 297-356.

Elliot, D. H. (1975), Tectonics of Antarctica: A Review, *Am. J. Sci.*, *275*(A), 45-106.

Ferraccioli, F., E. Bozzo, and D. Damaske (2002), Aeromagnetic signatures over western Marie Byrd Land provide insight into magmatic arc basement, mafic magmatism and structure of the Eastern Ross Sea Rift flank, *Tectonophysics*, *347*, 139-165.

Ferraccioli, F., E. Armadillo, T. Jordan, E. Bozzo, and H. Corr (2009), Aeromagnetic exploration over the East Antarctic Ice Sheet: A new view of the Wilkes Subglacial Basin, *Tectonophysics*, *478*, 62-77, doi: 10.1016/j.tecto.2009.03.013.

Finotello, M., A. Nyblade, J. Julia`, D. A. Wiens, and S. Anandakrishnan (2011), Crustal V_p-V_s ratios and thickness for Ross Island and the Transantarctic Mountain front, Antarctica, *Geophys. J. Int.*, *185*, 85-92, doi: 10.1111/j.1365-246X.2011.04946.x.

Fitzsimons, I. C. W. (2000a), Grenville-age basement provinces in East Antarctica: Evidence for three separate collisional orogens, *Geology*, *28*(10), 879-882, doi: 10.1130/0091-7613(2000)28<879:GBPIEA>2.0.CO;2.

Fitzsimons, I. C. W. (2000b), A review of tectonic events in the East Antarctic Shield and their implications for Gondwana and earlier supercontinents, *J. African Earth Sciences*, *31*(1), 3-23.

Fitzsimons, I. C. W. (2003), Proterozoic basement provinces in southern and southwestern Australia, and their correlation with Antarctica, in *Proterozoic East Gondwana: Supercontinent Assembly and Breakup*, edited by M. Yoshida, B. F. Windley and S. Dasgupta, pp. 93-130, Geological Society, London, Special Publication, London.

Forsyth, D. W., and A. Li (2005), Array analysis of two-dimensional variations in surface wave phase velocity and azimuthal anisotropy in the presence of multipathing interference, in *Seismic Earth: Array Analysis of Broadband Seismograms*, edited by A. Levander and G. Nolet, pp. 81-97, AGU, Washington D.C.

Goodge, J. W., and C. A. Finn (2010), Glimpses of East Antarctica: Aeromagnetic and satellite magnetic view from the central Transantarctic Mountains of East Antarctica, *J. Geophys. Res*, *115*, doi: 10.1029/2009JB006890.

Goodge, J. W., and C. M. Fanning (2010), Composition and age of the East Antarctic Shield in eastern Wilkes Land determined by proxy of Oligocene-Pleistocene glaciomarine sediment and Beacon Supergroup sandstones, Antarctica, *GSA Bull.*, *122*, 1135-1159, doi: 10.1130/B30079.1.

Goodge, J. W., C. M. Fanning, and V. C. Bennett (2001), U-Pb evidence of ~1.7 Ga crustal tectonism during the Nimrod Orogeny in the Transantarctic Mountains, Antarctica: Implications for Proterozoic plate reconstructions, *Precam. Res.*, *112*, 261-288.

Goodge, J. W., C. M. Fanning, D. M. Brecke, K. J. Licht, and E. F. Palmer (2010), Continuation of the Laurentian Grenville Province across the Ross Sea Margin of East Antarctica, *J. Geol.*, *118*(6), 601-619, doi: 10.1086/656385.

Goodge, J. W., J. D. Veervoort, C. M. Fanning, D. M. Brecke, G. L. Farmer, I. S. Williams, P. M. Myrow, and D. J. DePaolo (2008), A positive test of East Antarctica - Laurentia juxtaposition within the Rodinia supercontinent, *Science*, *321*, 235-240, doi: 10.1126/science.1159189.

Grunow, A. M., D. V. Kent, and I. W. D. Dalziel (1991), New paleomagnetic data from Thurston Island: Implications for the tectonics of West Antarctica and Weddell Sea opening, *J. Geophys. Res.*, *96*(B11), 17935-17954.

Hansen, S. E., J. Julia`, A. A. Nyblade, M. L. Pyle, D. A. Wiens, and S. Anandakrishnan (2009), Using S wave receiver functions to estimate crustal structure beneath ice

sheets: An application to the Transantarctic Mountains and East Antarctic craton, *Geochem. Geophys. Geosyst.*, *10*(8), doi: 10.1029/2009GC002576.

Hansen, S. E., A. A. Nyblade, D. S. Heeszel, D. A. Wiens, P. J. Shore, and M. Kanao (2010), Crustal structure of the Gamburtsev Mountains, East Antarctica, from S-wave receiver functions and Rayleigh wave phase velocities, *Earth Planet. Sci. Lett.*, *300*, 395-401, doi: 10.1016/j.epsl.2010.10.022.

Herrmann, R. B., and C. J. Ammon (2004), Computer Programs in Seismology: Surface Waves, Reciever Functions and Crustal Structure, edited, St. Louis Univ., St. Louis, MO.

Hofmann, J. (1991), Fault tectonics and magmatic ages in the Jetty Oasis area, Mac. Robertson Land: a contribution to the Lambert rift development, in *Geological Evolution of Antarctica*, edited by M. R. A. Thomson, J. A. Crame and J. W. Thomson, pp. 107-112, Cambridge University Press, Cambridge, United Kingdom.

Hole, M. J., and W. E. LeMasurier (1994), Tectonic controls on the geochemical composition of Cenozoic, mafic alkaline volcanic rocks from West Antarctica, *Contib. Mineral. and Petrol.*, *117*, 187-202.

Huerta, A. D., and D. L. Harry (2007), The transition from diffuse to focused extension: Modeled evolution of the West Antarctic Rift system, *Earth Planet. Sci. Lett.*, *255*, 133-147, doi: 10/1016/j.epsl.2006.12.011.

Jankowski, E. J., and D. J. Drewry (1981), The structure of West Antarctica from geophysical studies, *Nature*, *291*, 17-21, doi: 10.1038/291017a0.

Kennett, B. L. N., E. R. Enghdal, and R. Buland (1995), Constraints on seismic velocities in the Earth from travel times, *Geophys. J. Int.*, *122*, 108-124.

Lawrence, J. F., D. A. Wiens, A. A. Nyblade, S. Anandakrishnan, P. J. Shore, and D. Voigt (2006a), Upper mantle thermal variations beneath the Transantarctic Mountains inferred from teleseismic S-wave attenuation, *Geophys. Res. Lett.*, *33*, doi: 10.1029/2005GL024516.

Lawrence, J. F., D. A. Wiens, A. A. Nyblade, S. Anandakrishnan, P. J. Shore, and D. Voigt (2006b), Rayleigh wave phase velocity analysis of the Ross Sea, Transantarctic Mountains, and East Antarctica from a temporary seismograph array, *J. Geophys. Res.*, *111*, doi: 10.1029/2005JB003812.

Lawrence, J. F., D. A. Wiens, A. A. Nyblade, S. Anandakrishnan, P. J. Shore, and D. Voigt (2006c), Crust and upper mantle structure of the Transantarctic Mountains and surrounding regions from receiver functions, surface waves, and gravity: Implications for uplift models, *Geochem. Geophys. Geosys.*, *7*(10), doi: 10.1029/2006GC001282.

LeMasurier, W. E., and C. A. Landis (1996), Mantle-plume activity recorded by low-relief erosion surfaces in West Antarctica and New Zealand, *GSA Bull.*, *108*, 1450-1466, doi: 10.1130/0016-7606(1996)108<1450:MPARBL>2.3.CO;2.

Li, A., D. W. Forsyth, and K. M. Fischer (2002), Evidence for shallow isostatic compensation of the southern Rocky Mountains from Rayleigh wave tomography, *Geology*, *30*(8), 683-686.

Li, A., D. W. Forsyth, and K. M. Fischer (2003), Shear velocity structure and azimuthal anisotropy beneath eastern North America from Rayleigh wave inversion, *J. Geophys. Res*, *108*(B8), doi: 10.1029/2002JB002259.

Lisker, F., R. Brown, and D. Fabel (2003), Denudational and thermal history along a transect across the Lambert Graben, northern Prince Charles Mountains, Antarctica, derived from apatite fission track thermochronology, *Tectonics*, *22*(5), doi: 10.1029/2002TC001477.

Luyendyk, B. P., D. S. Wilson, and C. S. Siddoway (2003), Eastern margin of the Ross Sea Rift in western Marie Byrd Land, Antarctica: Crustal structure and tectonic development, *Geochem. Geophys. Geosys.*, *4*(10), doi: 10.1029/2002GC000462.

Lythe, M. B., D. G. Vaughan, and t. B. Consortium (2001), BEDMAP: A new ice thickness and subglacial topographic model of Antarctica, *J. Geophys. Res*, *106*(B6), 11335-11351.

Mooney, W. D., G. Laske, and T. G. Masters (1998), Crust 5.1: A global crustal model at 5 x 5, *J. Geophys. Res*, *103*(B1), 727-747.

Moores, E. M. (1991), Southwest U.S. - East Antarctic (SWEAT) connection: A hypothesis, *Geology*, *19*, 425-428.

Morelli, A., and S. Danesi (2004), Seismological imaging of the Antarctic continental lithosphere: a review, *Global and Planetary Change*, *42*, 155-165, doi: 10.1016/j.gloplacha.2003.12.005.

Panter, K. S., P. R. Kyle, and J. L. Smellie (1997), Petrogenesis of a phonolite - trachyte succession at Mount Sidley, Marie Byrd Land, Antarctica, *J. Petrology*, *38*(9), 1225-1253.

Paulson, T. S., and T. J. Wilson (2010), Evolution of Neogene volcanism and stress patterns in the glaciated West Antarctic Rift, Marie Byrd Land, Antarctica, *J. Geol. Soc., Lon.*, *167*, 401-416, doi: 10.1144/0016-76492009-044.

Pyle, M. L., D. A. Wiens, A. A. Nyblade, and S. Anandakrishnan (2010), Crustal structure of the Transantarctic Mountains near the Ross Sea from ambient seismic noise tomography, *J. Geophys. Res*, *115*, B11310, doi: 10.1029/2009JB007081.

Reading, A. M. (2006), The seismic structure of Precambrian and early Palaeozoic terranes in the Lambert Glacier region, East Antarctica, *Earth Planet. Sci. Lett.*, *244*, 44-57, doi: 10.1016/j.epsl.2006.01.031.

Ritzwoller, M. H., N. M. Shapiro, A. L. Levshin, and G. M. Leahy (2001), Crustal and upper mantle structure beneath Antarctica and surrounding oceans, *J. Geophys. Res*, *106*(12), 30645-30670.

Roult, G., and D. Rouland (1992), Antarctica I: deep structure investicagions inferred from seismology: a review, *Phys. Earth Planet. Int.*, *84*, 15-32.

Shapiro, N. M., and M. H. Ritzwoller (2002), Monte-Carlo inversion for a global shear-velocity model of the crust and upper mantle, *Geophys. J. Int.*, *151*, 88-105.

Siddoway, C. S., S. L. Baldwin, P. G. Fitzgerald, C. M. Fanning, and B. P. Luyendyk (2004), Ross Sea mylonites and the timing of intracontinental extension within the West Antarctic rift system, *Geology*, *32*(1), 57-60, doi: 10.1130/G20005.1.

Sieminski, A., E. Debayle, and J.-J. Le¤ve“que (2003), Seismic evidence for deep low-velocity anomalies in the transition zone beneath West Antarctica, *Earth Planet. Sci. Lett.*, *216*, 645-661, doi: 10.1016/S0012-821X(03)00518-1.

Stern, T. A., and U. S. ten Brink (1989), Flexural uplift of the Tranantarctic Mountains, *J. Geophys. Res*, *94*(B8), 10,315-310,330.

Studinger, M., R. E. Bell, W. R. Buck, G. D. Karner, and D. D. Blankenship (2004), Sub-ice geology inland of the Transantarctic Mountains in light of new aerogeophysical data, *Earth Planet. Sci. Lett.*, *220*, 391-408, doi: 10.1016/S0012-821X(04)00066-4.

Studinger, M., G. D. Karner, R. E. Bell, V. Levin, C. A. Raymond, and A. A. Tikku (2003), Geophysical models for the tectonic framework of the Lake Vostok region, East Antarctica, *Earth Planet. Sci. Lett.*, *216*, 663-677, doi: 10.1016/S0012-821X(03)00548-X.

ten Brink, U. S., and T. A. Stern (1992), Rift flank uplifts and hinterland basins: Comparisons of the Transantarctic Mountains with the Great Escarpment of Southern Africa, *J. Geophys. Res*, *97*(B1), 569-585.

ten Brink, U. S., S. Bannister, B. C. Beaudoin, and T. A. Stern (1993), Geophysical investigations of the tectonic boundary between East and West Antarctica, *Science*, *261*, 45-50.

van de Flierdt, T., S. R. Hemming, S. L. Goldstein, G. E. Gehrels, and S. E. Cox (2008), Evidence against a young volcanic origin of the Gamburtsev Subglacial Mountains, Antarctica, *Geophys. Res. Lett.*, *35*, doi: 10.1029/2008GL035564.

von Frese, R. R. B., L. Tan, J. W. Kim, and C. R. Bently (1999), Antarctic crustal modeling from the spectral correlation of free-air gravity anomalies with the terrain, *J. Geophys. Res*, *104*(B11), 25,275-225,296.

Watson, T., A. Nyblade, D. A. Wiens, S. Anandakrishnan, M. Benoit, P. J. Shore, D. Voigt, and J. VanDecar (2006), P and S velocity structure of the upper mantle beneath the Transantarctic Mountains, East Antarctic craton, and Ross Sea from travel time tomography, *Geochem. Geophys. Geosys.*, *7*(7), doi: 10.1029/2005GC001238.

Weaver, S. D., B. C. Storey, R. J. Pankhurst, S. B. Mukasa, V. J. DiVenere, and J. D. Bradshaw (1994), Antarctica - New Zealand rifting and Marie Byrd Land lithospheric magmatism linked to ridge subduction and mantle plume activity, *Geology*, *22*, 811-814.

Weeraratne, D. S., D. W. Forsyth, K. M. Fischer, and A. A. Nyblade (2003), Evidence for an upper mantle plume beneath the Tanzanian craton from Rayleigh wave tomography, *J. Geophys. Res*, *108*(B9), doi: 10.1029/2002JB002273.

Wessel, P., and W. H. F. Smith (1998), New, improved version of Generic Mapping Tools released, *Eos. Trans. AGU*, *79*(47).

West, M., J. Ni, W. S. Baldridge, D. Wilson, R. Aster, W. Gao, and S. Grand (2004), Crust and upper mantle shear wave structure of the southwest United States: Implications for rifting and support for high elevation, *J. Geophys. Res*, *109*, doi: 10.1029/2003JB002575.

Wilson, D., R. Aster, M. West, J. Ni, S. Grand, W. Gao, W. S. Baldridge, S. Semken, and P. Patel (2005), Lithospheric structure of the Rio Grande rift, *Nature*, *433*, 851-855.

Wilson, D. S., and B. P. Luyendyk (2006), Bedrock platforms within the Ross Embayment, West Antarctica: Hypotheses for ice sheet history, wave erosion, Cenozoic extension, and thermal subsidence,, *Geochem. Geophys. Geosys.*, *7*(12), Q12011, doi: 10.1029/2006GC001294.

Wilson, D. S., and B. P. Luyendyk (2009), West Antarctic paleotopography estimated at the Eocene-Oligocene climate transition, *Geophys. Res. Lett.*, *36*, doi: 10.1029/2009GL039297.

Wilson, T. J. (1995), cenozoic transtension along the Transantarctic Mountains - West Antarctic Rift boundary, southern Victoria Land, Antarctica, *Tectonics*, *14*(2), 531-545.

Winberry, J. P., and S. Anandakrishnan (2003), Seismicity and neotectonics of West Antarctica, *Geophys. Res. Lett.*, *30*(18).

Winberry, J. P., and S. Anandakrishnan (2004), Crustal structure of the West Antarctic rift system and Marie Byrd Land hotspot, *Geology*, *32*(11), 977-980, doi: 10.1130/G20768.1.

Yang, Y., and D. W. Forsyth (2006), Regional tomographic inversion of the amplitude and phase of Rayleigh waves with 2-D sensitivity kernels, *Geophys. J. Int.*, *166*, 1148-1160, doi: 10.1111/j.1365-246X.2006.02972.x.

Yang, Y., and M. H. Ritzwoller (2008), Teleseismic surface wave tomography in the western U.S. using the Transportable Array component of USArray, *Geophys. Res. Lett.*, *35*, doi: 10.1029/2007GL032278.

Yang, Y., A. Li, and M. H. Ritzwoller (2008a), Crustal and uppermost mantle structure in southern Africa revealed from ambien noise and teleseismic tomography, *Geophys. J. Int.*, *174*, 235-248, doi: 10.1111/j.1365-246X.2008.03779.x.

Yang, Y., M. H. Ritzwoller, F.-C. Lin, M. P. Moschetti, and N. M. Shapiro (2008b), Structure of the crust and uppermost mantle beneath the western United States revealed by ambient noise and earthquake tomography, *J. Geophys. Res*, *113*, doi: 10.1029/2008JB005833.

Yuan, H., and B. Romanowicz (2010), Lithospheric layering in the North American craton, *Nature*, *466*, 1063-1068, doi: 10.1038/nature09332.

Zhou, Y., F. A. Dahlen, and G. Nolet (2004), Three-dimensional sensitivity kernels for the surface-wave observables, *Geophys. J. Int.*, *158*, 142-168, doi: 10.1111/j.1365-246X.2004.02324.x.

Table 5.1: Station names and locations for the TAMSEIS deployment. [1]Permanent GSN stations.

Station Name	Latitude	Longitude
ARHT	-77.84	166.66
CASE	-80.44	160.1
CBOB	-77.03	163.17
CBRI	-77.25	166.43
CCRZ	-77.52	169.09
CPHI	-75.07	162.65
CTEA	-78.94	160.76
DIHI	-79.85	159.48
E000	-77.63	163.62
E002	-77.58	163.01
E004	-77.41	162.07
E006	-77.37	161.63
E008	-77.28	160.56
E010	-77.18	160.09
E012	-77.05	159.33
E014	-76.99	158.62
E018	-76.82	157.22
E020	-76.73	156.55
E022	-76.63	155.9
E024	-76.54	155.24
E026	-76.42	154.76
E028	-76.31	154.04
E030	-76.25	153.38
JNCT	-76.93	157.9
MAGL	-76.14	162.41
MCMD	-77.85	166.67
MINN	-78.55	166.88
N000	-76.01	160.38
N020	-77.47	155.82
N028	-78.03	153.65
N036	-78.55	151.28
N044	-79.07	148.62
N052	-79.54	145.75
N060	-80	142.59
N068	-80.39	138.92
N076	-80.81	135.43
N084	-81.16	131.47
N092	-81.46	126.98
N100	-81.65	122.61
N108	-81.88	117.61
N116	-82.01	112.57
N124	-82.07	107.64
N132	-82.08	101.96
RIS0	-78.08	172.5
TIMW	-80.39	135.27
VNDA[1]	-77.52	161.85
SBA[1]	-77.85	166.76

Table 5.2: Station names and location for the GAMSEIS experiment. [1]Chinese deployed seismic stations operate only during the austral summer. [2]Stations operated by the National Institute of Polar Research in Japan.

Station Name	Latitude	Longitude
N124	-82.07	107.64
N132	-82.08	101.95
N140	-82.01	96.77
N148	-81.86	91.51
N156	-81.67	86.50
N165	-81.41	81.76
N173	-81.11	77.47
N182	-80.74	73.19
N190	-80.33	69.43
N198	-79.86	65.96
N206	-79.39	62.86
N215	-78.90	59.99
P061	-84.50	77.22
P071	-83.65	77.33
P080	-82.81	77.36
P090	-81.94	77.31
P116	-79.57	77.05
P124	-78.87	77.66
GM01	-83.99	104.73
GM02	-79.43	97.58
GM03	-80.22	85.94
GM04	-83.00	61.11
GM05	-81.18	51.16
GM06[2]	-79.33	44.31
GM07[2]	-77.31	39.61
AGO1	-83.86	129.61
EGLE[1]	-76.42	77.03
CHNB[1]	-77.17	76.98

Table 5.3: Station names and locations of seismic stations associated with POLENET project. Stations are broken into POLENET-north and POLENET-south designations based on inclusion in sub-arrays. [1]Gamseis stations included in POLENET-north sub-array. [2]GSN stations.

Station Name	Latitude	Longitude	North/South
N100[1]	-81.65	122.59	North
N124[1]	-82.07	107.64	North
N132[1]	-82.08	101.95	North
N140[1]	-82.01	96.77	North
AGO1[1]	-83.86	129.61	North
BEAR	-74.55	-111.85	South
BYRD	-80.02	-119.47	South
CLRK	-77.32	-141.85	South
DEVL	-81.48	161.97	North
DNTW	-76.46	-107.78	South
DUFK	-82.86	-53.2	South
FALL	-85.31	-143.63	North/South
FISH	-78.93	162.57	North
HOWD	-77.53	-86.77	South
KOLR	-76.15	-120.73	South
LONW	-81.35	152.74	North
MECK	-75.28	-72.18	South
MILR	-83.31	156.25	North
MPAT	-78.03	-155.02	North/South
PECA	-85.61	-68.55	South
SILY	-77.13	-125.97	South
SIPL	-81.64	-148.96	North/South
ST01	-83.23	-98.74	South
ST02	-82.07	-109.12	South
ST03	-81.41	-113.15	South
ST04	-80.72	-116.58	South
ST06	-79.33	-121.82	South
ST07	-78.64	-123.8	South
ST08	-77.95	-125.53	South
ST10	-75.81	-129.75	South
ST13	-77.56	-130.51	South
ST14	-77.84	-134.08	South
SURP	-84.72	-171.2	North/South
UNGL	-79.77	-82.52	South
WAIS	-79.42	-111.78	South
WHIT	-82.68	-104.39	South
WILS	-80.04	-80.56	South
WNDY	-82.37	-119.41	South
VNDA[2]	-77.52	161.85	North
QSPA[2]	-89.93	144.44	North/South
SBA[2]	-77.85	166.76	North

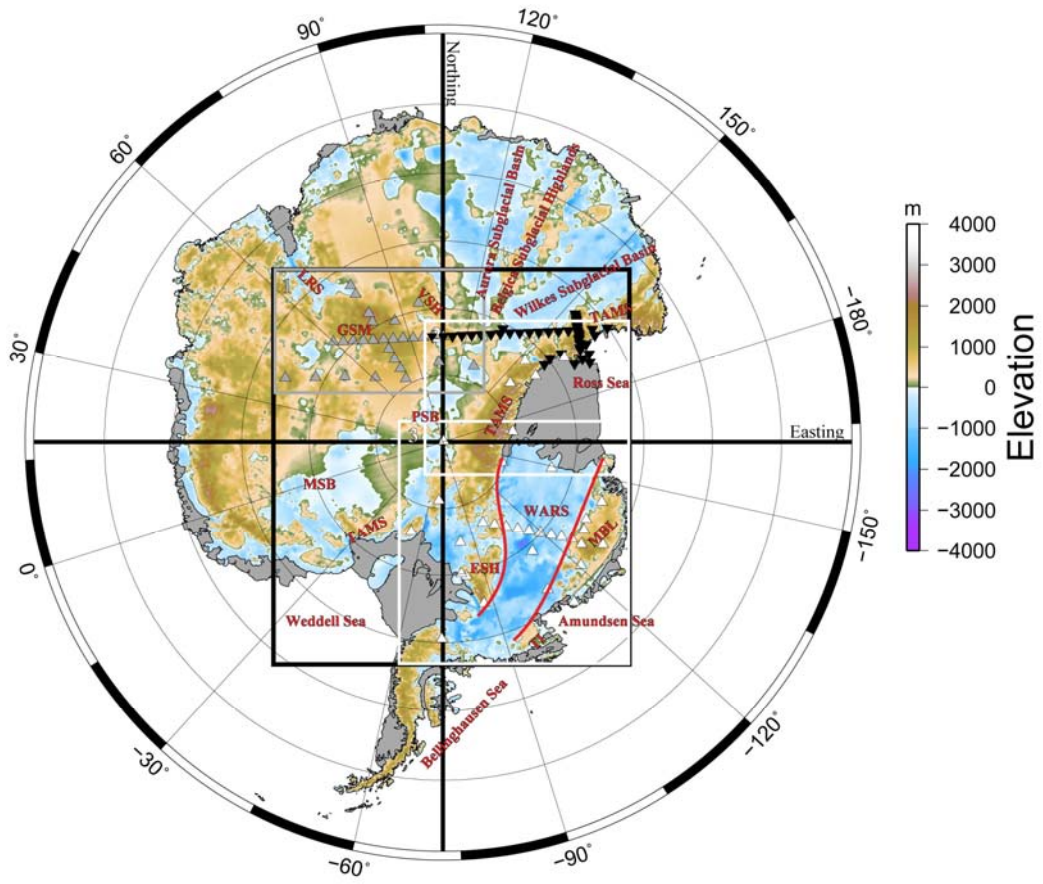

Figure 5.1: Study region and station locations over subglacial bedrock topography [*Lythe et al.*, 2001]. Large black box denotes study region while smaller boxes denote GAMSEIS (1), POLENET-north (2), or POLENET-south (3) subarrays for stations that operated during the same period. See tables 5.1-5.3 for a breakdown of which stations were included in which network processing subsets. Station locations are grey (GAMSEIS), black inverted (TAMSEIS), or white (POLENET) triangles depending on seismic network. Major subglacial features are labeled in red: LRS, GSM, VSH, MSB, PSB, TAMS, ESH, WARS, MBL are Lambert Rift System, Gamburtsev Subglacial Mountains, Vostok Subglacial Highlands, Maud Subglacial Basin, Polar Subglacial Basin, TAMS, Ellsworth Subglacial Highlands, West Antarctic Rift System, and Marie

Byrd Land respectively. Heavy red lines denote boundaries of WARS [*Winberry and Anandakrishnan*, 2003].

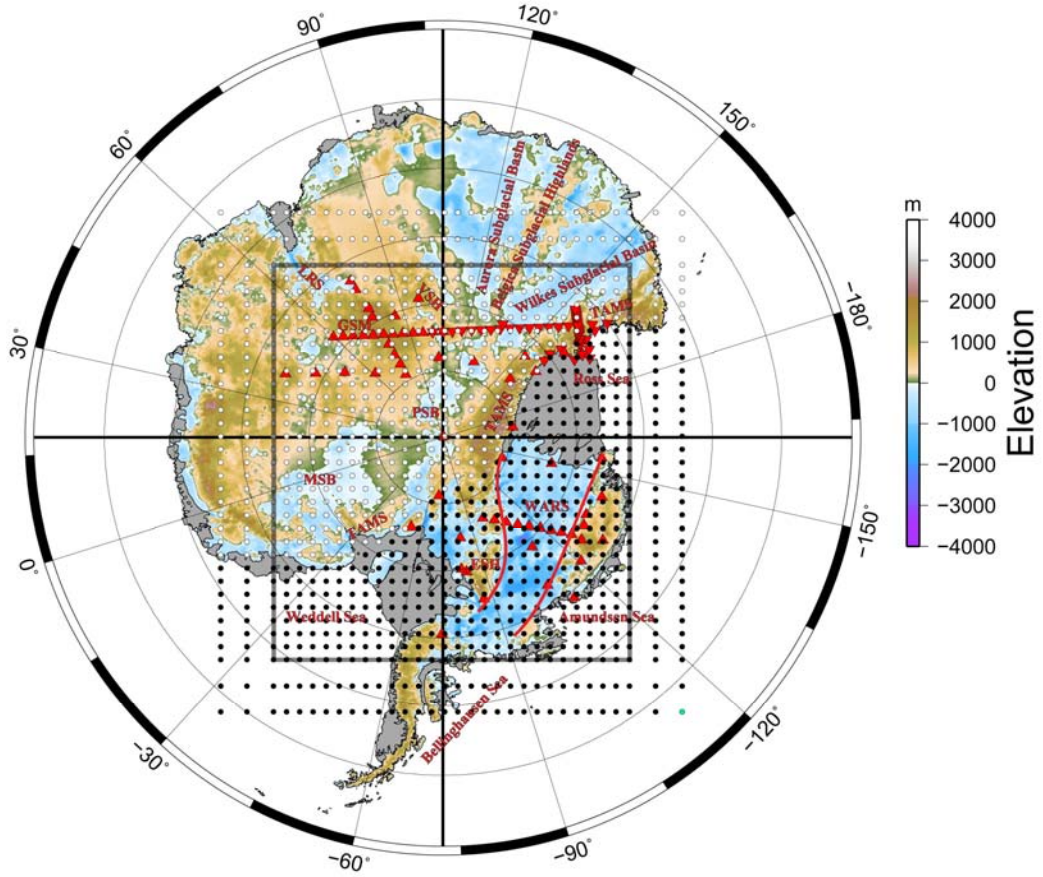

Figure 5.2: Node locations for study. White and black nodes represent East Antarctica and West Antarctica respectively. Labels as in figure 1. Nodes outside heavy black line are designed to absorb effect of structure outside imaged region and are not presented or interpreted in other figures.

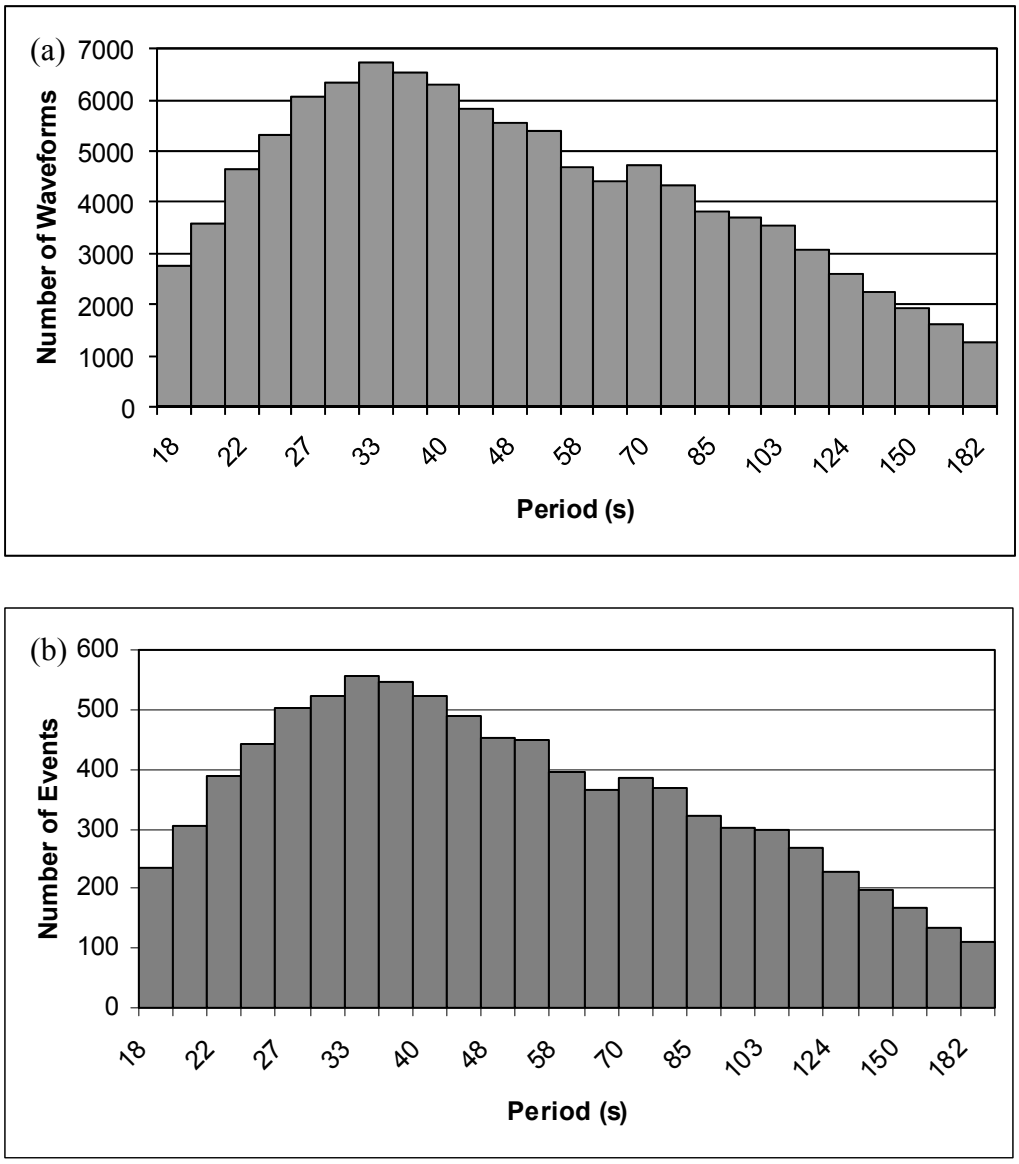

Figure 5.3: Number of waveforms (a) and events (b) used in study. Maximum number of waveforms (6728) and events (527) occurs for period of 33s. There is a subtle secondary peak at 70s indicating that our resolution is greatest at the base of the crust/uppermost mantle.

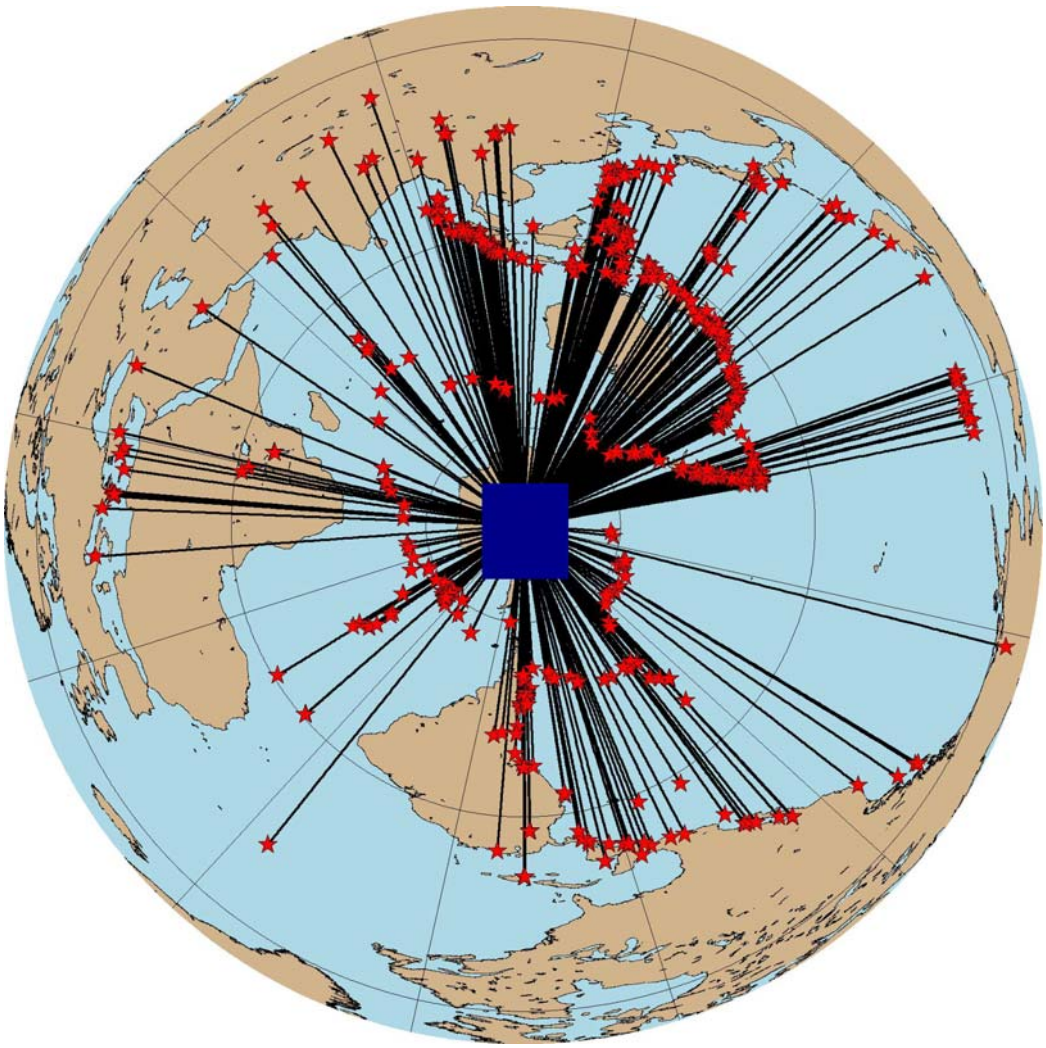

Figure 5.4: Azimuthal Equidistant map of earthquake locations (red stars) used in this study. Great circle paths from earthquake locations to South Pole, near center of study region, are plotted as black lines. Dark blues square is region imaged by this study. Grid spacing in latitude and longitude is 60 degrees and 30 degrees respectively. Map is oriented with the northing direction defined within the inversion grid at top. Earthquakes used in this study come dominantly from the western Pacific subduction zones.

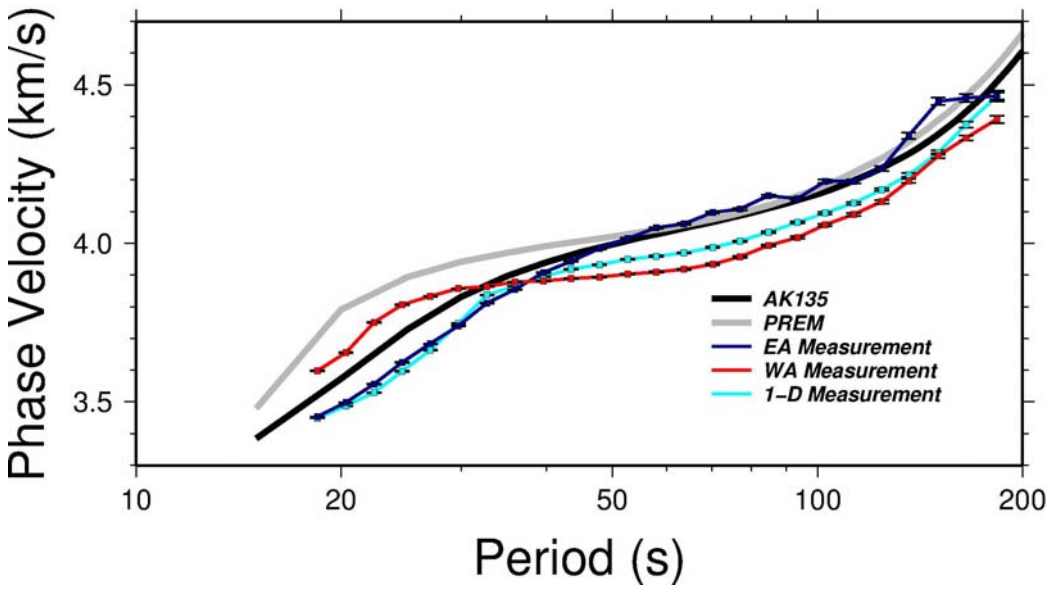

Figure 5.5: 1-D dispersion curves for study region. EA and WA curves correspond to white (East Antarctica) and black (West Antarctica) nodes in figure 2 and the light blue curve is the average phase velocity model across the entire region. Vertical error bars are two standard deviations. Two global models, the global average PREM [*Dziewonski and Anderson*, 1981] and continental average AK135 [*Kennett et al.*, 1995], are plotted for comparison. East Antarctica has a thicker crust than the global continental model (periods<~50s) and a slightly faster mantle (periods>50s). The model for West Antarctica is defined by a crust and upper mantle that is slower than oceanic PREM throughout the period range of this study. The average 1-D model is largely a hybrid of the two regional models with the exception of periods < 27s where it is slower than either regional model.

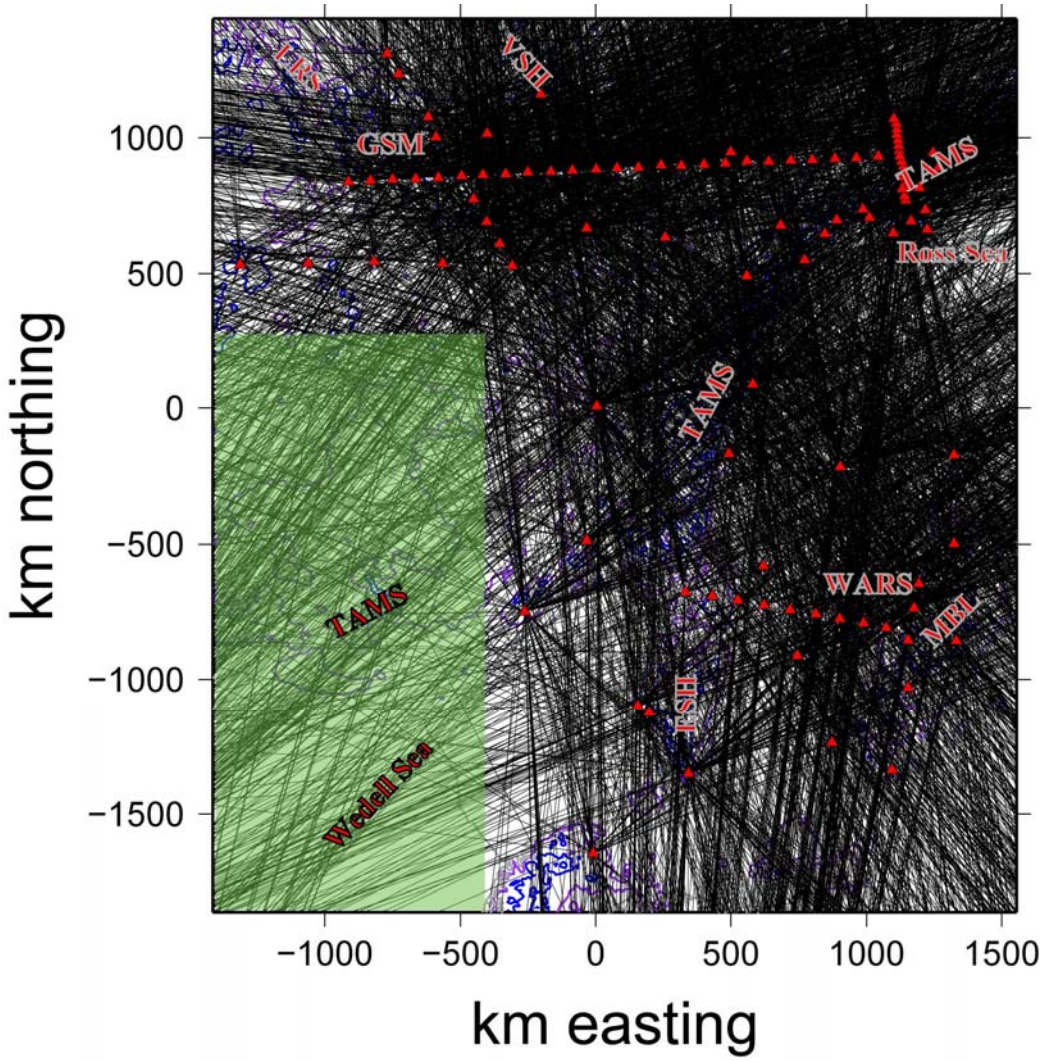

Figure 5.6: Raypath coverage at 33s. Black lines are great circle paths for event-station pairs used in inverting for 2-D phase velocity structure at this period. Red triangles are station locations and labels as in figures 1 and 2. Green square is region masked in phase and shear velocity maps due to lack of raypath and station coverage. Grey lines are coasts and ice shelves, blue lines and violet lines are 1000m and 0m bedrock elevation contours respectively.

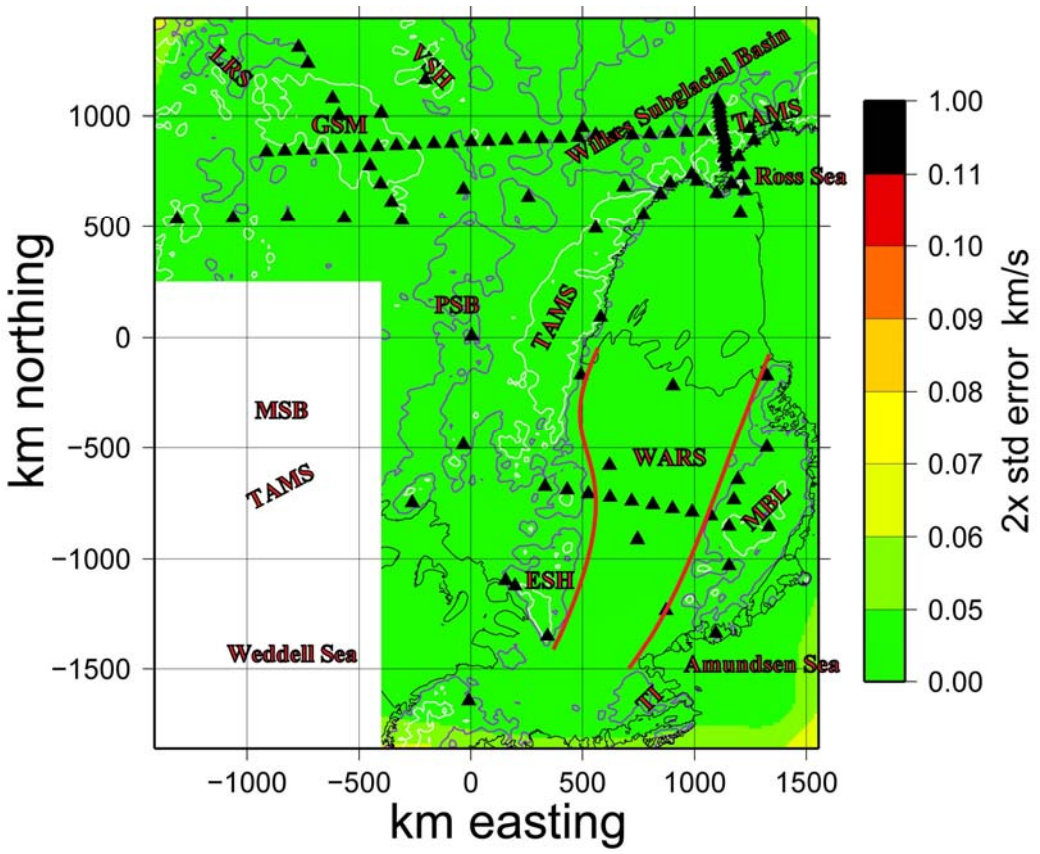

Figure 5.7: *A posteri* standard error plot at 53 seconds period for 2-D phase velocity inversion. Labels as in figure 1, thin black lines are coasts and ice shelves, white and violet lines are 1000m and 0m contours respectively. Blank region in southwest corner is region of limited resolution due to lack of raypaths and stations. Standard error is quite low for the entire study region, less than 0.05 km/s. Geographic plot as in figure 5, note that West Antarctica is located in the lower right corner of mapped region due to the local coordinate system used in inversion.

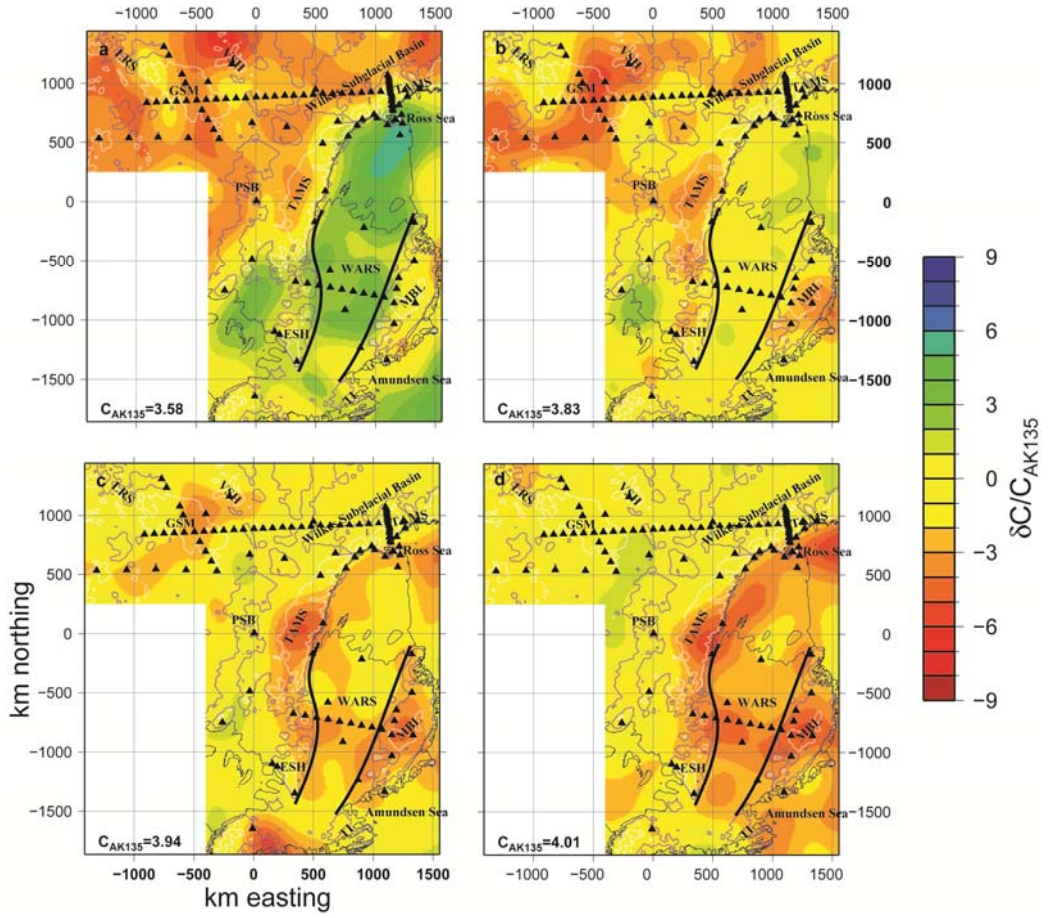

Figure 5.8: Phase velocity maps at (a) 20, (b) 30, (c) 40, and (d) 53 seconds relative to AK135 [*Kennett et al.*, 1995]. Stations are black triangles and labels are same as in other figures. AK135 phase velocities are plotted in lower left corner. West Antarctica transitions from being 2-4% faster than the global average at 20 seconds period (a) to being 2-5% slow at 50 seconds period. Largest slow velocity anomalies are beneath Marie Byrd Land (MBL), the central Transantarctic Mountains (beneath TAMS label in middle of maps) and in the Ross Sea region. The GSM also have slower than average phase velocities at periods less than ~53 seconds.

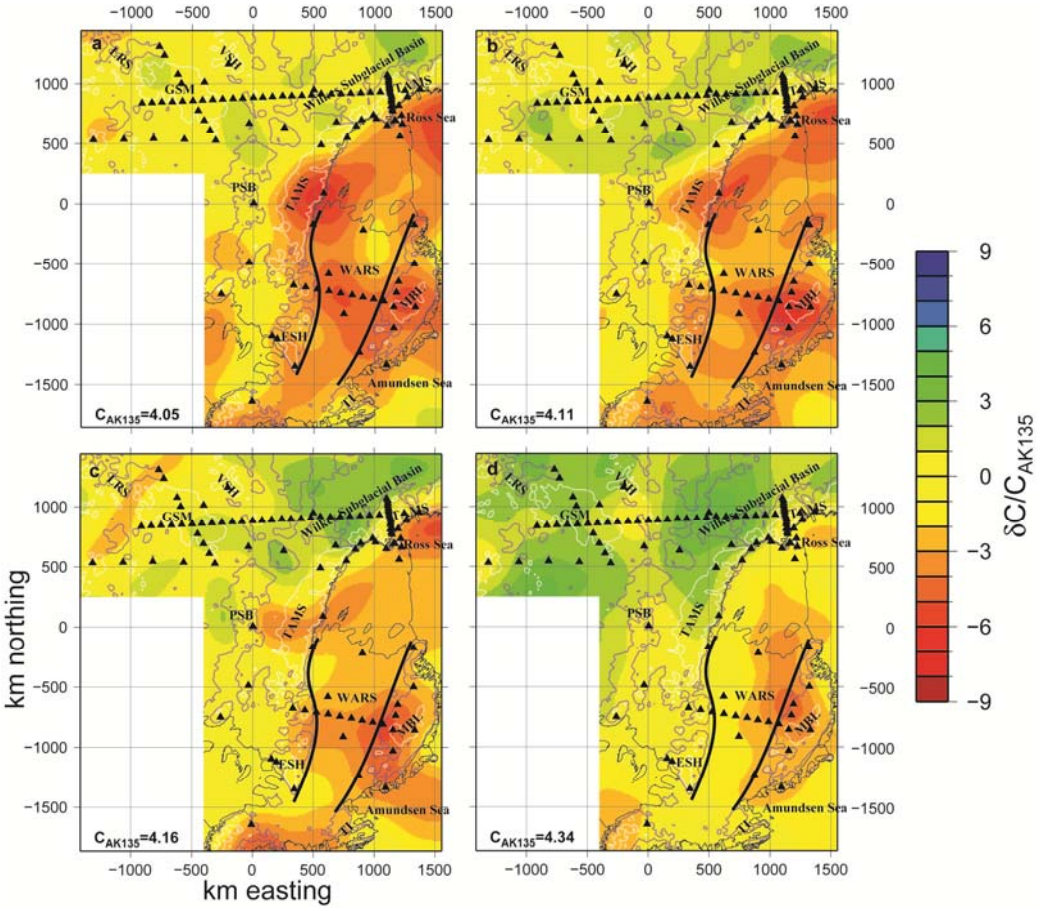

Figure 5.9: Same as figure 8 but at 64 (a), 84 (b), 103 (c), and 150 (d) seconds. Slow phase velocities relative to AK135 mark all periods in West Antarctica. The slow velocity anomaly spreads laterally at periods of 64-103 (a-c) seconds but appears to be concentrated beneath Marie Byrd Land at 150 seconds (d). Phase velocities become increasingly fast relative to the global average within East Antarctica supporting the hypothesis that cold cratonic lithosphere lies beneath the region.

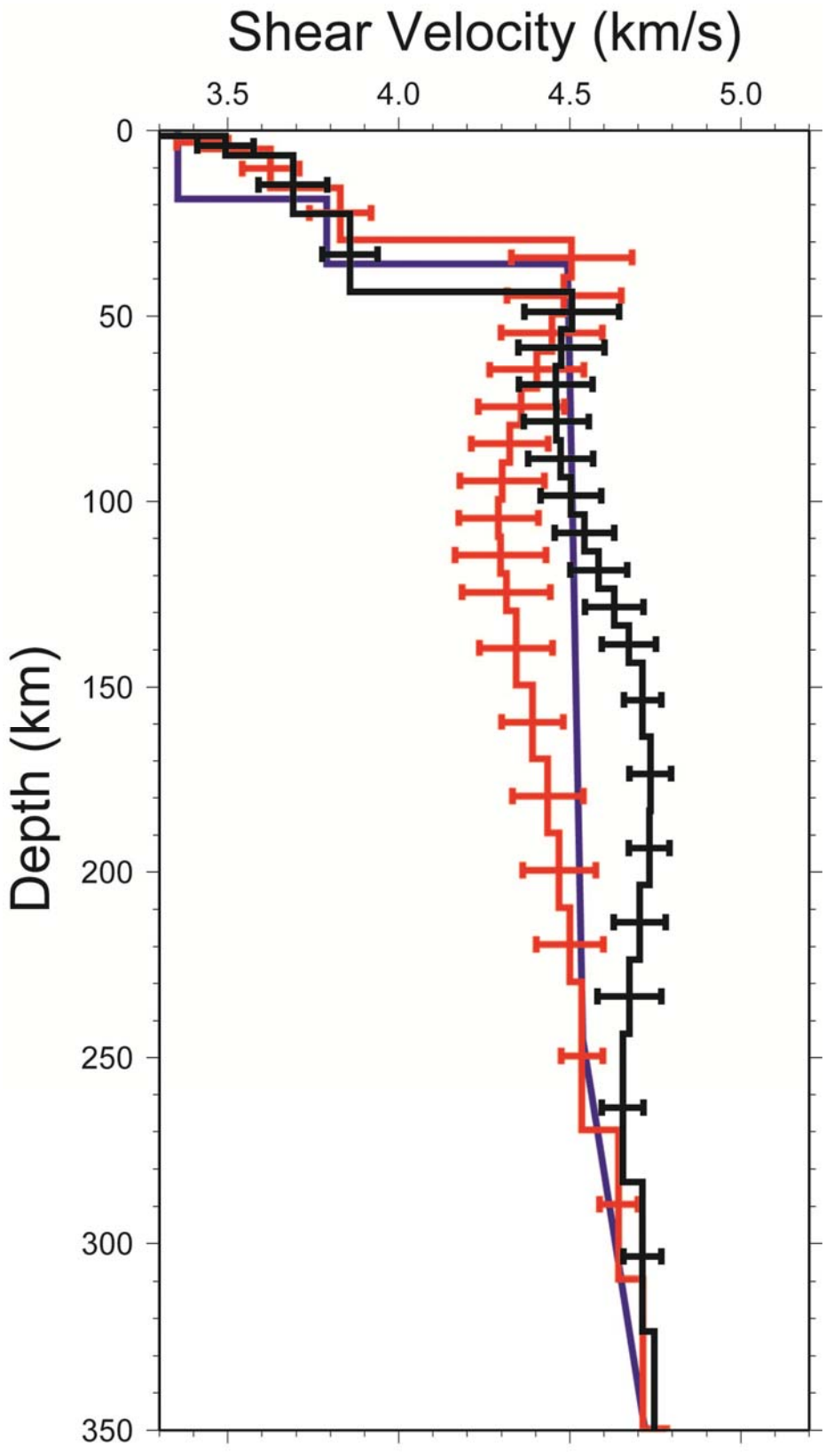
Shear Velocity (km/s)
3.5
4.0
4.5
5.0
0
50
100
150
200
250
300
350
Depth (km)

Figure 5.10: 1-D shear velocity models for East (black) and West (red) Antarctica with AK135 reference model (blue) [*Kennett et al.*, 1995]. Horizontal error bars represent standard deviation of acceptable models generated during Monte Carlo simulation. Upper mantle of West Antarctica is significantly slower than that of AK135at depths of 50-220 km. East Antarctica is faster than the global model from 100 to more than 250 km.

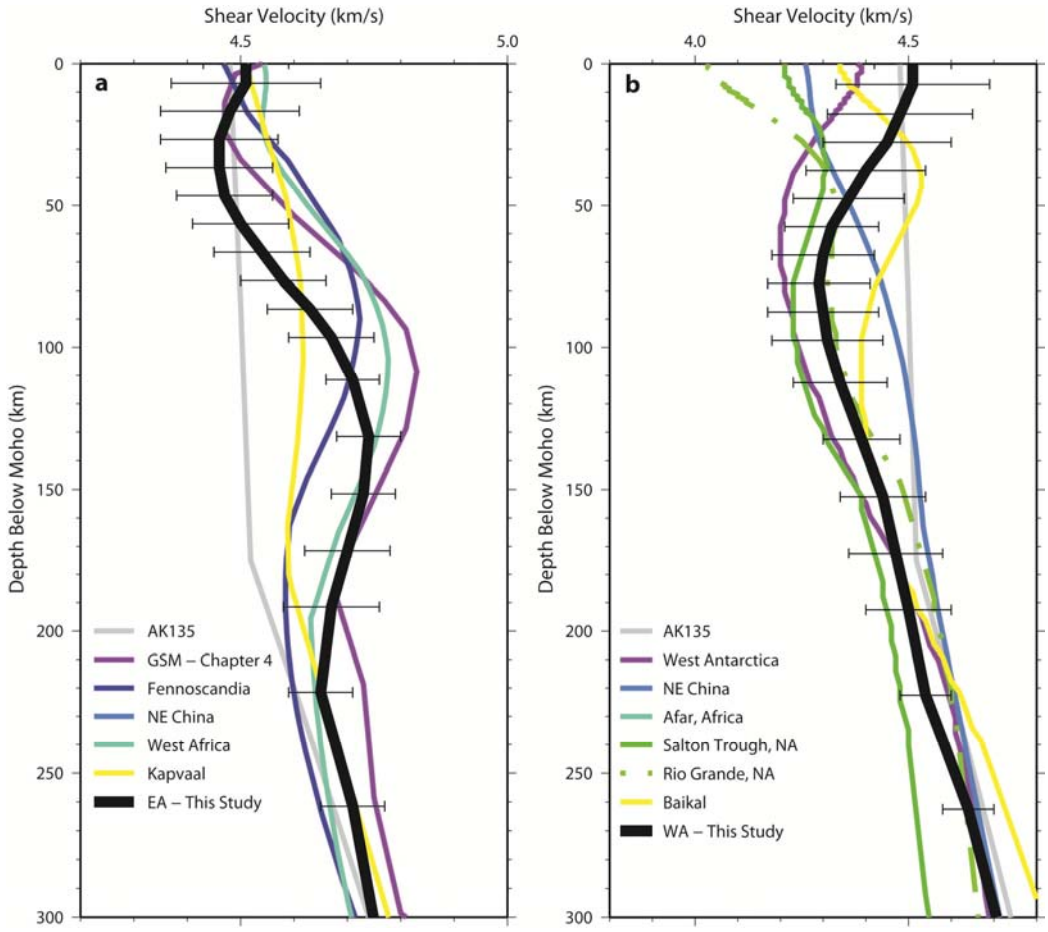

Figure 5.11: Comparison of 1-D shear velocity results for East (a) and West (b) Antarctic mantles with a number of regions around the world with similar tectonic settings. 1-D profiles are extracted from the CUB shear velocity model [*Shapiro and Ritzwoller*, 2002] with the exception of the AK135 [*Kennett et al.*, 1995] and the GSM profile from the Gamburtsev Subglacial Mountains (chapter 4). East Antarctica is similar to other Precambrian cratons such as Fennoscandia and West Africa. West Antarctica is seismically similar to other continental regions that have undergone extension. Horizontal error bars represent range of acceptable models from Monte Carlo modeling.

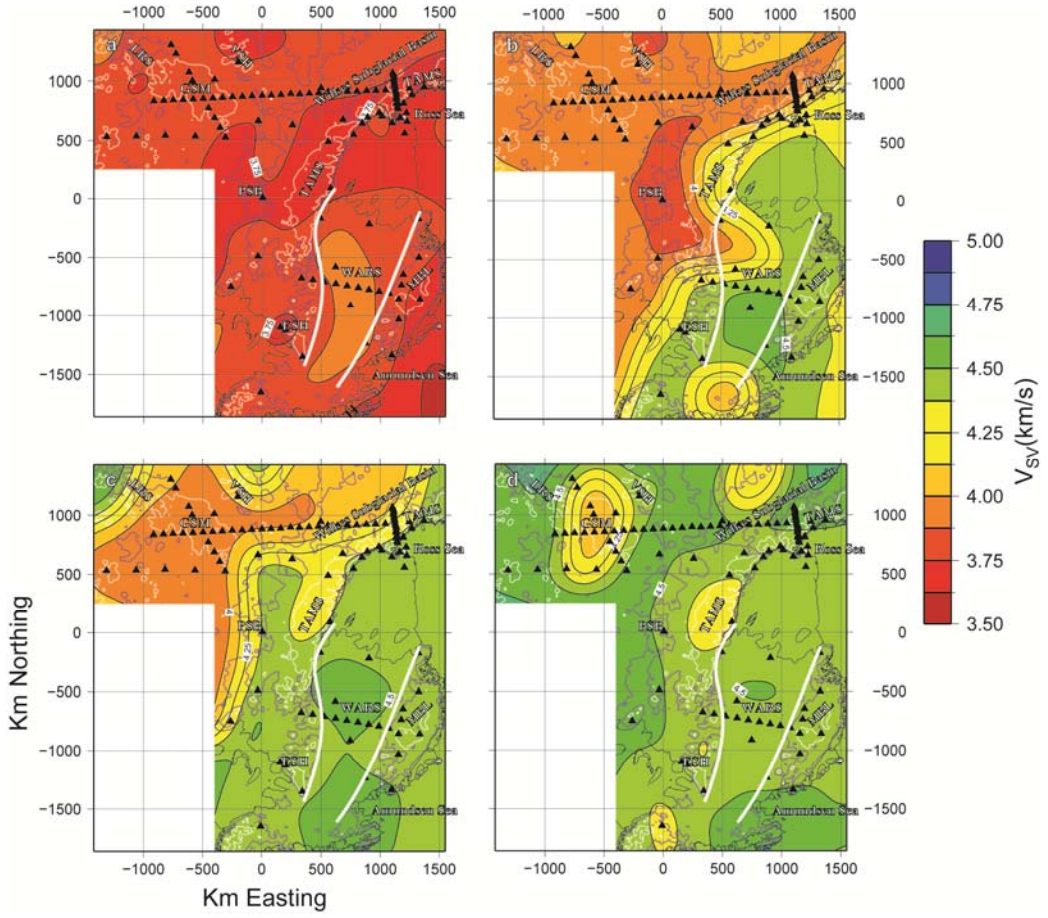

Figure 5.12: Shear velocity maps at depths of 20 (a), 30 (b), 40 (c), and 50 km (d). labels are same as in figure 1. At shallow depths, the WARS is marked by fast, thin crust (a-c). Crustal velocities persist beneath East Antarctica to depths of ~40 km with the exception of the GSM where crustal thicknesses are in excess of 50 km [*Hansen et al.*, 2010]. The central region of the TAMS 0 km – 500 km easting and -100 km – 500 km northing are marked by slow seismic velocities at all depths.

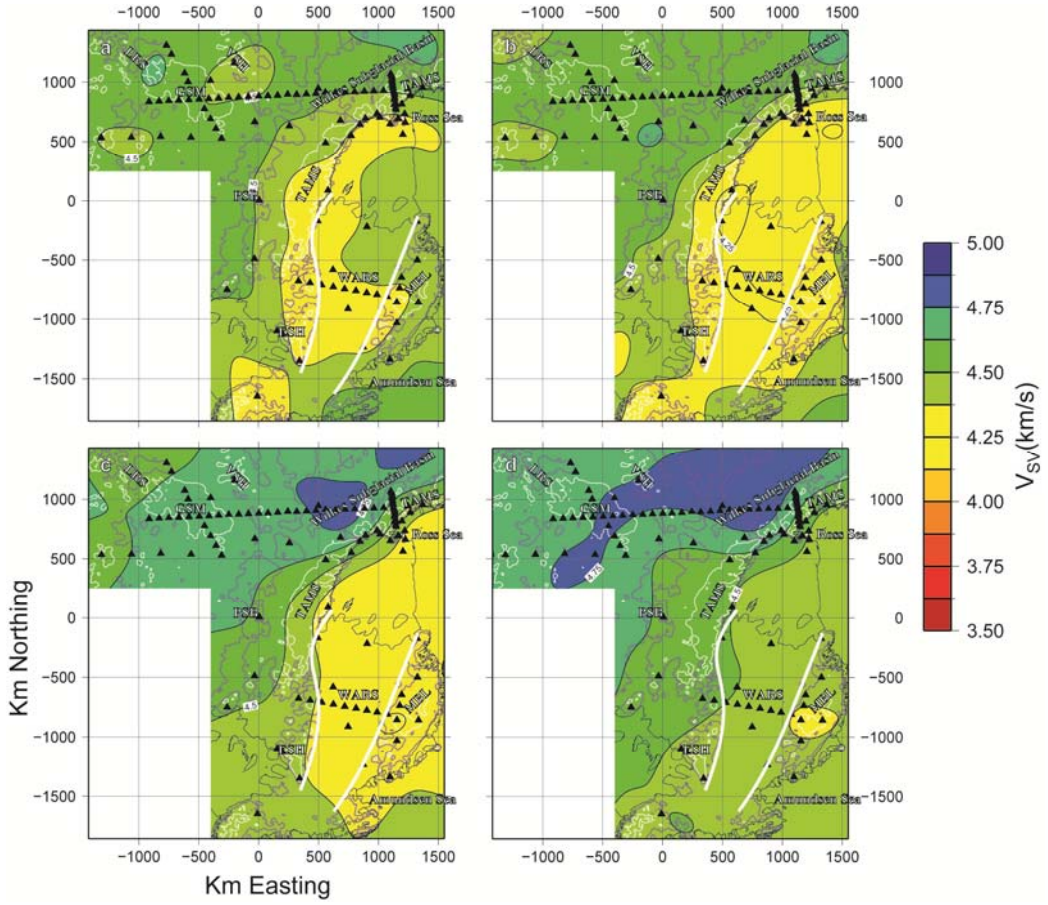

Figure 5.13: Shear velocity maps at depths of 70 (a), 100 (b), 140 (c), and 200 km (d). Labels are same as in figure 1. At these depths there is a marked difference between East and West Antarctica. A slow velocity zone extends across the WARS and hugs the TAMS in West Antarctica at shallower depths (a). The anomaly broadens with depth (b-d). East Antarctica is marked by a broad fast seismic velocity anomaly (c-d) that is consistent with a cratonic regions around the world (figure 11a).

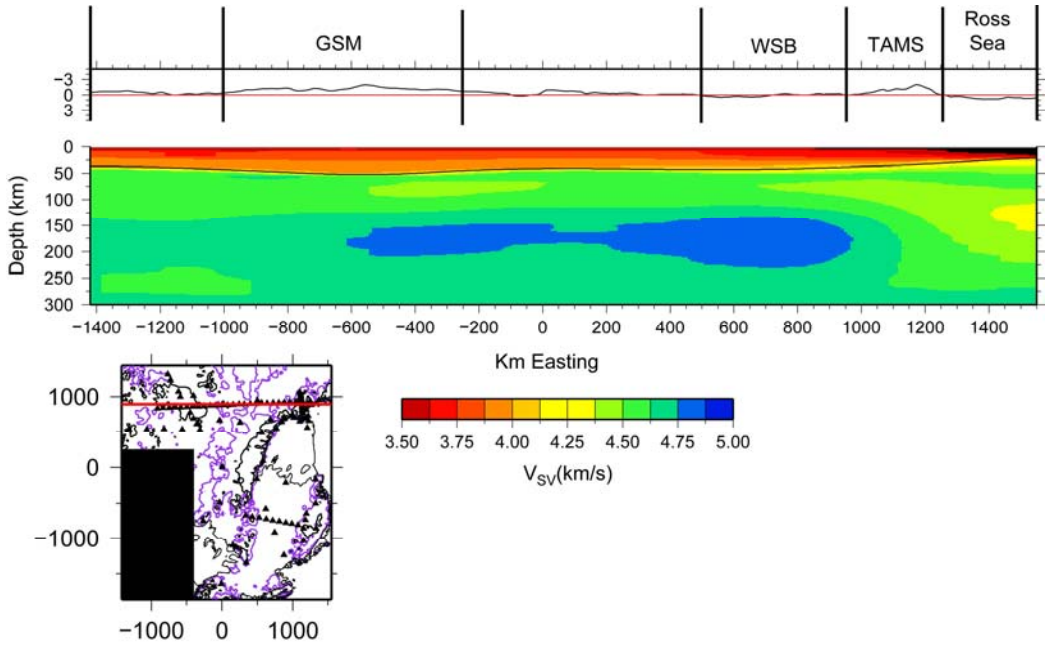

Figure 5.14: Seismic cross section along the 'N-line', a line of continuous seismic stations extending from the Gamburtsev Subglacial Mountains across East Antarctica and the Transantarctic Mountains and ending in the Ross Embayment. East Antarctica and the GSM have a seismic structure consistent with a continental craton. There is a sharp vertical velocity gradient across the region of the TAMSs, consistent with other studies [*Lawrence et al.*, 2006b; c; *Watson et al.*, 2006]. The red line in map view (lower) denotes location of cross section. Upper panel is subglacial bedrock topography with sea level in red. Center panel seismic velocities with major structural/topographic features are labeled: Transantarctic Mountains (TAMS), Wilkes Subglacial Basin (WSB), and Gamburtsev Subglacial Mountains (GSM).

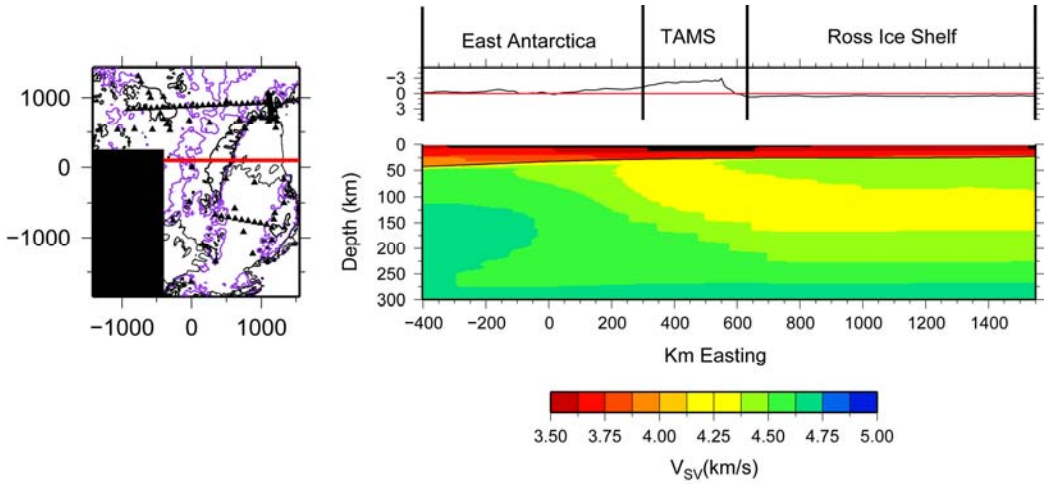

Figure 5.15: Vertical seismic cross section extending from East Antarctica, across the TAMS, to the Ross Ice Shelf. Fast Seismic velocities underlie East Antarctica to depths of ~250 km, consistent with a cratonic origin. The mantle beneath the TAMS is seismically slow, and the receiver functions in the region [*Chaput et al.*, 2011] do not support a thickened crust. Together, this suggests that the central region of the Transantarctic Mountains is supported thermally rather than isostatically. The red line in map view (left) denotes location of cross section. Upper panel is subglacial bedrock topography with sea level in red. Lower panel seismic velocities with major structural/topographic features labeled as Transantarctic Mountains (TAMS).

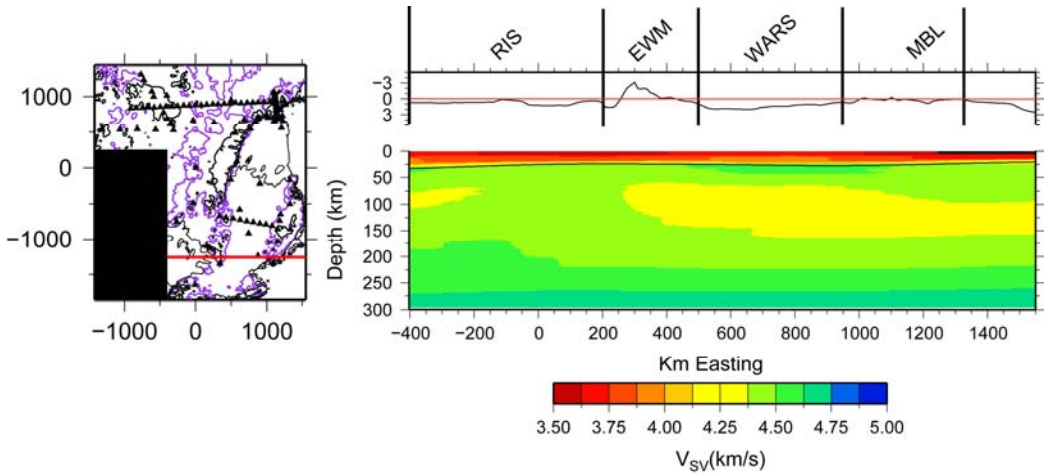

Figure 5.16: Vertical cross section of shear velocity from the Ronne Ice Shelf (RIS) to Marie Byrd Land (MBL). The imaged region extends across the Ellsworth Mountains (EWM), a region of detached East Antarctic crust. There is no significant shear velocity anomaly associated with the Ellsworth Mountains as might be expected if they were underlain by cratonic lithosphere. However, seismic velocities at depths of 50-150 are moderately faster than beneath the WARS. Faster seismic velocities at depths of ~ 50-100 km than beneath the WARS, suggesting an intact lithosphere, also underlie MBL. The red line in map view (left) denotes location of cross section. Upper panel is subglacial bedrock topography with sea level in red. Lower panel seismic velocities with major structural/topographic features labeled as Ronne Ice Shelf (RIS), Ellsworth Mountains (EWM), West Antarctic Rift System (WARS), and Marie Byrd Land (MBL).

Chapter 6

Conclusions

Broadband seismic arrays are enabling researchers to conduct ever more detailed and focused studies of tectonically interesting regions. While results from these studies give us the answers we so keenly seek, they often leave us asking new, deeper questions. In the chapters presented in this thesis, I have addressed some questions related to along-arc extension, earthquake source physics, and the seismic structure of the Antarctic continent at multiple scales. The Mariana Arc focuses along-arc extensional stress at volcanic cross-chains, allowing the system to stretch as the back arc basin 'unzips', Tonga is capable of producing large thrust-related earthquakes, and the seismic structure of Antarctica is much more complicated than suggested by global tomography studies. While none of these results is, perhaps, incredibly surprising, they do provide new insights into poorly understood processes and regions within our earth. These insights are only possible by applying observational seismology to specific tectonic questions using local broadband deployments.